DISSERTATION

Analysis of Cavity Formation in Polycrystalline Materials at Elevated Temperatures

carried out for the purpose of obtaining the degree of Doctor technicae (Dr. techn.)
submitted at the Faculty of Mechanical and Industrial Engineering, TU Wien

by
Dipl.-Ing. Harald Radlwimmer
00425171

under the supervision of
Univ.Prof. Dipl.-Ing. Dr.techn. Ernst Kozeschnik
Institute of Material Science and Technology

reviewed by
Prof. Dr.-Ing. Ulrich Prahl
Institute of Metal Forming, Technische Universität Bergakademie Freiberg
Bernhard-von-Cotta-Straße 4, 09599 Freiberg, Germany
and
Associate Prof. Dipl.-Ing. Dr.techn. Heinz Pettermann
Institute of Lightweight Design and Structural Biomechanics, TU Wien
Gumpendorfer Straße 7, 1060 Vienna, Austria

This work was supported by the Austrian Research Promotion Agency (FFG), the government of Upper Austria (LOÖ), and Styria (ST) *science and industry do high quality research work together* within the framework of the Competence Centers for Excellent Technologies Program (COMET) of the Austrian government K-Project for Non-destructive Testing and Tomography Plus (ZPT+).

The author gratefully acknowledges the funding support of K1-MET GmbH, metallurgical competence center. The research program of the K1-MET competence center is supported by COMET (Competence Center for Excellent Technologies), the Austrian program for competence centers. COMET is funded by the Federal Ministry for Transport, Innovation and Technology, the Federal Ministry for Digital and Economic Affairs and the provinces of Upper Austria, Tyrol, and Styria. Beside the public funding from COMET, this research project is partially financed by industrial partners.

I confirm that going to press of this thesis needs the confirmation of the examination committee.

Affidavit

I declare in lieu of an oath that I wrote this thesis and performed the associated research myself using only literature cited in this volume. If text passages from sources are used literally, they are marked as such.
I confirm that this work is original and has not been submitted elsewhere for any examination, nor is it currently under consideration for a thesis elsewhere.

Vienna, October 2024

Harald Radlwimmer

Abstract

Low-ductility intergranular fracture at elevated temperatures is often a result of excessive pore formation at the grain boundary. This thesis analyses a steel grade with hot tensile tests, material simulations, and a custom finite element user-material subroutine to gain a comprehensive insight into the underlying mechanisms at a microstructural level. Conducted hot tensile tests with steel samples of different nominal diameters indicate a size dependence within the temperature range 850 °C to 950 °C. In contrast, the transition from a *cooling rate* to a realistic *cooling time* regime does not cause increased susceptibility to brittle fracture, which can also be demonstrated with MatCalc precipitation kinetics simulations. The deformation characteristics, and the nucleation potential of austenite, were investigated with finite element analyses in a temperature range of 800 °C to 1200 °C and a strain rate range of $1 \times 10^{-6}\,\mathrm{s}^{-1}$ to $1 \times 10^{2}\,\mathrm{s}^{-1}$. For this purpose, the material model and the nucleation model were implemented in Ansys Mechanical via user-programmable features. The former was implemented using the Kreyca-Kozeschnik state parameter constitutive model for strain-rate dependent plastic deformation. The material model was developed with a single element and validated with MatCalc thermokinetic simulations. Computer simulations on the introduced simple microstructure model helped study the deformation characteristics in conjunction with different grain boundary friction coefficients. The results show that the stress exaggeration decreases toward high temperatures and strain rates. However, the grain boundary model needs to be improved for high strain rates. The implemented void nucleation model is based on Gleixner et al. and Svoboda-Sklenička. The utilized driving force comprises hydrostatic stress and a chemical stress component arising from excess vacancies. The Tang-Plumtree model was adapted with state-of-the-art information from Ungár et al. for the latter. The results show that void nucleation in austenite preferably occurs between 900 °C and 1100 °C within a strain rate range of $1 \times 10^{-2}\,\mathrm{s}^{-1}$ to $1 \times 10^{-1}\,\mathrm{s}^{-1}$.

Kurzfassung

Niedrigduktiles interkristallines Versagen bei erhöhten Temperaturen ist oft die Folge einer übermäßigen Porenbildung an der Korngrenze. Um einen umfassenden Einblick in die zugrunde liegenden Mechanismen auf mikrostruktureller Ebene zu erhalten untersuchten wir eine Stahlgüte mit Heißzugversuchen, Materialsimulationen sowie mittels einer benutzerdefinierten Subroutine für Finite-Elemente-Analysen. Durchgeführte Heißzugversuche mit Stahlproben unterschiedlichen Nenndurchmessers deuten auf eine Größenabhängigkeit innerhalb des Temperaturbereichs 850 °C bis 950 °C hin. Im Gegensatz dazu führt der Übergang von einer *Abkühlrate* zu einem realitätsgetreuen *Abkühlzeitregime* zu keiner erhöhten Sprödbruchanfälligkeit, was auch mit MatCalc Ausscheidungskinetiksimulationen nachgewiesen werden kann. Die Verformungseigenschaften sowie das Keimbildungspotenzial wurden anhand einer Finite-Elemente-Analyse mit Austenit in einem Temperaturbereich von 800 °C bis 1200 °C und einem Dehnratenbereich von $1 \times 10^{-6}\,\mathrm{s}^{-1}$ bis $1 \times 10^{2}\,\mathrm{s}^{-1}$ untersucht. Hierfür wurden das Materialmodell als auch das Nukleationsmodell über frei programmierbare Benutzersubroutinen in Ansys Mechanical implementiert. Ersteres wurde nach dem zustandsparametrischen konstitutiven Modell für die dehnungsratenabhängige Plastizität nach Kreyca-Kozeschnik implementiert. Die Entwicklung des Werkstoffmodells erfolgte an einem einzelnen Element und wurde mit thermokinetischen MatCalc-Simulationen validiert. Computersimulationen mit unserem einfachen Mikrostrukturmodell wurden verwendet, um die Verformungseigenschaften in Verbindung mit verschiedenen Korngrenzenreibungskoeffizienten zu untersuchen. Die Ergebnisse zeigen, dass die Spannungsüberhöhung in Richtung hoher Temperaturen und Dehnraten abnimmt und, dass das Korngrenzenmodell für hohe Dehnraten verbessert werden muss. Das Nukleationsmodell basiert auf Gleixner et al. und Svoboda-Sklenička. Die verwendete Triebkraft setzt sich aus der hydrostatischen Spannung und einer chemischen Spannungskomponente, welche von den Überschussleerstellen stammt, zusammen. Für letztere wurde das Tang-Plumtree Modell anhand der neuesten Informationen von Ungár et al. adaptiert. Die Ergebnisse zeigen, dass Nukleation in reinem Austenit vorzugsweise bei einer Temperatur von 900 °C bis 1100 °C innerhalb eines Dehnratenbereichs von $1 \times 10^{-2}\,\mathrm{s}^{-1}$ bis $1 \times 10^{-1}\,\mathrm{s}^{-1}$ stattfindet.

Acknowledgment

First and foremost, I would like to express my sincere gratitude to my supervisor, Ernst Kozeschnik, whose unwavering commitment, insightful feedback, and constant encouragement have been instrumental in shaping this research. I would also like to thank Guillermo Requena for his fruitful input in the early stages of the project. In addition, I would like to sincerely thank Jiří Svoboda and Mohammad Reza Ahmadi for generously sharing their knowledge on nucleation and Helmut Böhm for his advice on finite element analysis. My sincere thanks go to my project colleagues Pierre Wiehoff, Katrin Bugelnig, Simon Großeiber, and Pere Barriobero-Vila for their valuable contributions. I would also like to express my deep gratitude to Peter Reisinger, Sergiu Ilie, Jakob Six, and Andreas Schiefermüller from the voestalpine Stahl GmbH's R&D department for their excellent cooperation and invaluable feedback.

I am grateful to Werner Konstanzer and Josef Niederberger from HTBLuVA Mödling for their support in making a sensor mount. I thank Kurt Caloun, Christian Zaruba, and Edith Asiemo for their excellent help in the laboratory. I am very grateful to Tomasz Wojcik, who skillfully took the transmission electron microscopy images of my samples at USTEM, and to Christian Gusenbauer, the expert behind the X-ray computed tomography work at the University of Applied Sciences Upper Austria Campus Wels. I thank my friends Robert Weiser and Jakob Gager for their invaluable advice on finite element simulations. I would also like to thank my colleagues for their stimulating discussions and help, especially Martin Lückl, Yao Shan, Manuel Kleinbichler, Aurélie Jacob, Piotr Warczok, Johannes Kreyca, Georg Stechauner, Erwin Povoden-Karadeniz, 魏文文 (Wen Wen Wei), Siamak Rafiezadeh, Christoph Krüger, Thomas Weisz, Philipp Retzl, Bernhard Viernstein, and Daniela Wipp. I am very grateful to my colleagues from other working groups, especially Franziska Chalupa-Gantner, Olivier Guillaume, Denise Hirner, Thomas Radinger, Gregor Weisgrab, and Sara Žigon-Branc. It has been a pleasure to get to know you.

I have spent almost every lunch break at TeigWare over the last few years. Thanks to Birgit Hofer and Elmar Jelinek for serving more than delicious food and incredible hospitality, and to André Vogel and Stephan Reiter-Petrov for the great lunch discussions.

My utmost gratitude goes to my family, especially my parents, Christa and Wolfgang, my partner, Anke, and our daughter, Frida, for their unwavering support throughout this journey. I am deeply grateful for the love and strength you have given me along the way.

Solastranden

Contents

1 Introduction **1**

2 Objectives **3**

3 State of the art **5**
- 3.1 Hot Ductility 5
- 3.2 Plasticity 14
- 3.3 Cavity Nucleation 21

4 Experimental **35**
- 4.1 Mechanical Testing 35
- 4.2 Precipitation Analysis 37

5 Simulation **39**
- 5.1 Cooling Rate Sensitivity 39
- 5.2 Finite Element Model 39
- 5.3 Material Model 41
- 5.4 Program Specific Features 44

6 Results **51**
- 6.1 Experimental 51
- 6.2 Calculations 52
- 6.3 Computer Simulation 58

7 Discussion **69**
- 7.1 Experimental Results 69
- 7.2 Calculations 71
- 7.3 Computer Simulations 72

8 Summary and Conclusions **75**

References **77**

A Strain Rate in the Extreme Fiber **91**

B Additional results **93**

CHAPTER 1

Introduction

Cavity nucleation causes low ductility intergranular fracture in creeping solids at elevated to high temperatures. Correct cavity nucleation prediction is critical for the service life assessment of creep-resistant structures and for producing transverse cracking susceptible steel grades on curved continuous casting lines. New knowledge concerning cavity nucleation in polycrystalline materials will help understand the failure mechanisms in more detail and, in turn, will guide the development of further improved materials and production routines.

Research on intergranular cavity formation began in the early 1930s. It was motivated by the need to predict the lifetime of aircraft engines and to advance the technical development of power plants [1]. It soon became apparent that cavity nucleation could not occur homogeneously, so heterogeneous nucleation sites had to be identified. Typical cavity nucleation sites are slip bands, grain boundary ledges, triple junctions, and, if present, grain boundary particles. A wedge-type fracture is often observed starting from the triple junction. This type of crack is believed to arise due to a grain boundary sliding assisted cavity coalescence [1].

However, the big question remained: How do cavities form? Investigations and theories range from atomic bond breaking [1] to typical fracture mechanics [2] and thermodynamic approaches [3–8]. Most of the latter use the framework of classical nucleation theory (CNT) [9–15]. Recent modifications of this theory come from Svoboda et al. [6, 7].

In the past, less attention has been paid to models that focus on excess vacancies [16, 17]. This study considers them because the idea seems promising.

CHAPTER 2

Objectives

This study aims to analyze the cavity formation in polycrystalline materials at elevated temperatures. Specifically, this research aims to determine the *hot ductility* of a transverse cracking susceptible steel grade under different cooling strategies using experimental methods, to evaluate the precipitate evolution using transmission electron microscopy, and to compare the results with computer simulations. However, the main objective is to identify a suitable plasticity model and a vacancy model, integrate both into a finite element analysis and perform simulations on a representative microstructure model at elevated temperatures over several orders of magnitude of strain rate using austenite as the material.

CHAPTER 3

State of the art

3.1 Hot Ductility

During the continuous casting process of steel production, the strand must pass through the hot ductility region, a region of reduced fracture toughness. Typically, this region lies between 1200 °C and 600 °C, although the exact extent depends mainly on the alloy. Unfortunately, in curved continuous casters, this temperature range of reduced ductility typically interferes with the straightening process, the unbending of the strand. The cracks that can occur during the straightening are typically of the transverse type (fig. 3.1 numbers 9 and 10). Since some steel grades are more susceptible to cracking than others, controlling the production parameters within narrow limits is essential to obtain a crack-free end product.

Typically, laboratory hot tensile tests evaluate a steel grade's susceptibility to transverse cracking based on its ductility, with postmortem reduction of area (RA) being the standard quantification measure ($RA_\mathrm{f} = \left(A_0 - A_\mathrm{f}\right)/A_0$). Here, A_0 is the initial cross-section of the specimen, and A_f denotes the one after straining to fracture. At first glance, the hot ductility behavior splits into three regions: (1) high

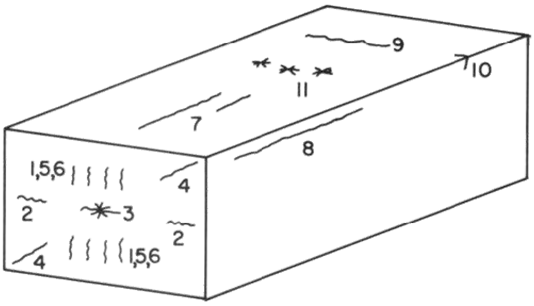

Figure 3.1. Schematic drawing of strand cast section showing different types of internal cracks. (1) Midway, (2) triple-point, (3) centerline, (4) diagonal, (5) straightening/bending, (6) pinch roll, surface cracks, (7) longitudinal, mid-face, (8) longitudinal, corner, (9) transverse, mid-face, (10) transverse, corner, (11) star. Reprinted from Brimacombe et al. [18].

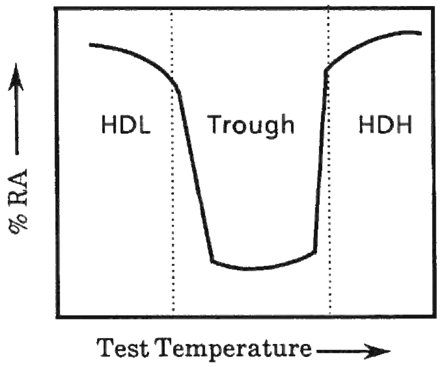

Figure 3.2. Schematic diagram of ductility curve defining the three characteristic regions of hot ductility. Reprinted from Mintz et al. [19].

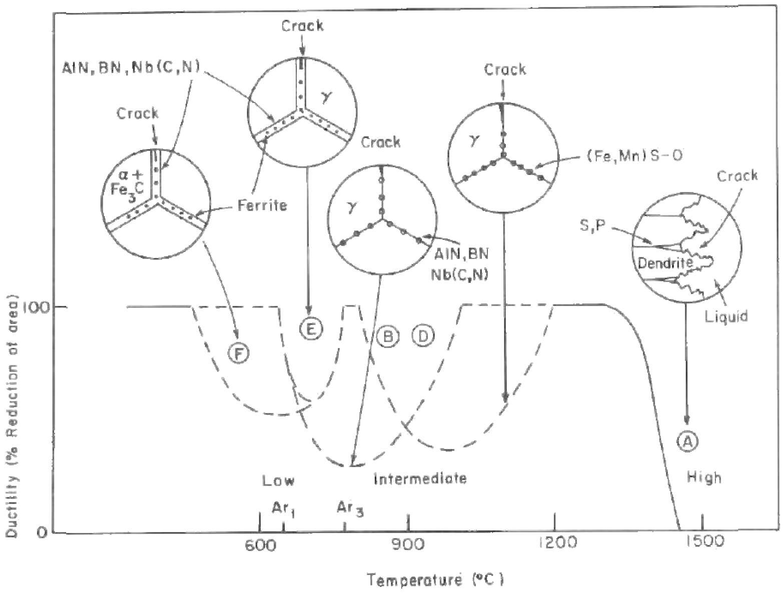
Crack
AlN, BN, Nb(C,N)
Crack
α + Fe₃C
Ferrite
γ
Crack
γ
AlN, BN
Nb(C,N)
Crack
γ
(Fe,Mn)S-O
Crack
S,P
Dendrite
Liquid
F
E
B
D
A
Low
Intermediate
High
Ar₁
Ar₃
Ductility (% Reduction of area)
100
0
600
900
1200
1500
Temperature (°C)

Figure 3.3. Schematic representation of temperature zones of reduced hot ductility of steel related to embrittling mechanisms. Reprinted from Thomas et al. [20]. For the meaning of letters A-F, see text.

ductility at low temperature (HDL), (2) ductility trough, and (3) high ductility at high temperature (HDH) (fig. 3.2) [19].

However, this only roughly describes the shape of the curve. In contrast, Thomas et al. [20] present a more fundamental approach and identify six embrittlement mechanisms of steels. In their representation, the ductility trough is a superposition of the following mechanisms: (A) microsegregation of sulfur and phosphorus residuals at solidifying dendrite interfaces, (B) sulfide embrittlement at high strain rates, (C) ductile intragranular fracture, (D) intergranular creep fracture, (E) embrittlement mechanisms in the two-phase austenite and ferrite region below the A_3 temperature, (F) embrittlement below the A_1 temperature for higher carbon steels (figs. 3.3 and 3.4). The temperature range of the mechanisms (C) to (E) typically overlaps with the straightening process.

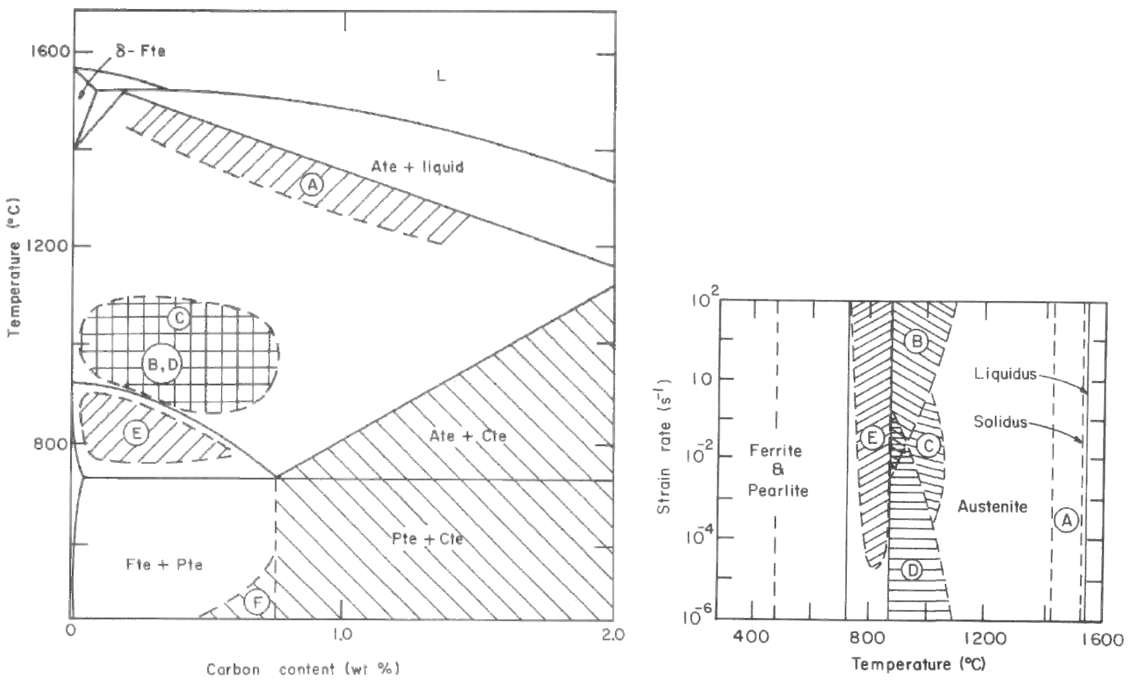

(a) **(b)**

Figure 3.4. Temperature zones of reduced hot ductility of steel, (a) Schematic diagram showing the zones of embrittlement at intermediate strain rates for the Fe-C system. (b) Possible fracture zones mapped for 0.2 percent C plain-carbon steel in strain rate temperature space. Reprinted from Thomas et al. [20]. For the meaning of letters A-F, see text.

Influencing Factors

Many factors affect hot ductility, but the most important ones fall into the following four categories [19, 21–24]:

- Composition and constituents
- Microstructural features
  - Grain size
  - Precipitates
- Process parameters
  - Oscillation marks
  - Multiple point bending
  - Casting speed; impact on
    - Strain rate
    - Metallurgical length
- Laboratory factors
  - Strain rate (correlation with casting speed)

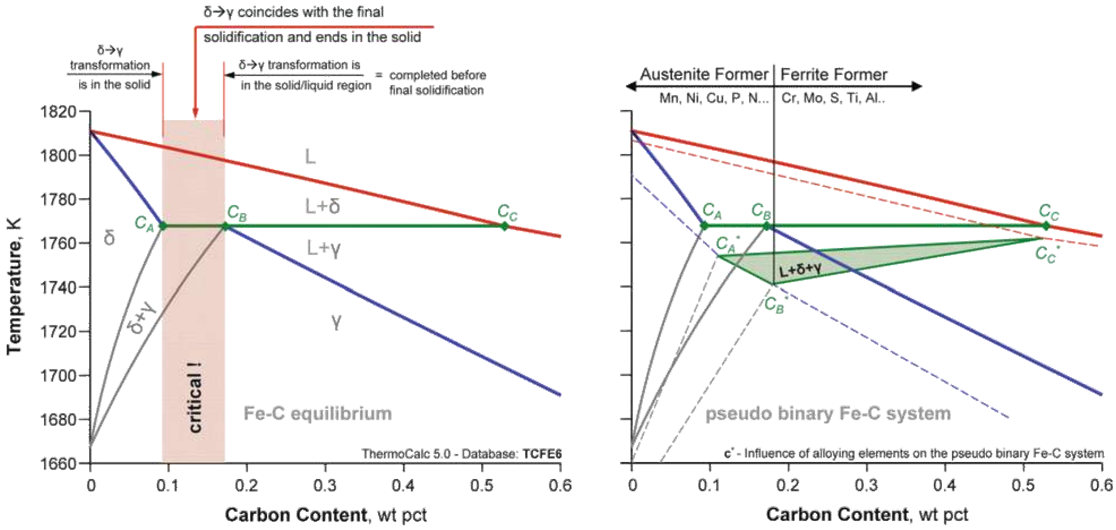

(a) (b)

Figure 3.5. Fe−C equilibrium diagram with the critical carbon range between 0.09 wt% C and 0.17 wt% C, and (b) influence of alloying elements on the Fe−C system. Reprinted from Presoly et al. [23]

.

- Temperature course of the testing routine
- Test device

Composition and Constituents

The chemical composition of a steel grade significantly influences its hot ductility properties. Due to the solidification sequence, continuous casting is challenging in the hypo-peritectic range, i.e., between 0.09 wt% C and 0.17 wt% C for plain carbon steel (fig. 3.5a). Precaution is necessary, as adding further elements to plain carbon steel shifts the peritectic range. The constituents contribute to forming either austenite or ferrite, as shown schematically in fig. 3.5b [23].

Besides shifting the peritectic region, the constituents also influence the shape of the hot ductility trough [19, 21, 25]. For a technically relevant amount of constituent, Mintz and Crowther [21], and Baker [26], summarize the influence of the alloying elements (table 3.1), while other authors focus primarily on precipitates [27, 28]. They find that, for example, niobium carbonitrides (Nb(C,N)) and aluminum nitrides (AlN) deteriorate hot ductility and fracture properties. However, it is only sometimes necessary to go that deep. Mintz et al. [19] divide the hot ductility behavior into three major steel composition classes: (1) Plain C−Mn and C−Mn−Al steels with low Al and N levels (0.02 %Al to 0.04 %Al, 0.005 %N), (2) C−Mn−Al steels with high Al and N levels, and (3) Microalloyed steels.

Microstructural Features

The two main reasons for the importance of microalloyed steels are their suitability for grain refinement and precipitation hardening in downstream processing. The goal of grain refinement is related to the Hall-Petch relationship [29, 30], which shows that

Die approbierte gedruckte Originalversion dieser Dissertation ist an der TU Wien Bibliothek verfügbar.
The approved original version of this doctoral thesis is available in print at TU Wien Bibliothek.
TU Bibliothek Your knowledge hub WIEN

Table 3.1. Alloying elements frequently used in microalloyed steels. Reprinted and adapted from [26]

Element	wt% in steel	Influence
C	<0.25	Strengthener
Mn	0.5 to 2.0	Delays austenite decomposition during accelerated cooling Decreases ductile to brittle transition temperature Strong sulphide former
Si	0.1 to 0.5	Deoxidizer in molten steel Solid solution strengthener
Al	<0.02	Deoxidizer Limits grain growth as AlN
Nb	0.02 to 0.06	Very strong ferrite strengthener as Nb(C,N) Delays $\gamma \rightarrow \alpha$ transformation
Ti	0 to 0.06	γ grain size control by TiN Strong ferrite strengthener
V	0 to 0.10	Strong ferrite strengthener by V(C,N)
Zr	0.002 to 0.05	γ grain size control [Zr(C,N)] Strong sulphide former
N	<0.012	Forms nitrides and carbonitrides with, e.g., Nb, Ti and V
Mo	0 to 0.3	Promotes bainite formation Ferrite strengthener
Ni	0 to 0.5	Increases fracture toughness
Cu	0 to 0.55	Improves corrosion resistance Ferrite strengthener
Cr	0.1 to 0.25	With Cu, increases atmospheric corrosion resistance
B	0.0005	Promotes bainite formation

the yield stress behaves inversely proportional to grain size ($\sigma_y \propto d^{-1/2}$) [31]. For this reason, grain size is often the focus of discussion. At least for pure face-centered cubic (fcc) materials, Kocks and Mecking [32] disagree with this standard approach. In their review of strain hardening, they point to the predominance of grain orientation (texture), which results from the direct influence of the Taylor factor on stress and strain. Thus, grain size is of secondary importance, and the hardening potential for polycrystals lies between the two texture orientation extremes (fig. 3.6).

In continuous casting, the loss of ductility is related to grain boundaries, grain junctions, and precipitates, such as MnS, AlN, and M(C,N)*. In addition, microcrack formation is temperature-dependent. Triple points and grain boundary precipitates are favorable nucleation sites at high temperatures. For the latter, even their size and spacing are essential. Grain boundary sliding favors microvoid growth and coalescence in the single austenite region. When deformation-induced ferrite first appears at lower temperatures, the voids nucleate at precipitates and inclusions within the thin ferrite film. Stress concentrations within the film strongly contribute to growth and coalescence [19, 27, 28, 33].

Precipitates affect the material strength; their number density, size, and distribution within the microstructure determine the degree of strengthening. An increased matrix strength degrades the fracture toughness because the concentration of stress at grain boundaries (GBs) promotes material failure along them, especially at low strain

---

*M may be substituted by any metal from the periodic table in microalloyed steels, commonly Nb, Ti, or V.

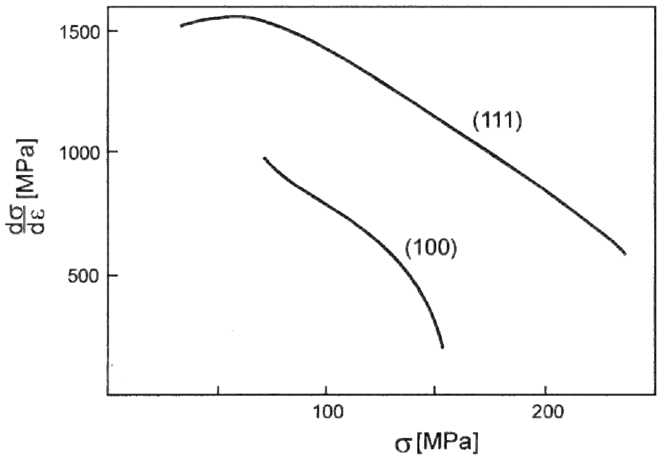

Figure 3.6. $d\sigma/d\varepsilon$–σ-plots for Ag single crystals with (100) and (111)-orientation deformed at room temperature. The two curves represent the expected range for textured polycrystals with different weightings of these two components. Reprinted from Kocks and Mecking [32].

rates where nucleation, growth, and coalescence of voids play a critical role [19–21]. However, precipitates can also have beneficial effects. Larger precipitates increase hot ductility, thereby reducing the susceptibility to transverse cracking [21, 33].

In strain-free austenite, Nb(C,N) precipitates almost exclusively at grain boundaries. Under strain, the preferred nucleation sites are the dislocation network, sub-grain boundaries, and vacancy clusters [19, 21, 34]. In addition to nucleation sites, the coherence and morphology of the precipitate have a significant influence (fig. 3.7). According to Dutta [35], Nb(C,N) precipitates in austenite have an incoherent or at least semicoherent character. After the austenite-ferrite transformation, they are all incoherent [36]. Therefore, the strength decreases significantly during the austenite-ferrite transformation. Nevertheless, precipitates are still valuable because they act as nucleation sites for ferrite, which ultimately improves the grain size in the final microstructure and strengthens the material according to the Hall-Petch relationship [37].

Process Parameters

Besides focusing on alloy constituents, Mintz and Crowther [21] summarize the influence of processing parameters and microstructure (see table 1 in ref. [21]). They show that increased casting speed is beneficial for hot ductility. In contrast, Petrus et al. [24] state that a reduced casting speed leads to a reduced metallurgical length and, as the ferrostatic pressure decreases, to less loaded support rolls. However, more than casting speed is needed to solve the issue, as it must always be within certain limits for a given casting machine. Another option is to control the cooling rate. Increased cooling rates affect hot ductility adversely, especially for Nb-bearing steels [21].

Laboratory Factors

Laboratory testing aims to create an environment as similar as possible to the one being mimicked. Since exact replication is difficult to achieve, test models should

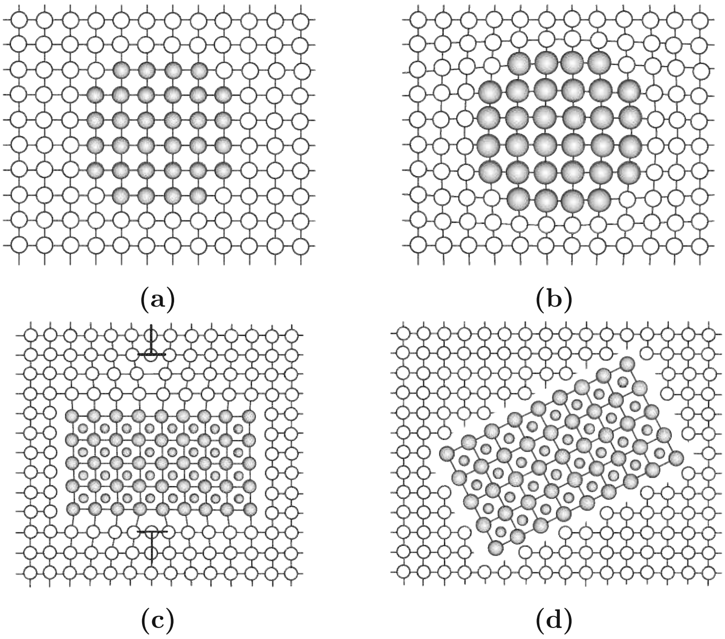

Figure 3.7. Schematic representation of a coherent precipitate (a) without and (b) with volumetric misfit, (c) precipitates with semicoherent, and (d) incoherent interface. Reprinted and adapted from Kozeschnik [38].

always mimic the desired process as closely as possible. The following section focuses on aspects of continuous casting.

In continuous casting, straightening occurs at temperatures around 1000 °C, just before the strand is flame cut into slabs. Sampling and testing of the material is not possible at this stage, so evaluation of hot ductility relies solely on as-cast specimens. Laboratory testing typically uses thermomechanical simulators for reheating, solution annealing, and laboratory testing. However, this has a significant disadvantage because the original microstructure gradually changes during reheating. Thus, a properly designed solution heat treatment should produce a microstructure with compatible properties. For steels, dwell times ranging from 60 s to 600 s at temperatures between 1200 °C and 1400 °C are common. Some authors even melt their samples locally to obtain more realistic results. Choosing the proper melt stabilizing tube is critical to avoid manipulating the steel composition, especially for titanium-bearing steels [21, 39, 40]. Some more sophisticated machines can partially melt the sample without needing a stabilizing tube, e.g., HZPM BETA 250-5 [41–43]. According to the literature, melting is unnecessary for niobium-bearing steels [21].

Three heating principles are available to achieve high temperatures: (1) induction, (2) radiation, and (3) direct resistance heating. Induction heating is widely used in dilatometers, certain hot tensile testers such as the HZPM BETA 250-5 [41–43], and, as of 2018, even some Gleeble machines [44]. Although induction heating is fascinating, most testing machines use radiation or direct resistance heating. Radiation heating provides a wide uniform temperature field with the disadvantage of slow heating rates (fig. 3.8a). In contrast, direct resistance heating provides high heating rates but only maintains the test temperature in a narrow region [22]. This issue generally arises due to cooled specimen grips and reduced specimen diameters

Die approbierte gedruckte Originalversion dieser Dissertation ist an der TU Wien Bibliothek verfügbar.
The approved original version of this doctoral thesis is available in print at TU Wien Bibliothek.
TU Bibliothek WIEN Your knowledge hub

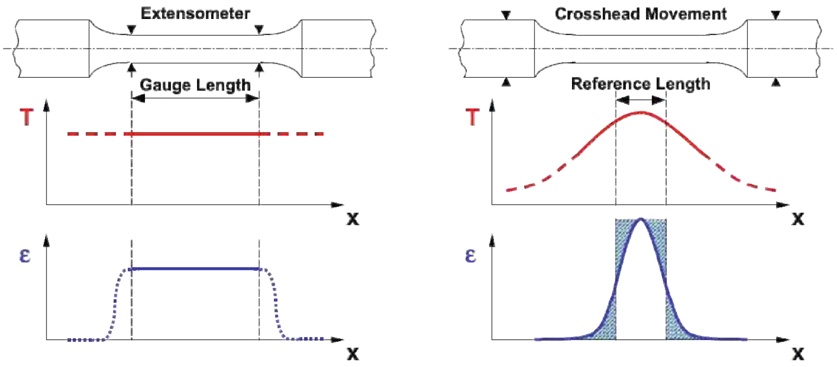

(a) (b)

Figure 3.8. Influence of (a) radiation and (b) direct resistance heating on temperature distribution and strain response. Reprinted and adapted from Glatzel [46].

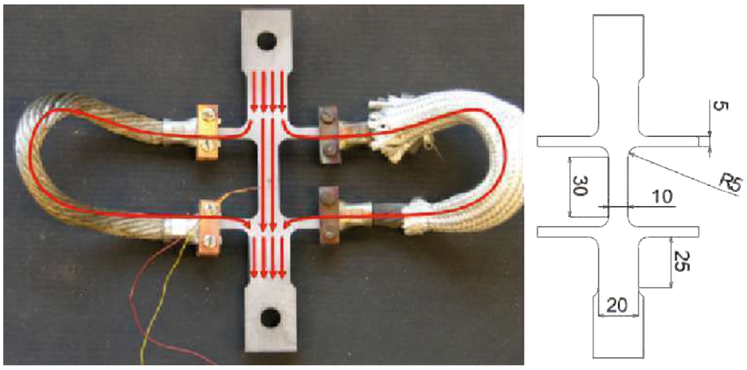

Figure 3.9. Tensile sample with equal current density. Reprinted from Abspoel et al. [47].

in the gage length, resulting in strain concentrations in a small region (fig. 3.8b). Therefore, this test method cannot meet standard test specifications [45]. Despite these drawbacks, direct resistance heating is widely used to characterize the hot ductility behavior of steel.

Abspoel et al. [47] extended the constant temperature zone for direct resistance heating with a complex sample geometry, including symmetrically arranged shunts (fig. 3.9). Since this approach relies on an evenly distributed current density, it only works up to the onset of necking. From that point on, a local temperature maximum is inevitable [47].

Suzuki et al. [39] and Zhang et al. [22] performed surface and core temperature measurements. The latter used their measurements to calibrate their FE model of Gleeble hot tensile tests. Their simulations provide evidence for the temperature gradient mentioned above. They also show that the strain rate is unevenly distributed throughout the specimen, as both temperature and stress are highest in the center of the specimen (fig. 3.10).

As previously discussed, chemical composition has a significant effect on hot ductility. Other influences are strain rate and test temperature [45], with the positive influence of increased strain rate on ductility mainly due to strain hardening [48, 49]. Steel grade, temperature, and strain rate impact the shape of the ductility trough (fig. 3.11).

Since the applied strain rate significantly affects hot ductility, selecting an appro-

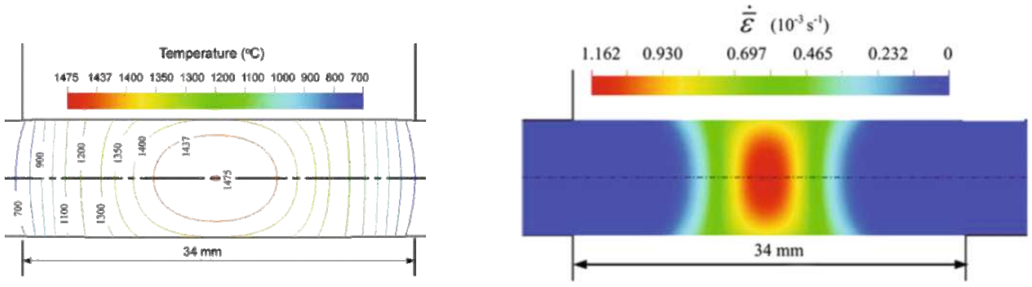

(a) (b)

Figure 3.10. Temperature and strain rate distribution for hot tensile tests with resistance heating. (a) Temperature distribution for a surface temperature of 1400 °C; (b) Calculated distribution of the equivalent strain rate $\dot{\bar{\varepsilon}}$ at nominal testing temperature 1200 °C and for a const. velocity $v = 0.001\,\mathrm{mm\,s^{-1}}$ of the moving grip. Reprinted from Zhang et al. [22].

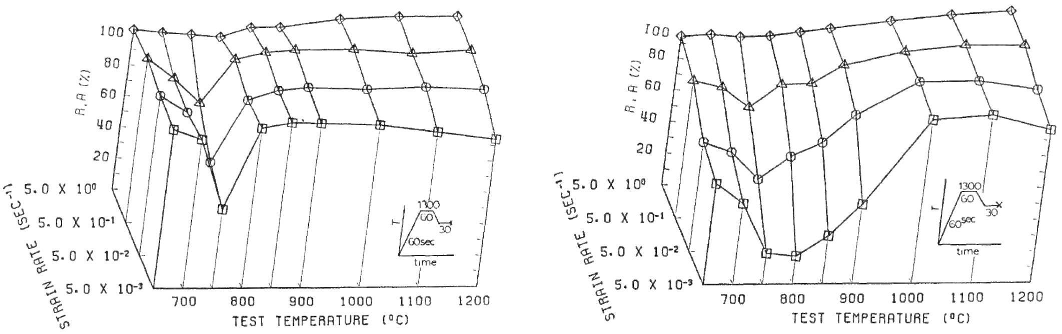

(a) (b)

Figure 3.11. Dependence of ductility on the strain rate and test temperature ranged from 1200 °C to 650 °C for (a) low carbon steel and (b) Nb-bearing steel. Reprinted from Suzuki et al. [39].

priate value is critical to obtaining realistic test results. Knowledge of the casting geometry is sufficient to calculate the strain rate during an ideal straightening process. Many authors use a strain rate between $1 \times 10^{-2}\,\mathrm{s^{-1}}$ and $1 \times 10^{-4}\,\mathrm{s^{-1}}$ [19, 50, 51]. Unfortunately, only a few authors justify their choice. Lankford is one of the few authors to provide an equation [52]. Similarly, the author of the present study calculated the strain and strain rate in the extreme fibers of the strand using the area conservation approach† (fig. 3.12 and eqs. (3.1) to (3.3)). Appendix A describes the calculation in more detail.

$$\varepsilon_\mathrm{i} = \ln\left(1/2\,(2R-h)\,/\,(R-h)\right) \tag{3.1}$$

$$\varepsilon_\mathrm{o} = \ln\left(1/2\,(2R-h)\,/R\right) \tag{3.2}$$

$$\dot{\varepsilon}_n = \varepsilon_n/\bar{t} = \varepsilon_n\bar{v}/\bar{l} \text{ with } n = \mathrm{o,i} \tag{3.3}$$

Here, R is the outermost radius of the strand, and h is the strand height. The following parameters refer to the neutral fiber, where $\bar{t}$ is the time to pass through the straightening zone, $\bar{v}$ is the casting speed, and $\bar{l}$ denotes the arc length of the

---

†It is assumed that the width of the strand is unchanged during the straightening process.

Die approbierte gedruckte Originalversion dieser Dissertation ist an der TU Wien Bibliothek verfügbar.
The approved original version of this doctoral thesis is available in print at TU Wien Bibliothek.
TU Bibliothek WIEN Your knowledge hub

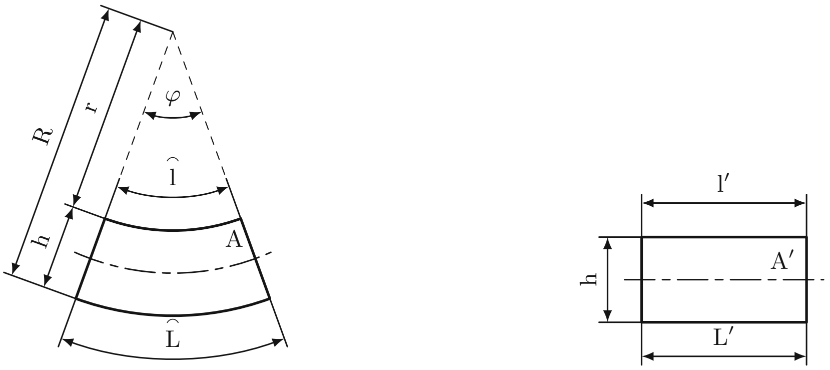

(a) **(b)**

Figure 3.12. Strand straightening in a curved strand caster. Strand segment before (a) and after (b) the straightening process

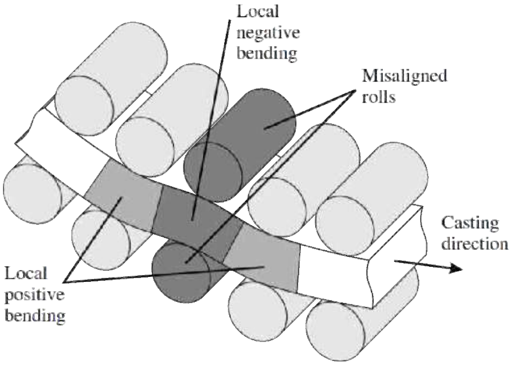

Figure 3.13. Successive local positive and negative bending due to misalignment. Reprinted from Pascon et al. [57].

straightening zone. Typical values‡ result in strains in the range of 6×10^{-3} to 3×10^{-2} and strain rates in the range of $3 \times 10^{-5}\,\mathrm{s}^{-1}$ to $3 \times 10^{-4}\,\mathrm{s}^{-1}$ at the innermost fiber. However, this is merely the strain rate for a perfectly shaped caster. Misalignments locally increase strain and strain rate (fig. 3.13). Therefore, accurate roll positioning and maintenance are paramount [52, 57].

3.2 Plasticity

Our understanding of plasticity rests on the existence of lattice dislocations, their generation, annihilation, and motion. The framework for this was developed independently by Orowan [58], Polanyi [59], and Taylor [60] in 1934. Argon [61] states that "dislocations are the most effective carrier of plasticity in crystalline solids."

Localized Frank-Read sources and double cross slip of screw dislocations generate additional dislocations [61, 62]. Annihilation occurs when two differently polarized types meet. The probability of the latter depends on the ability of the dislocation to move in the material. Obstacles, such as other dislocations, precipitates, solutes, or rain boundaries, typically impede free movement through the material [63, 64].

[‡] Radius $R = 9\,\mathrm{m}$ to $12\,\mathrm{m}$, height $h = 220\,\mathrm{mm}$ to $300\,\mathrm{mm}$ [53–55], $\bar{l} = 2.5\,\mathrm{m}$ to $4\,\mathrm{m}$ (assumption), $\bar{v} = 1.1\,\mathrm{m\,min^{-1}}$ to $1.6\,\mathrm{m\,min^{-1}}$ [56].

Although these obstacles are often insurmountable, especially at *low temperatures*, the annihilation of screw-type dislocations is still possible due to cross-slip [65–67]. At *high temperatures*, obstacles are easily overcome due to the sound availability of thermal activation energy; edge dislocations readily annihilate due to climb [68] or absorption from grain boundaries. The latter leads to grain boundary migration, sliding, and fracture [69]. The importance of diffusion depends on the strain rate. While it is essential for creep, it is only of marginal importance for forming processes [70]. In addition, climbing, shearing[§], and "Orowan" looping [71, 72][¶] assist in bypassing weak punctiform slip obstacles [61].

In simple terms, the plastic deformation behavior above 0.3 homologous temperature for metals and 0.4 for alloys and ceramics is strain-rate dependent. Typical high-temperature rate equation models are power-law creep (by glide alone or by glide-plus-climb), power-law breakdown, and Harper-Dorn creep. The two rate equations for diffusional flow are Coble creep (LT, grain boundary diffusion) and Nabarro-Herring creep (HT, lattice self-diffusion).

Rate Equations for High-Temperature Plasticity

The plasticity behavior of polycrystalline materials at high temperatures is strain-rate dependent, commonly called *creep*. As mentioned, creep can result from different dislocation-motion mechanisms (glide, climb, diffusive flow) and their combinations [63]. The following formulations allow a mathematical description of the different behaviors.

Power-Law Creep

The usual equation for the plastic shear strain rate in a power-law creep regime is

$$\dot{\gamma} \propto \left(\sigma_\mathrm{s}/G\right)^n , \tag{3.4}$$

where σ_s is the deviatoric part of the stress tensor, G is the shear modulus, and n is a power exponent in the range of 3 to 10 for high temperatures. Power-law creep above 0.6 homologous temperature can lead to dynamic recrystallization [63].

Glide alone is perhaps rate-controlling for creep below 0.5 homologous temperature for metals. Above this value, the material acquires another degree of freedom called *climb*. Climb-controlled creep (fig. 3.14) helps dislocations circumvent obstacles and reach a slip plane, where they can glide freely again, which also helps move ions and vacancies through the lattice at the atomic level [63]. According to Kassner [73], dislocation climb-controlled creep should be called diffusion-controlled creep.

The rate equation for power-law creep can represent both low-temperature and high-temperature creep and reads

$$\begin{aligned} \dot{\gamma}_\mathrm{PLC} &= \left(A_2 D_\mathrm{eff} G b / \left(k_\mathrm{B} T\right)\right) \left(\sigma_\mathrm{s}/G\right)^n , \text{ where} \\ A_2 &= 3^{(n+1)/2} A. \end{aligned} \tag{3.5}$$

[§] Coherent lattice configuration.

[¶] Semicoherent and incoherent lattice configurations.

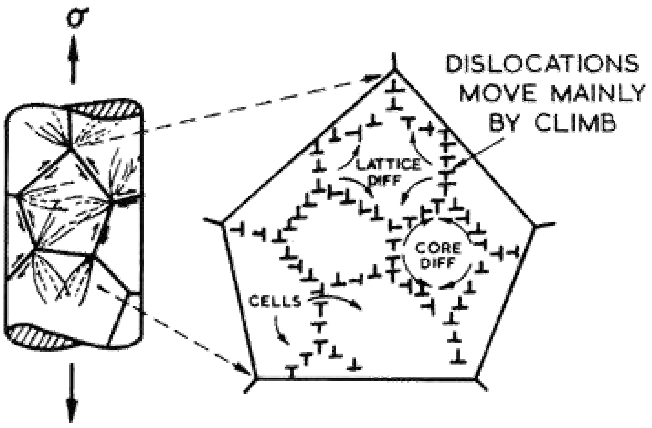

Figure 3.14. Power-law creep involving cell formation by climb. Power-law creep limited by glide processes alone is also possible. Reprinted from Frost and Ashby [63].

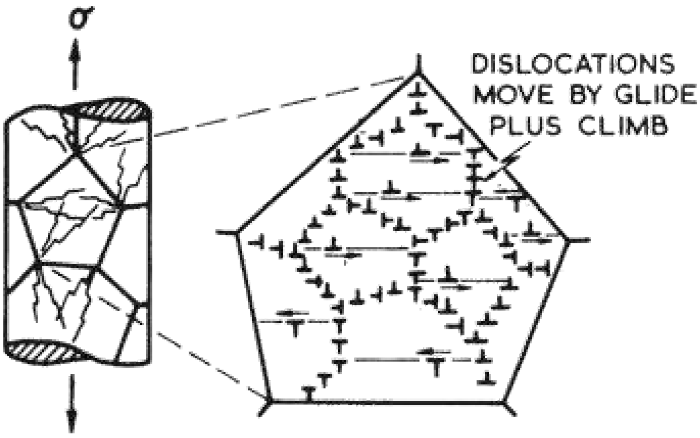

Figure 3.15. Power-law breakdown: glide contributes increasingly to the overall strain rate. Reprinted from Frost and Ashby [63].

Here, variable A_2 depends on the Dorn constant A[‖]. The other variables in the equation are the effective diffusion coefficient D_{eff}, the shear modulus G, the Burgers vector b, the Boltzmann constant k_{B}, the temperature T, the deviatoric part of the stress tensor σ_{s}, and the power-law constant n [63].

Power-Law Breakdown

The power-law breakdown represents the transition from climb to glide-controlled flow at high stresses (fig. 3.15). To date, the opinions in the community still differ on the governing mechanism. Some identify climb, facilitated by short-circuit diffusion, as the rate-controlling mechanism, while others prefer cross-slip and glide [74]. Since the rate equation for power-law creep (eq. (3.5)) cannot describe the transition, another equation (eq. (3.6)) is needed to account for climbing and gliding [63].

$$\dot{\gamma}_{\text{PLB}} = A\left(\sinh\left(\alpha' \sigma_{\text{s}}/\mu\right)\right)^{n'} \exp\left(-Q_{\text{cr}}/\left(k_{\text{B}}T\right)\right) \tag{3.6}$$

[‖] Frost and Ashby [63] list examples in chapter 4.

Die approbierte gedruckte Originalversion dieser Dissertation ist an der TU Wien Bibliothek verfügbar.
The approved original version of this doctoral thesis is available in print at TU Wien Bibliothek.
TU Bibliothek Your knowledge hub WIEN

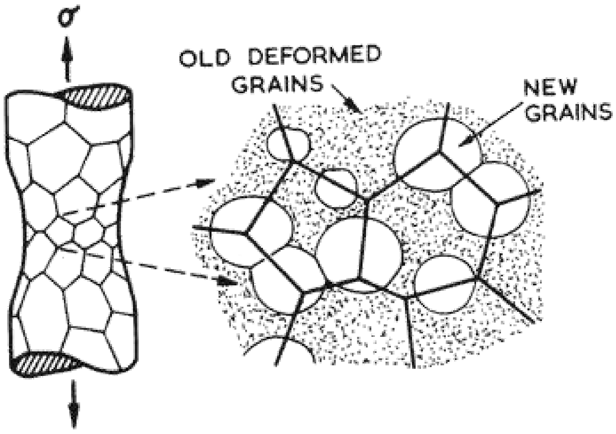

Figure 3.16. Dynamic recrystallization replaces deformed by undeformed material, permitting a new wave of primary creep, thus accelerating the creep rate. Reprinted from Frost and Ashby [63].

Combined rate equations for power-law creep and breakdown (eq. (3.7)) are available in the literature [63], but according to Frost and Ashby [63], they are hard to handle.

$$\dot{\gamma}_{\mathrm{PLC+B}} = \left(A_2' D_{\mathrm{eff}} G b / \left(k_{\mathrm{B}} T\right)\right) \left(\sinh\left(\alpha' \sigma_{\mathrm{s}} / G\right)\right)^{n'} \tag{3.7}$$

Harper-Dorn Creep

At sufficiently low stresses (below $5 \times 10^{-6} G$), materials creep proportional to the applied stress ($\dot{\gamma} \propto \sigma_{\mathrm{s}}$). The most likely climb-controlled Harper-Dorn creep does not alter the dislocation density with stress ($\varrho = \text{const.}$). Harper-Dorn creep is rate-controlling when a large grain size suppresses diffusion creep [63]. However, the current literature debates whether Harper-Dorn creep is a real phenomenon, transient or an artifact. The criticism focuses on the proposed constant dislocation density, which leads to an inappropriate physical solution of the basic steady-state equation (eq. (3.8)) at $\mathrm{d}\varrho/\mathrm{d}\gamma = 0$ [75].

$$\frac{d\varrho}{d\gamma} = \frac{d\varrho^{+}}{d\gamma} + \frac{d\varrho^{-}}{d\gamma} \tag{3.8}$$

Here, ϱ denominates the current dislocation density and γ is the shear stress. The superscripts decorating the dislocation density indicate their generation (+) and annihilation (−). Despite the ongoing discussions, the following—phenomenological—rate equation represents the Harper-Dorn creep [63, 73]:

$$\dot{\gamma}_{\mathrm{HD}} = \left(A_{\mathrm{HD}} D_{\nu} \mu b / \left(k_{\mathrm{B}} T\right)\right) \left(\sigma_{\mathrm{s}} / \mu\right). \tag{3.9}$$

Dynamic Recrystallization

Materials can recrystallize dynamically with a suitable dislocation substructure and homologous temperatures above 0.5 (fig. 3.16), The sensitivity of alloys to dynamic recrystallization (DRX) decreases with increasing alloy content [63, 76].

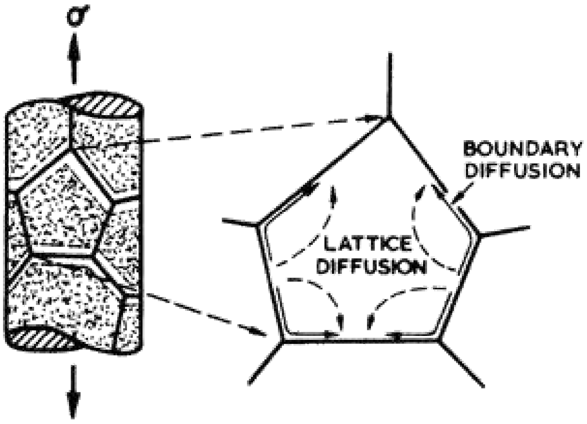

Figure 3.17. Diffusional flow by diffusional transport through and around the grains. The strain rate may be limited by the rate of diffusion or by that of an interface reaction. Reprinted from Frost and Ashby [63].

The availability of electron backscatter diffraction (EBSD) has dramatically improved the understanding of the mechanisms of DRX over the last few decades. Today, the literature distinguishes between (1) conventional/discontinuous, (2) continuous, (3) metadynamic, and (4) post-DRX. Discontinuous DRX is typical for metals and alloys with low to moderate stacking fault energy, such as austenitic steels, processed under hot working conditions ($T/T_\mathrm{m} > 0.5$) [76]. Dynamic recrystallization at high temperatures is likely the result of strain-induced boundary migration [76,77]. Due to the reduced temperature sensitivity of dynamic recrystallization compared to static recrystallization, some authors propose that DRX is an "athermal" process dedicated to vacancy generation during an ongoing deformation [77, 78].

There is evidence that shear bands significantly influence the recrystallization behavior in fcc materials. Due to the allotropic nature of iron, austenite, unless stabilized, does not exist at room temperature. Consequently, studies often focus on materials with a room-temperature stable fcc phase, i.e., nickel or copper [77].

Moreover, precipitates have a significant effect on dynamic recrystallization. The pinning effect of mature precipitates is low compared to newly nucleated ones. Therefore, preventing recrystallization requires continuous precipitation. In addition, elements that typically remain in solution, i.e., chromium, molybdenum, and nickel, influence the recrystallization behavior. For niobium-alloyed steels, the manganese-silicon (Mn/Si) ratio determines the dynamic recrystallization sensitivity [77].

Rate Equations for Diffusional Flow

Deviatoric stresses can induce diffusion creep by introducing chemical potential gradients at the grain boundary. The diffusion path is around the grain boundary at low temperatures (Coble creep) or through the lattice at high temperatures (Nabarro-Herring creep) (fig. 3.17). In alloys, solid solutions and dispersed second phases can influence the diffusion behavior [63, 79].

Coble Creep

Coble creep describes a creep regime below homologous temperatures below 0.7, controlled by vacancy diffusion along grain boundaries. Coble proposed the following steady-state rate equation

$$\dot{\varepsilon}_{\mathrm{ss}} = \left(A_{\mathrm{CC}} D_{\mathrm{gb}} \sigma_{\infty} b^{4}\right) / \left(k_{\mathrm{B}} T d^{3}\right), \tag{3.10}$$

where A_{CC} is a constant of unity order, D_{gb} is the diffusion coefficient along the grain boundary, σ_{∞} is the applied stress, k_{B} denotes the Boltzmann constant, T is the absolute temperature and d is the grain size [79].

Nabarro-Herring Creep

Nabarro-Herring creep describes a non-dislocation-based diffusion creep in fine-grained materials at very low stresses and temperatures close to the melting temperature (T_{m}). The Nabarro-Herring creep mechanism is the mass transport of excess vacancies from one grain boundary to another through the grain. Under uniaxial loading, excess vacancies develop on grain boundaries perpendicular to the loading direction. The steady-state rate equation reads

$$\dot{\varepsilon}_{\mathrm{ss}} = D_{\mathrm{sd}} \sigma_{\infty} b^{3} / \left(k_{\mathrm{B}} T d^{2}\right), \tag{3.11}$$

where D_{sd} is the self-diffusion coefficient, and all other variables are the same as in eq. (3.10) [79].

The Kreyca-Kozeschnik State Parameter Strengthening Model

The resistance of a crystal lattice to dislocation glide depends on its configuration. Metals with body-centered cubic (bcc) structures and strongly directionally bonded solids generally have high intrinsic plastic resistance. In contrast, those with face-centered cubic (fcc) and close-packed hexagonal (hcp) configurations tend to have low intrinsic plastic resistance. Extrinsic mechanisms can further increase the plastic resistance and depend on the alloy (solid-solution strengthening and precipitation strengthening) or dislocation configuration (strain hardening) [61].

In the past, it was common to describe the strengthening behavior of a material with a power law, the Hollomon equation $\sigma_{\mathrm{y}} = \sigma_0 + K\varepsilon^{n}$ [80, 81], where σ_0 is the initial yield stress, K is a constant, ε denotes the strain, and n is the strain hardening exponent. Because of their simplicity, these models were later used as an elegant way to keep the computational cost of finite element calculations down. Unfortunately, the Hollomon equation is purely empirical [82] and cannot provide the same fundamental insight into strengthening mechanisms as modern state parameter-based models, such as Kreyca and Kozeschnik, for calculating stress-strain curves. The yield stress in the Kreyca-Kozeschnik model [83] reads $\sigma_{\mathrm{y}} = \sigma_0 + \sigma_{\mathrm{p}}$, where σ_{y} is the yield stress, σ_0 is the initial yield stress, and σ_{p} is the plastic stress.

The Kreyca-Kozeschnik model is perfect for this study because it does not consider precipitates or solutes. Therefore, the only remaining obstacles for dislocations are the dislocations themselves.

Die approbierte gedruckte Originalversion dieser Dissertation ist an der TU Wien Bibliothek verfügbar.
The approved original version of this doctoral thesis is available in print at TU Wien Bibliothek.
TU Bibliothek WIEN Your knowledge hub

Initial Yield Stress

According to Kreyca and Kozeschnik [83], the initial yield stress consists of a low-temperature part and a high-temperature part, which add up as follows:

$$\sigma_0^{-1} = \left(\sigma_0^{\mathrm{lt}}\right)^{-1} + \left(\sigma_0^{\mathrm{ht}}\right)^{-1}. \tag{3.12}$$

The low-temperature part of the equation

$$\sigma_0^{\mathrm{lt}} = \hat{\sigma}\exp\left(-k_\mathrm{B}T/\Delta F_0^{\mathrm{lt}}\ln\left(\dot{\varepsilon}_0/\dot{\varepsilon}\right)\right) = \hat{\sigma}\left(\dot{\varepsilon}_0/\dot{\varepsilon}\right)\exp\left(-k_\mathrm{B}T/\Delta F_0^{\mathrm{lt}}\right), \tag{3.13}$$

where $\hat{\sigma}$ is the mechanical threshold stress (MTS), i.e., the yield stress at 0 K, k_B and T have their usual meaning, $\dot{\varepsilon}_0$ is the maximum achievable strain rate, ε denotes the strain rate, and ΔF_0^{lt} is the energy required for a dislocation to overcome an obstacle in the absence of thermal activation. The maximum achievable strain rate is calculated as $\dot{\varepsilon}_0 = \varrho_0 bc$, where ϱ_0 is the initial dislocation density, b is the Burgers vector, and c is the speed of sound.

The high-temperature part reads

$$\sigma_0^{\mathrm{ht}} = \left(\hat{\sigma}\left(\dot{\varepsilon}k_\mathrm{B}T\left(\alpha bGM\right)^2\right)/\left(2bc\Delta F_0^{\mathrm{ht}}\exp\left(-\Delta F_0^{\mathrm{ht}}/\left(k_\mathrm{B}T\right)\right)\right)\right)^{1/3}, \tag{3.14}$$

where α is the so-called strengthening factor, G is the shear modulus, M is the Taylor factor, and ΔF_0^{ht} is the Helmholtz energy, the energy required without thermal activation.

The flow stress in the MTS model consists of athermal, intrinsic, and hardening components [84–86]. Since only the basic yield stress is considered in this study, the MTS simplifies to $\hat{\sigma} = \hat{\sigma}_\mathrm{b}$.

Strain Hardening

To describe strain hardening, Taylor [60] developed a model that relates the flow stress of a material to its dislocation density ϱ. The equation relies on the maximum resolved shear stress at a dislocation site and the average distribution of dislocations [87]. This relation finally yields the well-known Taylor equation

$$\sigma_\mathrm{p} = \alpha MGb\varrho^{1/2}, \tag{3.15}$$

where α is a constant, M denotes the Taylor factor, G is the shear modulus, b is the Burgers vector, and ϱ denotes the dislocation density. Except for the constant α and the dislocation density ϱ, the parameters are well known. While α is typically a fitting parameter, ϱ needs a proper description. Hence, it is now essential to describe the dislocation density evolution adequately.

Dislocation Density Evolution Models

Over the years, three groups of dislocation density evolution models have been established: (1) average dislocation density models, (2) spatiotemporal dislocation distribution models, and (3) discrete dislocation dynamics models [64]. One of the most widely used models is the Kocks-Mecking model [32, 88], which follows the

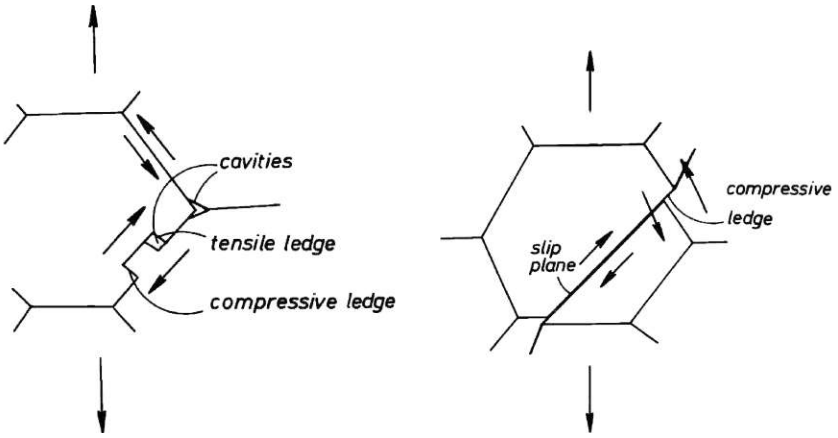

(a) (b)

Figure 3.18. Cavity nucleation at grown-in and slip-induced ledges and at a triple junction. Reprinted from Riedel [1].

first of the three mentioned approaches, the average dislocation density approach. Recently, Sherstnev et al. [89] have slightly adapted this model. Their formulation was then incorporated into the Kreyca-Kozeschnik model [83] and reads

$$\dot{\varrho} = \frac{\mathrm{d}\varrho}{\mathrm{d}t} = \frac{M\dot{\varepsilon}_\mathrm{p}}{Ab}\sqrt{\varrho} - 2B\frac{d^*_\mathrm{ann}M\dot{\varepsilon}_\mathrm{p}}{b}\varrho - 2C\frac{b^3 D_\varrho G}{k_\mathrm{B}T}\left(\varrho^2 - \varrho^2_\mathrm{eq}\right) \tag{3.16}$$

$$= \mathfrak{A}\sqrt{\varrho} - \mathfrak{B}\varrho - \mathfrak{C}\left(\varrho^2 - \varrho^2_\mathrm{eq}\right), \tag{3.17}$$

where M is the Taylor factor, ϱ denotes the current dislocation density, A, B, C are material parameters, b is the Burgers vector, $\dot{\varepsilon}_\mathrm{p}$ denotes the plastic strain rate, d^*_ann is the critical dislocation annihilation distance, D_ϱ denotes the substitutional self-diffusion coefficient along the dislocations, G is the shear modulus, k_B is the Boltzmann constant, T is the temperature, and ϱ_eq is the equilibrium dislocation density.

3.3 Cavity Nucleation

Cavities can nucleate within grains or at interfaces, such as grain boundaries. The latter are suitable nucleation sites due to their high diffusion transport capacity [8,90]. Nevertheless, cavitation is unlikely to occur at an arbitrary location since nucleation happens only readily at heterogeneous sites [1,38]. Typical nucleation sites, especially in industrial materials, are slip bands, grain boundary ledges, triple junctions (fig. 3.18), and grain boundary particles. Besides, stress fields from already nucleated cavities are known to foster further nucleation in their vicinity [91]. Based on the abundance of nucleation sites, cavity nucleation can also be considered material-dependent; alloys typically cavitate more willingly than pure metals [73, 92].

Cavity Nucleation Mechanisms

Cavity nucleation is triggered by dislocation pile-up, vacancy condensation, grain boundary sliding, or any combination of these mechanisms [73].

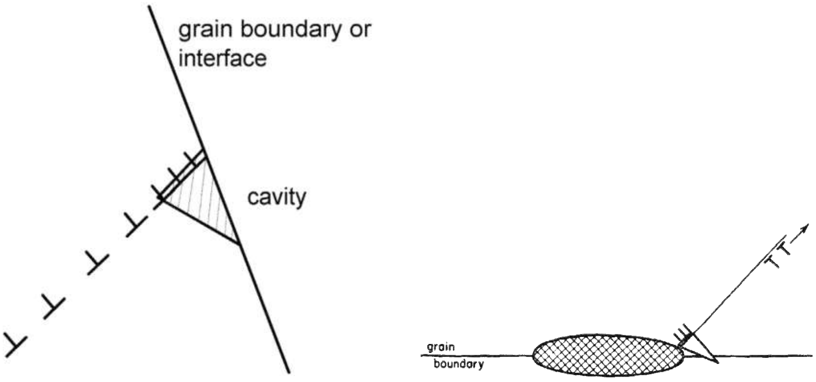

(a) **(b)**

Figure 3.19. Zener-Stroh-based cavity nucleation mechanisms. (a) Cavity nucleation from a Zener-Stroh mechanism. (b) Anti-Zener-Stroh crack, according to Kikuchi et al. [98]. The crack is formed when dislocations leave a region of high shear stress near the tip of a particle at the grain boundary, leaving behind dislocations of the opposite sign. Reprinted from, [73] and [99], respectively.

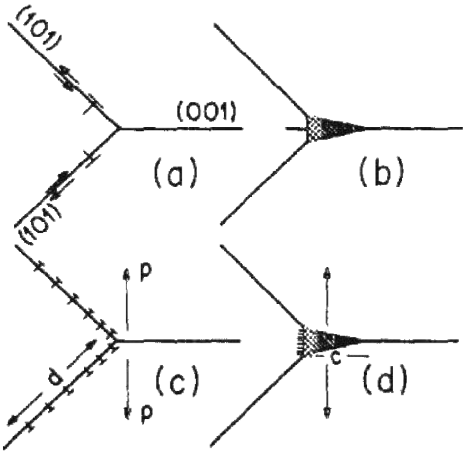

Figure 3.20. A crack formed by the coalescence of piled-up dislocations on intersecting slip planes (from Cottrell [100]). Reprinted from Weertman [99].

Dislocation Pile-Ups

Stress concentrations at obstacles, such as grain boundaries, arise from the pile-up of edge dislocations and can form a cavity, commonly called the Zener-Stroh mechanism (fig. 3.19a) [93–97]. Cavities can even form in stress fields near a particle interface under the prerequisite of induced slip. In this case, one part of the dislocation dipole leaves the highly stressed region, leaving behind its counterpart (Anti-Zener-Stroh mechanism, fig. 3.19b) [98, 99].

In addition to grain boundaries and inclusions, intersecting slip planes can block free dislocation motion. The latter behavior is the Cottrell mechanism (fig. 3.20). Thus, dislocations themselves are also obstacles [99, 100].

Vacancy Condensation

As early as the 1950s, Greenwood [3, 101] proposed vacancy condensation, but it was not widely accepted then and was only held responsible for the growth of preexisting voids [102]. Hull and Rimmer [103] suggested that it requires heterogeneous nucleation of cavities on particles, which later grow by vacancy condensation. Further studies on vacancy condensation [104, 105] suggested the stress concentration at nonshearable grain boundary inclusions and triple points as the missing link for void nucleation, leading to an extensive discussion of void nucleation by sliding displacements. Raj and Ashby [4] also advocated for vacancy condensation. A few years later, Riedel [2] argues that nucleation by vacancy condensation is unlikely, even under the assumption of stress concentrations. Crescent-shaped cavities are the only reliable way to reduce or eliminate the nucleation barrier [1].

Grain Boundary Sliding

Although Zener [93] already knew the importance of grain boundary sliding (GBS), the research community preferred diffusion mechanisms for some years [106]. Interestingly, GBS is perceived very differently. Often, it is presented as a single mechanism, but according to Langdon [107], there are two types of GBS: Rachinger GBS[**] and Lifshitz GBS[††]. It is important to note that GBS can hardly be significant since the least sliding grain boundaries, those perpendicular to the applied stress, will preferentially cavitate [1].

The Ball-Hutchinson model of superplastic deformation is a well-known model that links GBS to dislocation motion (fig. 3.21) [108]. Imagine two sets of grains; one set is properly aligned for free sliding along the boundaries, and the other is not, thus blocking movement. Consequently, local stresses arise precisely at the triple junction, where the two sets intersect. These stresses generate dislocations that leave the triple point toward the opposite grain boundary if high enough. There, the dislocations have three options: (1) climb to another lattice site (at HT), (2) be absorbed by the grain boundary, or (3) pile up at the edges of slip bands until the resulting back stress equilibrates the GBS. The latter encourages dislocations at the pile-up head to climb [65], and therefore, they must be continuously replaced to equilibrate further grain boundary sliding in the triple point [73, 108, 109].

Wadsworth et al. [111] later used the Ball-Hutchinson model, first, to postulate that dislocation glide ($\dot{\varepsilon}_{\mathrm{gbs}} \propto \sigma$) is climb-controlled ($\dot{\varepsilon}_{\mathrm{gbs}} \propto \sigma^2$) and, second, to explain that denuded zones cannot originate from Nabarro-Herring diffusion creep.

Cavity Nucleation Models

In the past, cavity formation has been treated in four ways, namely (1) observed nucleation kinetics, (2) atomic bond breaking, (3) vacancy condensation, and (4) stress concentrations during creep. As shown in this subsection, (1) and (3) provide nucleation rate equations, while (2) and (4) deal with the stress required to break an atomic bond.

[**] Conventional creep; accommodated by the movement of intragranular dislocations.

[††] Diffusion creep.

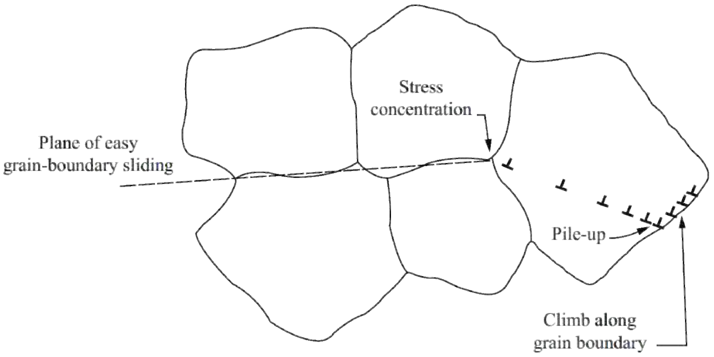

Figure 3.21. Ball-Hutchinson model of GBS accommodated by dislocation movement [108]. Reprinted from Kassner [110].

Observed Nucleation Kinetics

This basic approach relates the number of cavities N per unit grain boundary area to the product of an empirical factor α' (m^{-2}) and the creep strain ε (eq. (3.18)). The nucleation rate follows from the time derivative of the—detectable—postmortem cavity count (eq. (3.19)) [1].

$$N = \alpha' \varepsilon \tag{3.18}$$
$$J^* = \alpha' \dot{\varepsilon} \tag{3.19}$$

A small collection of this empirical factor α', including some steels and one nickel-based superalloy, is available in Riedel's book [1], but the suggested proportionality factor is not always valid to failure. A deviation from the suggested values results from a saturating cavity density or a stress-dependent proportionality factor. For nickel-based superalloys, the cavity density depends on the square of the strain [1].

Rupturing of Atomic Bonds

Breaking atomic bonds under typical creep conditions in the scope of an ideal crystal lattice (strength $E/10$) requires extreme stress concentrations. Accordingly, this cannot be the governing mechanism of cavity nucleation since cavities preferentially nucleate at interfaces. Therefore, the rupture of atomic bonds is more feasible at weaker bonded interfaces (strength $E/100$). In addition, impurity segregation can reduce the cohesive interface strength by up to 50 %. Even in the weakest configuration, grain boundary sliding is necessary to achieve the required stress concentrations [1].

Vacancy Condensation

The two theories discussed above are unsatisfactory because they are either a phenomenological description or simply unrealistic. Therefore, another approach was needed to explain pronounced cavitation under typical creep conditions.

Nucleation is the transformation of a metastable phase[‡‡] into a more stable one [112]. To simplify, nucleation is "crossing the phase boundaries" [113], which is

---

[‡‡] A phase that is not in thermal equilibrium.

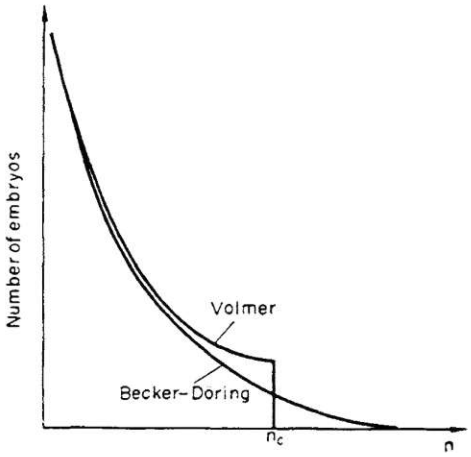

Figure 3.22. Distribution functions for embryos of different sizes according to Volmer and Becker-Döring theories of nucleation. Reprinted from Christian [115].

easier for heterogeneous nucleation than homogeneous nucleation because obstacles and imperfections help it. Nevertheless, nucleation is a stochastic process; it occurs only with a certain probability [38].

There are two nucleation theories: the classical nucleation theory (CNT) and the cluster dynamics modeling approach. Since both theories are derived from the master equation, they are based on the same fundamental research performed by Volmer and Weber [9], Farkas [10], Gibbs [11], Kaischew and Stranski [12], Becker and Döring [13], Frenkel [14], and Zeldovich [15] [1,38,112,114,115]. The coexistence of the two theories is likely due to their different strengths.

The advantages of the *classical nucleation theory* are the limited number of input parameters[§§] and the low computational requirements. However, only the nucleation stage can be calculated with CNT. Therefore, other models are needed to predict the growth and coarsening process [112]. In addition, some authors criticize CNT, as opposed to first principles, as a “semiempirical” approach because it employs macroscopic quantities such as the surface energy on an almost atomistic scale [1,116]. Furthermore, CNT can predict the onset of abundant nucleation but not absolute nucleation rates, as advanced models show [1]. The latter is a well-known consequence of the stochastic nature mentioned above [38].

The *cluster dynamics modeling approach* can represent all three stages but is computationally intensive and time-consuming. It also requires information that may require the use of atomistic modeling [112]. It is, therefore, not surprising that CNT is still widely used to describe nucleation.

The first convincing treatment of the classical nucleation theory came from Volmer and Weber [9]. Still, criticism soon arose because embryos automatically nucleate when they exceed their critical size. Later, Becker and Döring [13] corrected this in their improved theory (fig. 3.22) [115].

Nucleation is most likely to occur at grain boundaries and their particles. Typically, cavities are not perfectly spherical; instead, models assume a self-similar lenticular shape (fig. 3.23), which allows the use of dimensionless functions (eqs. (3.20) and (3.21)) [1,4].

[§§] Driving force, interface free energy, and condensation rate.

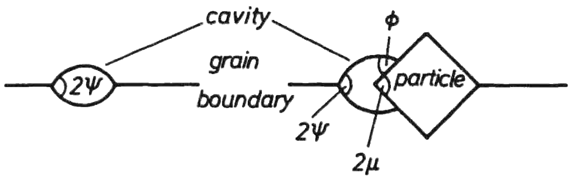

(a) (b)

Figure 3.23. Cavities (a) on grain boundaries and (b) at grain-boundary particles. Reprinted from Riedel [1].

$$\begin{aligned} f_{\mathrm{v}}(\psi) &= (2\pi/3)\left(2-3\cos\psi+\cos^3\psi\right) \\ \psi &= \gamma_{\mathrm{gb}}/\left(2\gamma_{\mathrm{s}}\right) \end{aligned} \tag{3.20}$$

$$\begin{aligned} f_{\mathrm{v}}(\psi') &= (4\pi/3)\left(2-3\cos\psi'+\cos^3\psi'\right) \\ \psi' &= \left(\psi+\phi-\mu\right)/2 \end{aligned} \tag{3.21}$$

For inclusion-free triple junctions, the self-similar cavity function is [4, 8, 117]

$$\begin{aligned} f_{\mathrm{v}}(\psi) = 2\,\Big(&\pi - 2\sin^{-1}\left(1/2\csc\psi\right) \\ &+ 1/3\cos^2\psi\left(4\sin^2\psi-1\right)^{1/2} \\ &- \cos^{-1}\left(\cot\psi/\sqrt{3}\right)\cos\psi\left(3-\cos^2\psi\right)\Big)\,. \end{aligned} \tag{3.22}$$

The nucleation process consumes free energy from abandoned surfaces but gains free energy from newly formed cavities

$$\Delta G = -\sigma\varrho^3 f_{\mathrm{v}}(\psi') + 3\gamma_{\mathrm{s}}\mathrm{s}\varrho^2 f_{\mathrm{v}}(\psi'), \tag{3.23}$$

where ΔG is the total free energy change, σ denotes the stress, ϱ is the radius, $f_{\mathrm{v}}(\psi')$ denotes a self-similar definition of a lenticular cavity, and γ_{s} is the interfacial energy. The partial differentiation $\partial\Delta G/\partial\varrho = 0$ of eq. (3.23)

$$\varrho^* = 2\gamma_{\mathrm{s}}/\sigma. \tag{3.24}$$

Substituting eq. (3.24) into eq. (3.23) gives the height of the critical nucleation barrier

$$\Delta G^* = 4\gamma_{\mathrm{s}}^3 f_{\mathrm{v}}(\psi')/\sigma^2. \tag{3.25}$$

A simple analysis of this equation shows that the height of the barrier (1) increases as the cube of the interfacial energy, (2) decreases as the square of the stress, and (3) vanishes for $f_{\mathrm{v}}(\psi') = 0$ [1].

Supersaturation of Vacancies Using a simple example, Riedel [1] shows that supersaturation of vacancies can provide a sufficiently high driving force for cavity nucleation. However, such high supersaturation requires the presence of irradiation or the Kirkendall effect; supersaturation due to the latter results from an unbalanced exchange of vacancies between two systems [118, 119]. Incidentally, it is impossible to superimpose the free energy changes of the stress and the supersaturation [1].

Raj-Ashby Nucleation Approach For several decades, the application of the classical nucleation theory was unpopular. It took the research of Raj and Ashby [4] to bring it back to prominence. Their study implements three key assumptions: (1) There are $(c_{\mathrm{max}} - c)$ subcritical nucleation sites per unit grain boundary available for further nucleation, and stable cavities form proportional to an Arrhenius factor[¶¶]. (2) Clusters absorb vacancies but never emit them. (3) Vacancies move only along the grain boundary [1].

The nucleation rate J^* is the product of the absorption rate β^* per unit time and the density of critical clusters N_0^* per unit area:

$$J^* = \beta^* N_0^* \tag{3.26}$$

$$\beta^* = \left(f_{\mathrm{p}} \varrho^* \delta_{\mathrm{gb}} \Omega^{-2/3}\right) \left(c_0 \exp\left(\sigma\Omega / \left(k_{\mathrm{B}} T\right)\right)\right) \left(4 D_{\mathrm{vac}} \Omega^{-2/3}\right) / 4 \tag{3.27}$$

$$N_0^* = \left(c_{\mathrm{max}} - c\right) \exp\left(-\Delta G^* / \left(k_{\mathrm{B}} T\right)\right) \tag{3.28}$$

Here, δ_{gb} is the grain boundary thickness, Ω denotes the atomic volume, and $D_{\mathrm{vac}} = \left(\delta_{\mathrm{gb}} D_{\mathrm{gb}} / c_0\right)$ is the jump frequency of a vacancy expressed by the vacancy diffusion coefficient in a grain boundary. The dimensionless function f_{p} represents the self-similar shape of the cavity concerning the length of its perimeter in the grain boundary:

$$f_{\mathrm{p}}(\psi') = 2\pi \sin \psi' \tag{3.29}$$

Substituting eqs. (3.27) to (3.29) into eq. (3.26) for $\sigma\Omega << k_{\mathrm{B}} T$ and respecting the above relationship for D_{vac} gives

$$J^* = \frac{2 f_{\mathrm{p}}(\psi') \gamma_{\mathrm{s}}}{\Omega^{4/3} \sigma} \left(1 + \frac{\sigma\Omega}{k_{\mathrm{B}} T}\right) \delta_{\mathrm{gb}} D_{\mathrm{gb}} \left(c_{\mathrm{max}} - c\right) \exp\left(-\frac{\Delta G^*}{k_{\mathrm{B}} T}\right). \tag{3.30}$$

Unfortunately, the exponential part of eq. (3.30) is so dominant that it makes the equation behave like a switch. Imagine the following behavior: Below the threshold stress, no cavity can form, and any stress greater than or equal to this value results in a sudden activation of all available nucleation sites [1].

The Becker-Döring Theory of Nucleation Raj and Ashby [4] formulate their equation independently of the Zeldovich factor [1], which considers that the nucleus is destabilized by thermal excitation compared to the inactive state [120]. Therefore, this study follows the interpretation of the Becker-Döring nucleation theory as outlined by Gleixner et al. [90][***] and only recently applied by Ahmadi et al. [8].

The nucleation rate J is the product of the vacancy sticking rate R_{stick}, the number of vacancies at the surface of a critical embryo n_{s}^*, and the number of critical embryos Z^* per unit volume.

$$J = R_{\mathrm{stick}} n_{\mathrm{s}}^* Z^* \tag{3.31}$$

The sticking rate of vacancies R_{stick} depends on the atomic vibration frequency ν and the activation energy for the jumping process in the lattice $(U_{\mathrm{D,l}})$ and along the boundary $(U_{\mathrm{D,b}})$.

$$\begin{aligned} R_{\mathrm{stick}} &= \nu \exp\left(-U_{\mathrm{D},i} / \left(k_{\mathrm{B}} T\right)\right) \\ &= \nu \exp\left(-Q_{\mathrm{D},i} / \left(R T\right)\right), \text{ with } i = \mathrm{l}, \mathrm{b} \end{aligned} \tag{3.32}$$

[¶¶] The exponential part of eq. (3.28).

[***] They reference Christian [115].

The number of vacancies at the surface of a critical nucleus is calculated according to its geometry:

$$n^*_\mathrm{s} = A^*_\mathrm{m} n_\nu \delta_\mathrm{s}, \text{ where} \tag{3.33}$$

$$n_\nu = 1/\Omega \exp\left(-U_\nu / \left(k_\mathrm{B}T\right)\right) \exp\left(\sigma\Omega / \left(k_\mathrm{B}T\right)\right). \tag{3.34}$$

In eq. (3.33), A^*_m is the surface area of a critical nucleus in the matrix, n_ν denotes the number of vacancies per unit volume, and δ_s is the thickness of the surface layer. In eq. (3.34), U_ν is the formation energy of a vacancy in the absence of hydrostatic stress, and all the other variables have their usual meaning.

The critical number of embryos Z^* per unit volume is calculated according to

$$Z^* = N/n^* \left(\Delta F^* / \left(3\pi k_\mathrm{B}T\right)\right)^{1/2} \exp\left(-\Delta F^* / \left(k_\mathrm{B}T\right)\right), \tag{3.35}$$

where N is the number of possible nucleation sites per unit volume[†††], n^* denotes the number of vacancies in a critical embryo, and ΔF^* is the critical Helmholtz free energy obtained from $\partial \Delta F / \partial r$.

Finally, the nucleation rate for a single vacancy path eq. (3.36) or a multiple vacancy path according to eq. (3.37) is

$$J_\mathrm{single} = \frac{\nu A^*_\mathrm{m}\delta_\mathrm{s}}{n^*\Omega^2}\left(\frac{\Delta F^*}{3\pi k_\mathrm{B}T}\right)^{1/2} \exp\left(-\frac{U_{\mathrm{D},i}+U_\nu}{k_\mathrm{B}T}\right) \exp\left(\frac{\sigma\Omega}{k_\mathrm{B}T}\right) \exp\left(-\frac{\Delta F^*}{k_\mathrm{B}T}\right) \tag{3.36}$$

$$\text{with } i = \mathrm{l}, \mathrm{b} \text{ or}$$

$$\begin{aligned} J_\mathrm{multi} = &\left(\delta_\mathrm{gb} l^*_\mathrm{gb} \exp\left(-\frac{U_\mathrm{D,b}}{k_\mathrm{B}T}\right) + A^*_\mathrm{m} \exp\left(-\frac{U_\mathrm{D,l}}{k_\mathrm{B}T}\right)\right) \frac{\nu\delta_\mathrm{s}}{n^*\Omega^2}\left(\frac{\Delta F^*}{3\pi k_\mathrm{B}T}\right)^{1/2} \\ &\exp\left(-\frac{U_\nu}{k_\mathrm{B}T}\right) \exp\left(\frac{\sigma\Omega}{k_\mathrm{B}T}\right) \exp\left(-\frac{\Delta F^*}{k_\mathrm{B}T}\right). \end{aligned} \tag{3.37}$$

In eq. (3.37), δ_gb is the grain boundary width intersecting the critical embryo, and l^*_gb is the corresponding length. All other variables have the same meaning as above. The critical number of vacancies (eq. (3.39)) is derived from the two equated formulas for the cavity volume (eq. (3.38)) and the equation for the critical radius (eq. (3.24)) and is

$$n^*\Omega = f_\mathrm{v}(\psi')r^{*3}, \text{ where} \tag{3.38}$$

$$n^* = f_\mathrm{v}(\psi')/\Omega \left(2\gamma_\mathrm{s}/\sigma\right)^3. \tag{3.39}$$

As mentioned above, grain boundary diffusion is dominant. Therefore, employing equation eq. (3.36) for grain boundary diffusion alone should give acceptable results. Moreover, [1] and Christian [115] point out that the nucleation rate is not sensitive to the pre-exponential factor.

It is important to note that observable nucleation requires a nucleation barrier height of less than $\Delta G^* \lesssim 76\,\mathrm{k_B}T$ [121].

[†††] Here, the atomic density.

Time-Dependent Nucleation Riedel [1] further shows how the Raj-Ashby model [4] changes by treating the nucleation problem based on the research of Zeldovich [15]. The Fokker-Plank equation (eq. (3.40)) is the central equation in this problem, governing the continuity condition of the cluster flux in size space:

$$\frac{\partial N(n)}{\partial t} = \frac{\partial}{\partial n}\left(\beta(n) N_0(n) \frac{\partial [N(n)/N_0(n)]}{\partial n}\right). \tag{3.40}$$

The above equation can be treated in two ways: independently and as a function of cluster size. While the former gives the steady-state nucleation rate, the latter results in a transient solution of the Fokker-Plank equation (eq. (3.40)), which can help estimate a lower and an upper bound of the incubation time [1]. The steady-state nucleation rate solution is[‡‡‡]

$$J^* = \frac{f_\mathrm{p}(\psi')\sigma\delta_\mathrm{gb} D_\mathrm{gb}\left(c_\mathrm{max} - c\right)}{2\Omega^{1/3}\left(3\pi k_\mathrm{B} T \gamma_\mathrm{s} f_\mathrm{v}(\gamma')\right)^{1/2}} \exp\left(-\frac{4\gamma_\mathrm{s}^3 f_\mathrm{v}(\psi')}{\sigma^2 k_\mathrm{B} T}\right). \tag{3.41}$$

Again, the exponential part is dominant, and the nucleation reaches its full potential shortly after the trigger value (eq. (3.41)). Although only the pre-exponential factor has been improved, the equation is still valuable because it provides a rough estimate of the critical stress for cavity nucleation. It is important to note that this stress cannot be achieved by stress concentration alone [1]. As an alternative to the steady-state solution, the transient solution can be used to estimate the upper (ub) and lower (lb) bounds of the incubation time:

$$t_\mathrm{i}^\mathrm{ub} = 11.5\left(f_\mathrm{v}^2/f_\mathrm{p}\right)\left(\gamma_\mathrm{s}/\sigma\right)^5 \Omega^{-2/3}\left(\delta_\mathrm{gb} D_\mathrm{gb}\right)^{-1} \exp\left(-\sigma\Omega/\left(k_\mathrm{B} T\right)\right) \text{ and} \tag{3.42}$$

$$t_\mathrm{i}^\mathrm{lb} = 3 k_\mathrm{B} T n^* / \left(\sigma\Omega\beta^*\right). \tag{3.43}$$

Unified Thermodynamic Cavity Nucleation

The diagnosis is consistently negative in the above treatments since cavity nucleation would require unrealistic stresses ($\sigma > \left(\gamma_\mathrm{s}^3 f_\mathrm{v}/\left(10 k_\mathrm{B} T\right)\right)^{1/2}$) [1]. This diagnosis did not convince Svoboda et al. [6,7] and Svoboda [122,123]. They find that the thermal nucleation theory is still incomplete and requires a proper, purely thermodynamic retreat. This approach finally leads to the unified treatment of nucleation and growth of cavities (eq. (3.44)). The derived formula is, as Svoboda et al. [6] mention, a close relative of the Fokker-Plank equation (eq. (3.40)) but has a more general meaning due to the use of $1/A(n) = \beta_\mathrm{c}^+(n)$, the effective frequency of the vacancy cluster atomic emissions, instead of $\beta^+(n)$, the vacancy cluster absorption rate. The use of $\beta_\mathrm{c}^+(n)$ has the advantage that local stresses are not significantly relaxed during the nucleation of a cavity. However, since $\beta_\mathrm{c}^+(n)$ is an order of magnitude smaller than $\beta^+(n)$, the nucleation rate is also lower by the same amount [6].

$$\dot{N}(n) = \frac{\partial}{\partial n}\left(\frac{N_0(n)}{A(n)} \frac{\partial\left(N(n)/N_0(n)\right)}{\partial n}\right) \tag{3.44}$$

In a later publication, Svoboda and Sklenička [7] focused on intergranular inclusions and how cavities nucleate on them. They point out that Raj and Ashby [4]

[‡‡‡] Neglecting $\sigma\Omega$ compared to $k_\mathrm{B} T$.

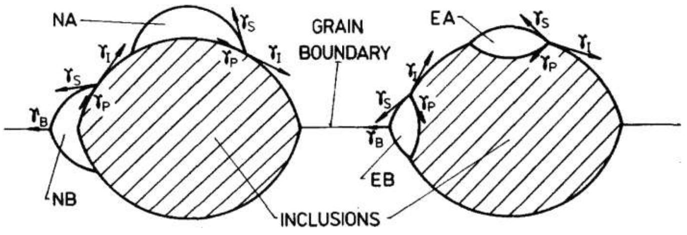

(a) (b)

Figure 3.24. (a) Cavities forming with inclusion a non-equilibrium system (NA and NB type cavities). (b) Cavities forming with inclusion the equilibrium system (EA and EB type cavities). Reprinted from Svoboda and Sklenička [7].

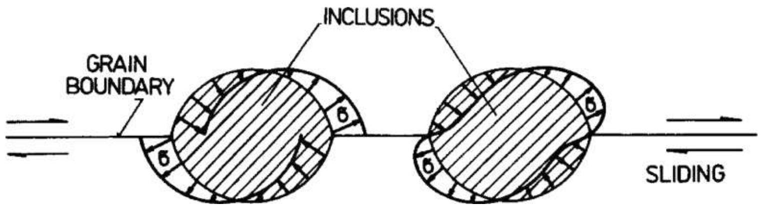

(a) (b)

Figure 3.25. Schematic illustration of the course of the local stress σ normal to the inclusion–matrix interface at the grain boundary sliding (a) without any diffusion acting in the inclusion–matrix interface (b) with the interface diffusion. Reprinted from Svoboda and Sklenička [7].

assumed infinite-sized inclusions, which is unrealistic since they are not on a size scale comparable to the radius ϱ of the free cavity nucleus surface. In addition, they note that void nucleation has previously been analyzed using a non-equilibrium system (fig. 3.24a); likewise, the converse must also be considered (fig. 3.24b). In the setup of Raj and Ashby [4], the dimensionless function of self-similar lenticular cavities $f_\mathrm{v}(\psi')$ (eq. (3.21)) is independent of the curvature radius ϱ. This treatment does not hold for $f_\mathrm{v} \neq f_\mathrm{v}(\varrho)$ [7], where the equation for the nucleation barrier G^* is

$$G^* = G(\varrho^*) = \sigma\left(3F_\mathrm{v}(\varrho^*) - 2f_\mathrm{v}(\varrho^*)\right)\varrho^{*3}/2 = \sigma h_\mathrm{v}(\varrho^*)\varrho^{*3}/2, \qquad (3.45)$$

where the term in parentheses is equal to $h_\mathrm{v}(\varrho^*)$. An analysis of the factors f_v, F_v, and h_v shows that the nucleation barrier for EB-type cavities (3.24b) is an order of magnitude smaller when the generalized shape factor h_v is considered.

Cavity nucleation is often discussed in the context of grain boundary sliding (GBS). In the presence of grain boundary inclusions in a sliding boundary and the absence of diffusion processes, the local stress distributes unsteadily along the grain boundary (fig. 3.25a). In a system with diffusion, the stress field changes continuously. Therefore, the latter can only induce cavity nucleation of type EA and NA (fig. 3.25b). Unfortunately, these two types have very high nucleation barriers. The EB-type is the most likely type of cavity to occur on an intergranular inclusion. Finally, it is essential to note that the generalized shape function is strongly dependent on the cavity radius and, therefore, the nucleation barrier increases rapidly with an increasing ratio of inclusion volume to critical inclusion radius v_I/ϱ^* [7].

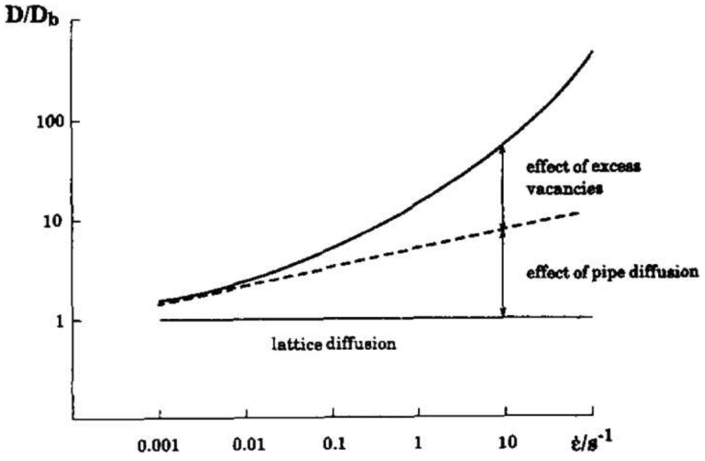

Figure 3.26. Strain-rate dependence of the enhancement factor for lattice self-diffusion in austenite at 1273 K. The dashed line indicates the contribution from pipe diffusion. Reprinted from Militzer et al. [17].

Excess Vacancies

According to Militzer et al. [17], excess vacancies are vital in cold working conditions. However, vacancies are rapidly annihilated at high temperatures and low strain rates (fig. 3.26).

In contrast, Tang and Plumtree [16] report that the aggregation of excess vacancies helps reduce the system's free energy. In turn, they are equally suitable nucleation sites. Additionally, precipitates are favorable nucleation sites. They suggest that the effect can be modeled as chemical stress σ_{chem} (eq. (3.47)). Together with the contribution of the excess vacancy concentration and the grain boundary vacancy concentration (eqs. (3.48) and (3.50)), the effective stress acting on the transverse grain boundary σ_{eff} is obtained.

$$\sigma_{\mathrm{eff}} = \sigma_\infty + \sigma_{\mathrm{chem}} \tag{3.46}$$

$$\sigma_{\mathrm{chem}} = k_{\mathrm{B}}T/\Omega \ln\left(1 + c_{\mathrm{ex}}/c_{\mathrm{gb}}\right) \tag{3.47}$$

$$c_{\mathrm{ex}} = 10^{-4}\dot{\varepsilon}_{\mathrm{loc}}L^2/\left(D_{\mathrm{v0}}\exp\left(-Q_{\mathrm{mig}}/\left(RT\right)\right)\right) \tag{3.48}$$

$$L = \left(2\varrho^{1/2}\right)^{-1} \tag{3.49}$$

$$c_{\mathrm{gb}} = c_0\exp\left(\sigma_\infty\Omega/\left(k_{\mathrm{B}}T\right)\right) \tag{3.50}$$

Here, 10^{-4} comes from the excess vacancy concentration during plastic deformation, $\dot{\varepsilon}_{\mathrm{loc}}$ is the local strain rate, L is the average diffusion distance, D_{v0} denotes the pre-exponential term for the volume diffusion coefficient, $Q_{\mathrm{mig}} = Q_{\mathrm{v}} - Q_{\mathrm{f}}$ is the activation energy for vacancy migration, and c_0 is the vacancy concentration in equilibrium with the grain boundary under an applied stress σ_∞.

The Tang-Plumtree model [16] predicts a large vacancy concentration at transverse grain boundaries around 0.5 homologous temperature. The concentration decreases at higher temperatures and has no significant contribution above 0.7 homologous temperature for a strain rate of $1 \times 10^{-4}\,\mathrm{s}^{-1}$. In addition, the effective stress is particularly strain-rate dependent between 0.3 and 0.7 homologous temperature (fig. 3.27).

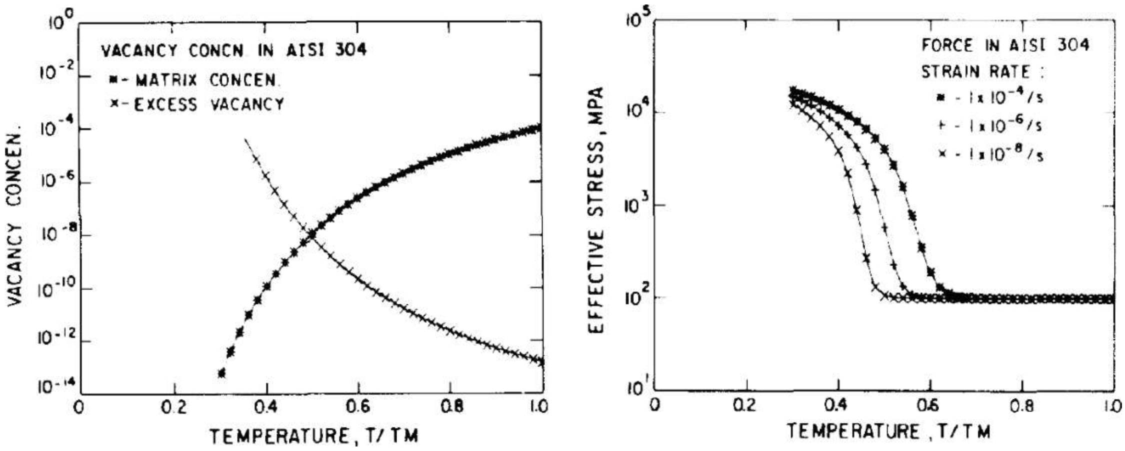

(a) **(b)**

Figure 3.27. (a) Vacancy concentration in the vicinity of grain boundaries as a function of temperature. Also depicted is the vacancy concentration in equilibrium with transverse grain boundaries under an applied stress of 100 MPa. (b) Total effective stress-inducing vacancy aggregation as a function of temperature. Reprinted from [16].

In the Tang-Plumtree model [16], the vacancy concentration during unidirectional deformation is, according to the references [124, 125], linearly depending on the plastic deformation

$$c_{\mathrm{pl}} = 10^{-4}\varepsilon. \tag{3.51}$$

However, in more recent research on copper, Ungár et al. [126] define the vacancy concentration as a function of the dislocation density ϱ, which additionally depends on the deformation mode, i.e., cold rolling (CR) (eq. (3.52)), and equal channel angular pressing (ECAP) (eq. (3.53)). Both equations saturate at a vacancy concentration of 5×10^{-4}. This saturation value is the lowest value that satisfies both experimental data sets.

$$c_{\mathrm{vac}}^{\mathrm{CR}} \cong 5 \times 10^{-4} \left(1 - \exp\left(-8 \times 10^{-8} \left(10^{-14}\varrho\right)^{5}\right)\right) \tag{3.52}$$

$$c_{\mathrm{vac}}^{\mathrm{ECAP}} \cong 5 \times 10^{-4} \left(1 - \exp\left(-2.2 \times 10^{-5} \left(10^{-14}\varrho\right)^{3.7}\right)\right) \tag{3.53}$$

The implementation of the equations of Ungár et al. in the Tang-Plumtree model requires the replacement of 10^{-4} by $c_{\mathrm{vac}}/\varepsilon$.

Other notable observations Ungár et al. [126] are that (1) vacancy accumulation happens more readily in the polycrystal and (2) vacancy concentration near the grain boundary can reach values up to 1×10^{-3}. Without deformation, the latter can only be reached at the melting point.

Shear-Crack Model

In 1984, Riedel [2] analyzed cavity nucleation based on atomic vacancy condensation [4, 5] and found that fast relaxation often suppresses nucleation. Consequently, Riedel [1, 2] treats the problem in terms of fracture mechanics[§§§] and concludes that the triple junctions support most of the applied shear stress. However, as Riedel [1] notes, this treatment does not contribute to a comprehensive understanding of nucleation. He also points out that stress concentrations at the particles are essential for high-temperature fracture in industrial materials, while the role of grain boundary sliding is marginal. In addition, he emphasizes a rough proportionality between strain rate and nucleated cavities, suggesting that slip within the grains plays a critical role in stress concentration.

[§§§] Unlike the CNT treatment, this approach provides nucleation stresses instead of nucleation rates. Therefore, it only helps to implement failure criteria, which is outside the scope of this study.

Die approbierte gedruckte Originalversion dieser Dissertation ist an der TU Wien Bibliothek verfügbar.
The approved original version of this doctoral thesis is available in print at TU Wien Bibliothek.
TU Bibliothek Your knowledge hub WIEN

CHAPTER 4

Experimental

4.1 Mechanical Testing

All material samples tested were continuously cast slabs of a typical microalloyed boiler steel grade (table 4.1) from voestalpine Stahl GmbH (Linz, Austria). The cross-section of each slab was 1600 × 250 mm^2. Besides, voestalpine Stahl GmbH also machined all specimens from near-surface regions of the slab, where cracking is most likely to occur. According to the specifications, the standard specimen had a gauge length of 15 mm and a nominal diameter of 8 mm (fig. 4.1). Some tests used an adapted double-diameter sample geometry.

Tensile tests provided a reference data set for flow behavior and hot ductility. All tests were performed on a DSI Gleeble 1500D machine in an argon atmosphere. The temperature was controlled by an S-type thermocouple (PtRd$_{10}$/Pt) spot welded in the center of the gauge length. Occasionally, the axial temperature distribution was measured with additional attached thermocouples. Once mounted, the test sequence began.

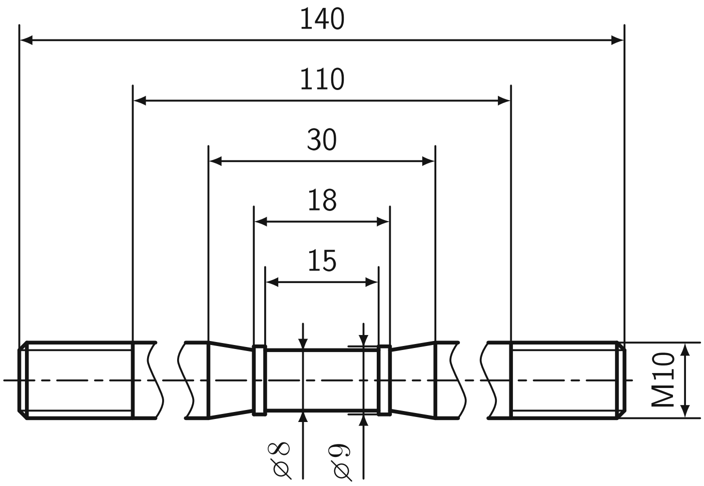

Figure 4.1. Dimensions of the standard tensile test sample.

Table 4.1. Chemical composition of the tested microalloyed boiler steel.

Element	wt%	
C	0.17	
Si	0.384	
Mn	1.17	
P	0.0078	
S	0.0007	
Al	0.033	
Cr	0.169	
Ni	0.28	
Mo	0.03	
Cu	0.172	
V	0.003	
Nb	0.018	
Ti	0.003	
Sn	0.003	
B	3	ppm
N	38	ppm
Fe	bal	
Al×N	1.254	$\times 10^{-4}$
Mn/S	1671	

First, the specimen was heated at $10\,\mathrm{K\,s^{-1}}$ to a solution-annealing temperature of 1320 °C, followed by a subsequent dwell time of 600 s to ensure a solid solution of all microalloying elements* and a microstructure compatible with continuous casting [19]. The subsequent sequence mimicked the cooling of the strand by continuously decreasing the temperature at a rate of $1\,\mathrm{K\,s^{-1}}$ down to the desired test temperature (fig. 4.2a). After an isothermal rest period of 15 s, the simulation of the straightening process began. The start of the straining also marked the first loading of the specimen.

The tests were performed at different strain rates for two reasons: First, the strain rate gradually changes from tension to compression over the height of the strand due to the straightening process. Second, the plant operator may vary the casting speed slightly to reduce failure, e.g., by transverse cracking. Therefore, the strain rate variation also revealed the casting speed sensitivity of the investigated steel grade.

All hot ductility tests in this study were conducted using tensile tests due to the known prevalence of transverse cracking in the upper half of the strand. These tests used different cooling regimes (fixed time window and constant cooling rate), specimen diameters (8 mm and 16 mm), strain rates ($1 \times 10^{-4}\,\mathrm{s^{-1}}$ to $3 \times 10^{-4}\,\mathrm{s^{-1}}$), and temperatures (800 °C to 1050 °C). Wiehoff [127] performed all mechanical tests at a strain rate of $1 \times 10^{-4}\,\mathrm{s^{-1}}$.

New approaches were needed since several other projects had already performed

---

*Confirmed by MatCalc computer simulations.

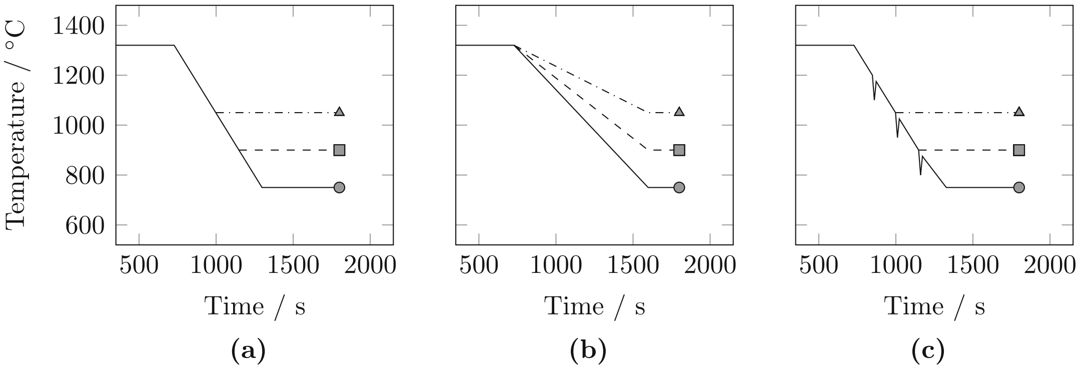

Figure 4.2. Schematic illustration of different cooling strategies. (a) Linear cooling with $1\,\mathrm{K\,s^{-1}}$, (b) linear cooling within 800 s, and (c) linear cooling with $1\,\mathrm{K\,s^{-1}}$ and three troughs á 100 K.

the above tests. Adapting the cooling stage of the standard test routine resulted in two new regimes. In the first regime, cooling occurred within a *fixed time* window (800 s), corresponding to the typical cooling time in a conventional slab caster between the mold and the start of the straightening process. This regime is more realistic because it allows for only small variations in casting speed. In addition, the applied cooling intensity is independent of the casting speed (fig. 4.2b). The second variant[†] considered the periodically recurring local cooling of the strand surface by contact with cooled support rolls. The superposition of temperature *troughs* and linear cooling resulted in the above characteristic.

Most of the experimental results and related discussions are available in the thesis of Wiehoff [127].

4.2 Precipitation Analysis

Wiehoff [127] identified Nb(C,N) as the predominant precipitate species in the investigated steel. This study gathers additional information on the species by studying its evolution with isothermal hot tensile tests. The employed routine was an adapted version of the above described and illustrated *linear cooling* test (fig. 4.2a) with a test temperature of 950 °C, isothermal holding times of 1 min, 5 min, 15 min, and 30 min, and a strain rate of $3 \times 10^{-4}\,\mathrm{s^{-1}}$. After straining to failure, carbon extraction replicas of polished sections were examined by transmission electron microscopy (TEM) in bright-field mode.

[†] Conducted by Wiehoff [127].

CHAPTER 5

Simulation

5.1 Cooling Rate Sensitivity

As shown in section 6.1 Precipitation Analysis, the experimental precipitation sequences confirmed the predictive quality of the MatCalc kinetic simulations. Consequently, it was permissible to investigate variations in cooling ($1 \times 10^{-2}\,\mathrm{K\,s^{-1}}$ to $1 \times 10^{2}\,\mathrm{K\,s^{-1}}$) and loading cycle (20 min) with computer simulations.

5.2 Finite Element Model

The shell region of a strand typically consists of columnar grains [128, 129]. In an idealized structure, equally sized and perfectly shaped hexagonal prisms adequately represent the microstructure, allowing a plane-strain model setup (fig. 5.1a). Besides, applying appropriate boundary conditions reduces the model to a representative area (fig. 5.1b). In Ansys Mechanical (Release 18.0), *constraint equations* are suitable for virtually extending representative areas to infinity. Vidal [130] demonstrates the application with a simple model (fig. 5.2). The application of the representative area model requires compatible boundaries, i.e., nodal displacements. Unfortunately,

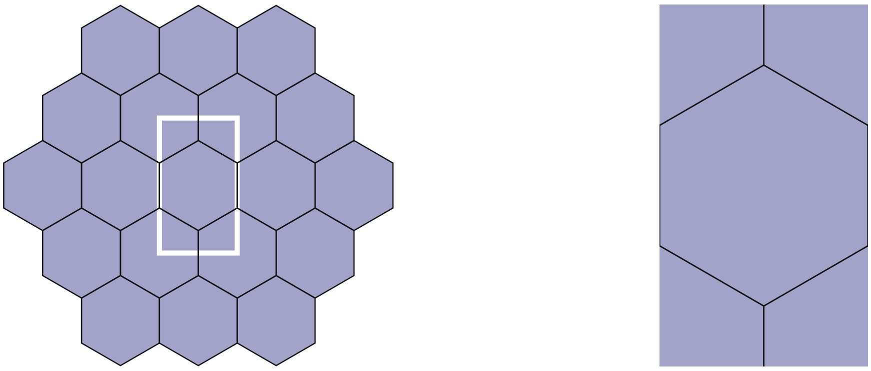
(a) (b)

Figure 5.1. Selection of representative area. (a) Infinite hexagon array representing the microstructure, (b) representative area.

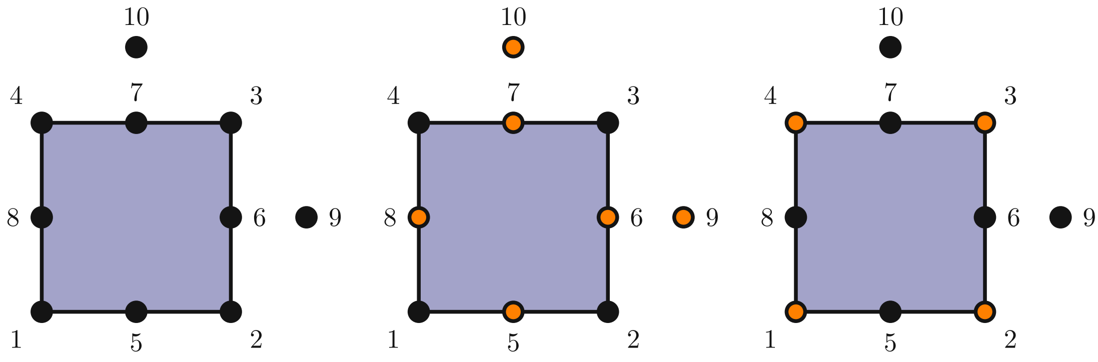

(a) (b) (c)

Figure 5.2. Simple representative area model illustrating the setup of the constraint equations. (a) Overview, (b) mid-side and dummy nodes, (c) corner nodes. Analog to Vidal [130].

a trivial equation setup leads to a rigid connection of the node pairs (eqs. (5.1) to (5.3)*).

$$u_{x2} - u_{x1} = 0 \tag{5.1}$$
$$u_{x6} - u_{x8} = 0 \tag{5.2}$$
$$u_{x3} - u_{x4} = 0 \tag{5.3}$$

The wise placement of dummy nodes (fig. 5.2, nodes 9 and 10) and their inclusion in the system of equations helps to solve this issue. The structure is no longer necessarily rigid, so the displacement of the nodes can reach nonzero values. Furthermore, this approach allows the application of strains or forces through the dummy nodes (eqs. (5.4) to (5.6)).

$$u_{x2} - u_{x1} = u_{x9} \tag{5.4}$$
$$u_{x6} - u_{x8} = u_{x9} \tag{5.5}$$
$$u_{x3} - u_{x4} = u_{x9} \tag{5.6}$$

Rewriting the above formulation leads to the equations for the nodes of the vertical side in the x-direction (eqs. (5.7) to (5.9)). The equations for the horizontal direction derive similarly (eqs. (5.10) to (5.12)).

$$u_{x2} - u_{x1} - u_{x9} = 0 \tag{5.7}$$
$$u_{x6} - u_{x8} - u_{x9} = 0 \tag{5.8}$$
$$u_{x3} - u_{x4} - u_{x9} = 0 \tag{5.9}$$

$$u_{x4} - u_{x1} - u_{x10} = 0 \tag{5.10}$$
$$u_{x7} - u_{x5} - u_{x10} = 0 \tag{5.11}$$
$$u_{x3} - u_{x2} - u_{x10} = 0 \tag{5.12}$$

---

*The equations represent only the x-direction of the vertical sides. The equations for the vertical sides in the y-direction and the horizontal sides in both directions derive similarly.

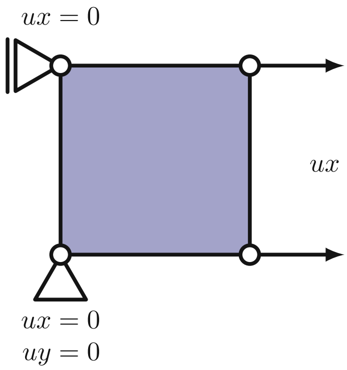

Figure 5.3. Setup of a single-element test.

A closer look at eqs. (5.7) to (5.12) shows that eliminating the displacements $u_{\mathrm{x}9}$ and $u_{\mathrm{x}10}$ further simplifies eqs. (5.7) and (5.10) and eqs. (5.9) and (5.12). The combination of both equation pairs then results in eq. (5.13). Therefore, there are only two kinds of equations: mid-side nodes (fig. 5.2b, eqs. (5.8) and (5.11)) and corner nodes (fig. 5.2c, eq. (5.13)).

$$u_{\mathrm{x}1} - u_{\mathrm{x}2} + u_{\mathrm{x}3} - u_{\mathrm{x}4} = 0 \tag{5.13}$$

Besides the constraint equations, a multi-body setup requires contact definitions. Ansys facilitates the setup process with its *Contact Wizard*, but adjustments still need to be made. Essential adaptations in this study's model are (1) the allowance of grain boundary sliding via the *no-separation (always)* constraint, (2) the rigid connection of internal grain boundaries, and the fact that (3) grain boundaries at the system boundary consider only normal forces. In addition, Coulomb friction can be part of the contact definition. The present study only uses static friction. There is no transition to a—lower—dynamic friction value.

5.3 Material Model

Developing a material model on a single-element model is standard practice. This approach ensures that the developer can monitor, control, and debug the behavior on the simplest system (fig. 5.3).

The material model of this study implements the Kreyca-Kozeschnik state parameter model (eqs. (3.12) to (3.14)), where the initial yield stress is temperature and strain-rate dependent. In addition, the strain-hardening contribution depends on the dislocation density and uses the Taylor equation (eq. (3.15)). The dislocation density evolution employs the same model as MatCalc [131], i.e., the extended Kocks-Mecking approach (eq. (3.16)). Consequently, MatCalc computer simulations are a perfect reference for developing the material model in this study.

In Ansys, users can implement their material laws via user-programmable features (UPFs). According to the documentation and lecture notes [132], there are three ways to utilize UPFs: the `/UPF` command, dynamic-link libraries (DLLs), and custom

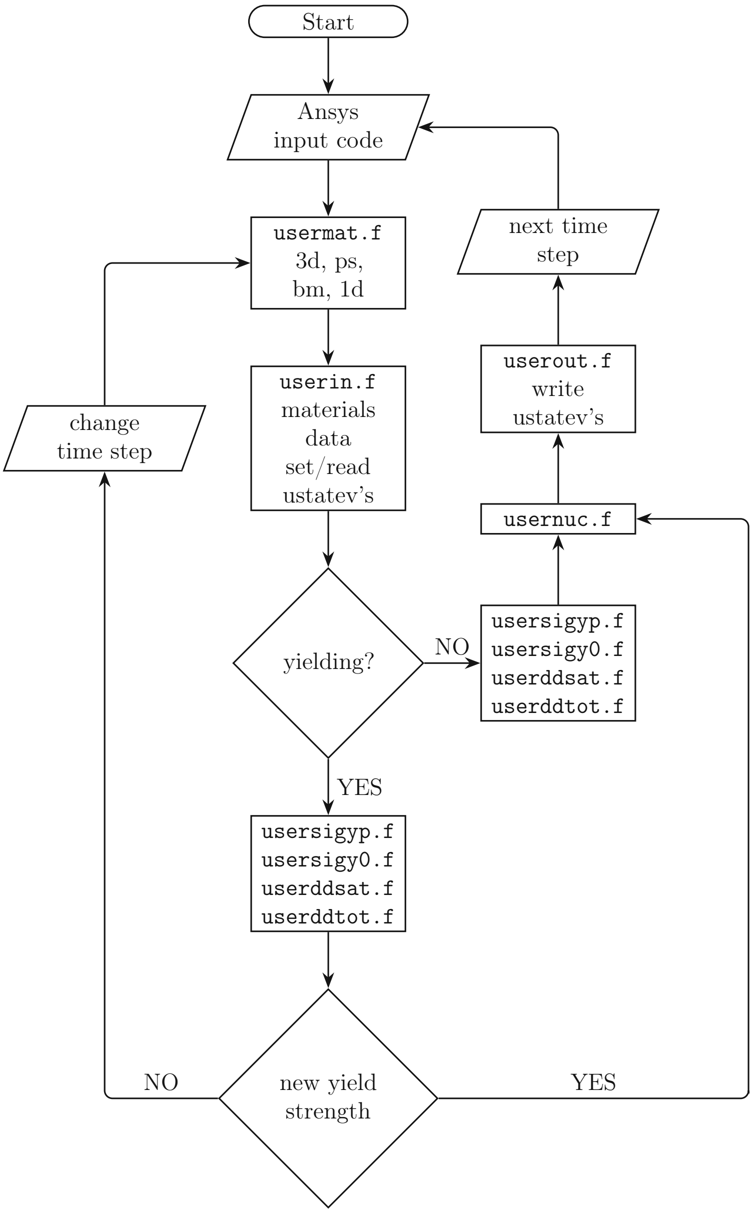
Start
Ansys input code
usermat.f 3d, ps, bm, 1d
userin.f materials data set/read ustatev's
yielding?
NO
YES
usersigyp.f usersigy0.f userddsat.f userddtot.f
usersigyp.f usersigy0.f userddsat.f userddtot.f
new yield strength
NO
YES
change time step
usernuc.f
userout.f write ustatev's
next time step

Figure 5.4. Ansys-UPF program sequence of this study.

Ansys executables, respectively. In the context of this study, the first method was suitable; hence, the Ansys UPF `usermat.f`[†] became the foundation of the material model implementation. For simplicity and modularity, the customized primary instance `usermat.f` calls several subroutines, such as `usersigyp.f`. Since these subroutines are an outsourced part of `usermat.f`, there is no need to compile any of them. Figure 5.4 outlines the program sequence and demonstrates where user state variables (USTATEVs) are read and written.

The dominant material laws in nonlinear finite element analysis typically use simple bilinear isotropic (BISO, fig. 5.5a) or multilinear isotropic (MISO, fig. 5.5b) stress-strain behavior. More advanced plasticity laws are either of a kinematic or an anisotropic kind. Due to the lack of experience with finite element material model

---

[†] The file extension *.f* refers to FORTRAN files.

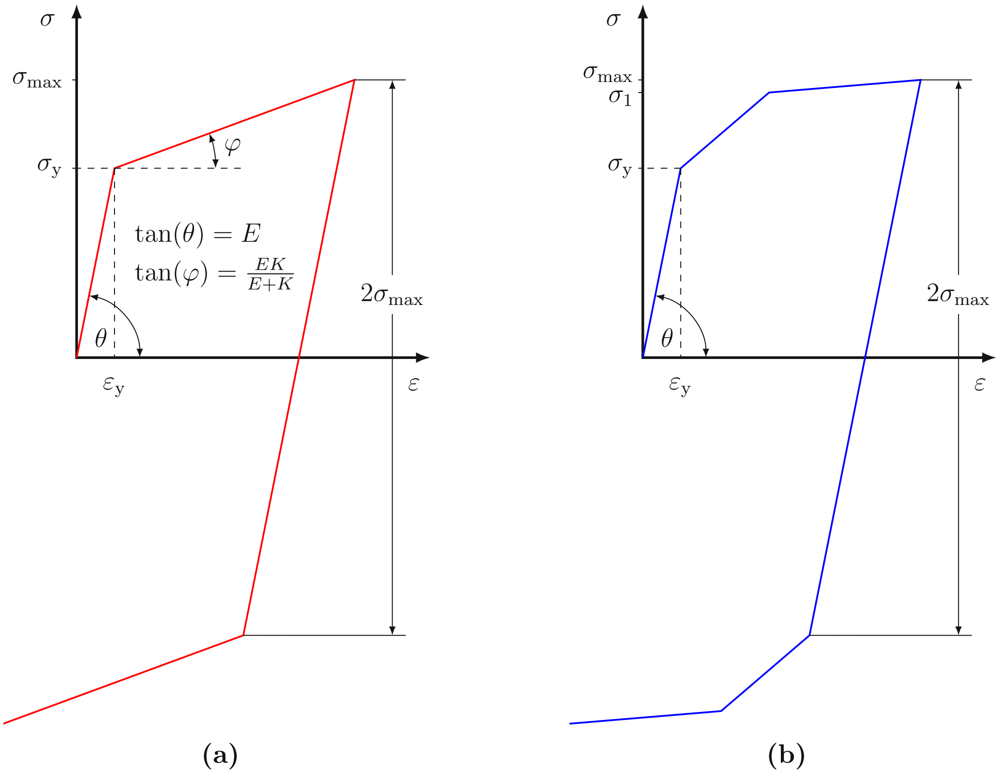

Figure 5.5. Stress-strain behavior of isotropic materials. (a) Bilinear isotropic hardening, (b) Multilinear isotropic hardening.

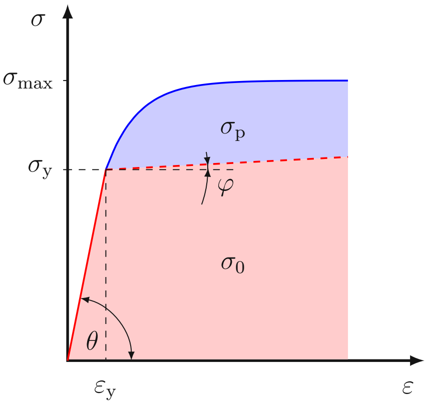

Figure 5.6. BISO framework based state parameter material model.

implementations, a simple isotropic material model is a good starting point. The existing BISO model (Ansys `usermat.f`) served as a template and facilitated the custom implementations. Ultimately, however, only the outline of the BISO material model remained untouched in this study. The Kreyca-Kozeschnik model replaces the elastic and strain-hardening models of the stress-strain curve's plastic part. The plastic slope φ of the original BISO model was set to zero to avoid any influence (fig. 5.6). As a result, the yield stress of the material model is fully temperature, strain rate, and time-dependent. The communication between the input code and the user subroutine happens only at the beginning and end of each time step.

Another important aspect of computer simulations is always the underlying data

Table 5.1. Materials parameters for austenite. The data stems from the indicated references.

Material	γ-iron	Ref.
Crystallographic and thermal data		
Lattice points per unit cell, Z	4	
Standard atomic weight, $A_\mathrm{r}(Fe)/(\mathrm{g\,mol^{-1}})$	55.845(2)	[133, 134]
Lattice constant, $a_0/(1 \times 10^{-9}\,\mathrm{m})$	$0.35519 + 8.1593 \times 10^{-6}\,T$	[135]
Burgers vector, $b/(\mathrm{m})$	$a_0/sqrt(2)$	[136]
Vacancy formation energy, $E_\mathrm{f}/(\mathrm{eV})$	1.7	[137]
Taylor factor, M	3.06	[63]
Melting temperature, $T_\mathrm{m}/(\mathrm{K})$	1810	[63]
Speed of sound, $v/(\mathrm{m\,s^{-1}})$	$\sqrt{(}[E\,(1-\nu)]/[\varrho\,(1+\nu)\,(1-2\nu)])$	[138]
Surface energy fcc-Fe, $\gamma_\mathrm{s}/(\mathrm{J\,m^{-2}})$	0.9	this work
	1.02	[7]
Grain boundary energy fcc-Fe, $\gamma_\mathrm{gb}/(\mathrm{J\,m^{-2}})$	0.8	this work
Generalized shape factor, h_v	1×10^{-2}	[7]
Dislocation evolution		
Dislocation density of well-annealed fcc-Fe, $\varrho/(\mathrm{m^{-2}})$	1×10^{11}	[38]
A	35	[139–141]
B	$7.5 - 0.7\,\ln\dot{\varepsilon}$	[139–141]
C	5×10^{-5}	[139–141]
Yield stress		
Basic yield strength, $\hat{\sigma}_\mathrm{b}/(\mathrm{MPa})$	20	[139–141]
Young's modulus, $E_0/(\mathrm{GPa})$	193	[38]
Temp. dependence of modulus, $\frac{E_0 - E(T)}{T - 273.15}$	73.33	[38]
Strengthening coefficient, α	0.5	[139–141]
Activation energy (HT), $\Delta F^\mathrm{ht}_{\sigma 0}/(\mathrm{kJ\,mol^{-1}})$	286.2	[139–141]
Lattice diffusion		
Pre-exponential, $\delta D_{0\mathrm{v}}/(\mathrm{m^2\,s^{-1}})$	1.8×10^{-5}	[63]
Activation energy, $\delta Q_{0\mathrm{v}}/(\mathrm{kJ\,mol})$	270	[63]
Boundary diffusion		
Pre-exponential, $\delta D_{0\mathrm{b}}/(\mathrm{m^3\,s^{-1}})$	7.5×10^{-14}	[63]
Activation energy, $\delta Q_{0\mathrm{b}}/(\mathrm{kJ\,mol})$	159	[63]
Core diffusion		
Pre-exponential, $\delta a_\mathrm{c} D_{0\mathrm{c}}/(\mathrm{m^4\,s^{-1}})$	1×10^{-23}	[63]
Activation energy, $\delta Q_{0\mathrm{c}}/(\mathrm{kJ\,mol})$	159	[63]
Pipe diffusion		
Pre-exponential, $D_{0\mathrm{d}}/(\mathrm{m^2\,s^{-1}})$	4.5×10^{-6}	[142]
Activation energy, $Q_{0\mathrm{d}}/(\mathrm{kJ\,mol})$	167	[142]

used. All the simulations presented here use the material data listed in table 5.1 in combination with the Ansys element type *PLANE182*, i.e., a two-dimensional four-node structural solid in a plane-strain configuration (section 5.2).

5.4 Program Specific Features

This section presents modifications and additional implementations in the user material model `usermat.f` and provides basic information on the subroutines. The text generally focuses on `usermat3d.f` but is analogously valid for `usermatps.f`, `usermat1d.f`, and `usermatbm.f`.

Time-discretized calculations require caching of variables to pass them from one time step to the next. Ansys transfers the data via user state variables (USTATEVs or SVARs), a bi-directional interface between the subroutine and the input code.

usermat.f

Although Ansys offers a wide range of material laws, it does not consider dislocations. Therefore, there is no strain-hardening model available. Fortunately, Ansys has a customizable subroutine for bilinear isotropic material (BISO) called `usermat.f`. The file sits in the installation folder[‡]. Initially, the template has a rate-independent plasticity behavior, but adjustments make it time-dependent (section 5.3). The customized model typically uses a tangent modulus equal to zero. Still, since the tangent modulus is not hard-coded to zero, both models can theoretically be mixed.

The customizations described below have two goals: (1) to keep template changes to an absolute minimum and (2) to outsource additional code into meaningful named subroutines wherever possible.

The first significant change to `usermat.f` is the inclusion of `locknm.inc` and its associated commands `pplock` and `ppunlock`, which ensure that the processors used in parallel processing never fall out of step. The subsequently implemented subroutine `userin.f` serves as a central interface for incoming user state variables from the Ansys computer simulation. Additionally, the input subroutine also contains initial material configurations.

Another critical step in the development process is identifying the code section that calculates the current yield stress σ_y. For the standard BISO model, the yield stress is

$$\sigma_\mathrm{y} = \sigma_0 + \left(\mathrm{d}\sigma_\mathrm{p}^\mathrm{BISO}/\mathrm{d}\varepsilon_\mathrm{p}\right)\bar{\varepsilon}_\mathrm{p}, \tag{5.14}$$

where σ_0 is the initial yield stress, $\mathrm{d}\sigma_\mathrm{p}^\mathrm{BISO}/\mathrm{d}\varepsilon_\mathrm{p}$ is the slope of the plastic flow curve from the BISO model, and $\bar{\varepsilon}_\mathrm{p}$ denotes the equivalent plastic strain at the end of the time increment. The modified equation differs only slightly from the above (eq. (5.14)), and the yield stress amounts to

$$\sigma_\mathrm{y} = \sigma_0 + \left(\mathrm{d}\sigma_\mathrm{p}^\mathrm{BISO}/\mathrm{d}\varepsilon_\mathrm{p}\right)\bar{\varepsilon}_\mathrm{p} + \sigma_\mathrm{p}^*, \tag{5.15}$$

where σ_0 is the initial yield stress according to the Kreyca-Kozeschnik model (eqs. (3.12) to (3.14)), and σ_p^* is the yield stress contribution of the Taylor equation at the beginning of the time increment (eq. (3.15)).

After computing the yield stress, the `usermat.f` subroutine determines whether an individual element yields or not. If the yielding occurs, the subroutine enters the appropriate branch of the code while safely storing the previously calculated value of the yield stress `sigy` (σ_y) in a temporary variable `sigy_t` (σ_y^*). The code then estimates the current equivalent plastic strain $\dot{\bar{\varepsilon}}_\mathrm{p}$ (eq. (5.16)) by dividing the incremental equivalent plastic strain `dpleq` by the time increment `dTime`. Conveniently, both variables are already available from the unmodified `usermat.f` subroutine.

$$\dot{\bar{\varepsilon}}_\mathrm{p} = \texttt{dpleq}/\texttt{dTime} = \Delta\bar{\varepsilon}_\mathrm{p}/\Delta t \tag{5.16}$$

Subsequently, the subroutine enters `usersigyp.f` to compute the yield stress contribution based on the dislocation density from the beginning of the current time increment. The returned value updates the yield stress. Moreover, it is also essential to execute the subroutine in case of elastic unloading. As the absence of plastic strain makes it difficult to achieve convergence, the subroutine ensures that the plastic strain rate never falls below $1 \times 10^{-8}\,\mathrm{s}^{-1}$.

[‡] `<path to Ansys>/Ansys Inc/v<three digit version number>/Ansys/customize/user`

userin.f

The `userin.f` subroutine is an interface for incoming material data from the Ansys input file and a library of elementary material parameters. It handles exceptions and provides some values in the first calculation step, e.g., the initial yield stress.

usersigy0.f

This subroutine calculates the initial yield stress contribution, as outlined in the Kreyca-Kozeschnik model [83] (eqs. (3.12) to (3.14)).

usersigyp.f

The subroutine `usersigyp.f` calculates the strain-hardening contribution using the Taylor equation (eq. (3.15)). Outsourcing the computation of the total dislocation density (`userddtot.f`) and its corresponding saturation value (`userddsat.f`) to nested subroutines resulted in clean code.

userddsat.f

The dynamic equilibrium between dislocation formation and annihilation determines the saturation (maximum) dislocation density ϱ_{sat} [143, 144]. The `userddsat.f` subroutine uses the Newton-Raphson root-finding algorithm (eq. (5.17)) to calculate the maximum achievable value in a time step.

$$\begin{aligned} f &: \mathbb{R} \to \mathbb{R} \\ x &: f(x) = 0 \\ x_1 &= x_0 - f(x_0)/f'(x_0) \\ x_{n+1} &= x_n - f(x_n)/f'(x_n) \end{aligned} \tag{5.17}$$

Root-finding is an iterative process. First, the code requires a starting value, which is either ten times the equilibrium dislocation density or, if available, the dislocation density value of a previous time step. With this input, the code calculates a new value and compares it to the starting value of the current loop. The algorithm accepts the result if the relative change is less than 1×10^{-8}, otherwise, iterates up to 30 times.

Besides being generated, dislocations can also be annihilated until the equilibrium dislocation density ϱ_{eq} is reached, i.e., the state of an ideally recovered material. Therefore, the calculation ensures that neither the total dislocation density nor its saturation value falls below the equilibrium level.

userddtot.f

The calculation of the total dislocation density evolution uses an explicit Runge-Kutta (RK) method (eq. (5.18)) implemented via a Butcher tableau (eq. (5.19)). Each Butcher tableau consists of three parts: the RK matrix $\boldsymbol{A}\,[s \times s]$, the node vector $\boldsymbol{c}\,[s \times 1]$, and the weight vector $\boldsymbol{b}\,[s \times 1]$, with their characteristic coefficients a_{jl}, c_j, and b_j. For explicit methods, the RK matrix $\boldsymbol{A}$ is lower triangular [145–147].

The advantage of this approach is that any explicit RK method, e.g., Forward Euler or fourth order RK, no matter how complex, is defined using the corresponding Butcher table (eqs. (5.20) and (5.21)). Consequently, switching between already implemented solvers requires only a minor adjustment in the simulation setup.

$$\begin{aligned} y'(t) &= f(t, y(t)), \quad y(t_0) = y_0, \quad y : \mathbb{R} \to \mathbb{R}^{\mathrm{d}} \\ t_{n+1} &= t_n + h \\ y_{n+1} &= y_n + h \sum_{j=1}^{s} b_j k_j \\ k_j &= f\left(t_n + hc_j, y_n + h \sum_{l=1}^{s} a_{jl} k_l\right) \quad \text{for } j = 1 \ldots s \end{aligned} \tag{5.18}$$

$$\begin{array}{c|c} \boldsymbol{c} & \boldsymbol{A} \\ \hline & \boldsymbol{b}^{\mathrm{T}} \end{array} = \begin{array}{c|ccccc} c_1 & & & & & \\ c_2 & a_{21} & & & & \\ c_3 & a_{31} & a_{32} & & & \\ \vdots & \vdots & & \ddots & & \\ c_s & a_{s1} & a_{s2} & a_{s3} & a_{s,s-1} & \\ \hline & b_1 & b_2 & \cdots & b_{s-1} & b_s \end{array} \qquad \begin{aligned} c_1 &= 0 \\ a_{jl} &= 0 \quad \text{for all} \quad j \geq l \end{aligned} \tag{5.19}$$

$$\begin{array}{c|c} 0 & \\ \hline & 1 \end{array} \tag{5.20}$$

$$\begin{array}{c|cccc} 0 & & & & \\ 1/2 & 1/2 & & & \\ 1/2 & 0 & 1/2 & & \\ 1 & 0 & 0 & 1 & \\ \hline & 1/6 & 1/3 & 1/3 & 1/6 \end{array} \tag{5.21}$$

The simulation model resulting from this study predicts the temporal and spatial evolution of the dislocation density between the lower and upper barrier, i.e., the equilibrium dislocation density ϱ_{eq} and saturation dislocation density ϱ_{sat} (eq. (5.22)). Often, simulations start with a fully recovered material, i.e., a state of dislocation equilibrium. As this is not the general case, the algorithm also readily handles arbitrary values ϱ_{arb} (eq. (5.23)), a prerequisite for successful multistep computations. Finally, the dislocation density at the end of the current time step results from evaluating the characteristic equation (eq. (5.24) cf. eqs. (3.16) and (3.17)).

$$y(t) = \varrho(t), \quad \varrho(t) \geq \varrho_{\mathrm{eq}} \tag{5.22}$$

$$y(t_0) = \varrho(t_0) = \varrho_{\mathrm{eq}} \vee \varrho_{\mathrm{arb}} \tag{5.23}$$

$$y'(t) = \dot{\varrho}(t) = \mathfrak{A}\sqrt{\varrho(t)} - \mathfrak{B}\varrho(t) - \mathfrak{C}\left(\varrho(t)^2 - \varrho_{\mathrm{eq}}^2\right) \tag{5.24}$$

usernuc.f

The Gleixner et al. model [90] for multiple vacancy paths to the critical embryo (eq. (3.37)) forms the basis of the subroutine `usernuc.f` that calculates the nucleation rate J_i. The implementation in this study calculates the number of nucleated cavities over a given time step N_i from the product of the nucleation rate at the beginning of the time step with its respective duration Δt_i. The total number of nuclei N results from the summation over the entire simulation time and is given by

$$N = \sum_{i=1}^{n} J_i \Delta t_i. \tag{5.25}$$

Nucleation occurs only after surmounting the nucleation barrier, which requires a specific amount of driving force. According to the respective literature, typical driving forces for void nucleation are the plastic strain [148,149], the normal stress [6,122,150], and the hydrostatic stress [151–153]. The model presented here combines the latter approach with that of Tang-Plumtree [16]. Therefore, the *effective* driving force is the sum of hydrostatic and chemical stress (eq. (5.31)).

There are three scenarios when evaluating the pressure balance at the void surface: sintering ($\sigma_{\text{eff}} - p_\infty < 0$), equilibrium/no nucleation ($\sigma_{\text{eff}} - p_\infty = 0$), and nucleation ($\sigma_{\text{eff}} - p_\infty > 0$). However, an assumption prohibits the first case; voids cannot sinter once formed. Consequently, the first two cases merge, and the driving force of the nucleation rate is either zero or calculated according to an adapted version of the Tang-Plumtree model for excess vacancies (eqs. (5.26) to (5.31)).

$$\begin{align}
\sigma_{\text{chem}} &= k_{\text{B}}T/\Omega \ln\left(1 + c_{\text{ex}}/c_{\text{gb}}\right) \tag{5.26}\\
c_{\text{ex}} &= 10^{-4}\dot{\varepsilon}_{\text{loc}}L^2/\left(D_{\text{v0}}\exp\left(-Q_{\text{mig}}/\left(RT\right)\right)\right) \tag{5.27}\\
c_{\text{vac}} &= \begin{cases} 10^{-4} \\ 5\times 10^{-4}\left(1-\exp\left(-8\times 10^{-8}\left(10^{-14}\varrho\right)^5\right)\right) \end{cases} \tag{5.28}\\
L &= \left(2\varrho^{1/2}\right)^{-1} \tag{5.29}\\
c_{\text{gb}} &= c_0\exp\left(\sigma_{\text{h}}\Omega/\left(k_{\text{B}}T\right)\right) \tag{5.30}\\
\sigma_{\text{eff}} &= \sigma_{\text{h}} + \sigma_{\text{chem}} \tag{5.31}\\
df &= \mathrm{R}T\ln\left|\sigma_{\text{eff}}/p_\infty\right|/V_{\text{mole}} \tag{5.32}\\
V_{\text{mole}} &= \mathrm{N_A}\Omega \tag{5.33}\\
\Omega &= a^3/Z \tag{5.34}\\
& \tag{5.35}
\end{align}$$

Here, c_{vac} is the vacancy concentration according to, respectively, Tang and Plumtree [16] and Ungár et al. [126], $\dot{\varepsilon}_{\text{loc}}$ is the local strain rate, L is the average diffusion distance, D_{v0} is the pre-exponential term for the volume diffusion coefficient, $Q_{\text{mig}} = Q_{\text{v}} - Q_{\text{f}}$ is the activation energy for vacancy migration, and c_0 is the vacancy concentration in equilibrium with the grain boundary in conjunction with a hydrostatic stress σ_{h}. Q_{v} denotes the activation energy for volume diffusion (or lattice diffusion), and $Q_{\text{f}} = \mathrm{e_c}\mathrm{N_A}E_{\text{f}}$ is the activation energy for vacancy formation, where $\mathrm{e_c}$ is the elementary (Coulomb) charge, and $\mathrm{N_A}$ is the Avogadro constant. See table 5.1 for values and references.

userout.f

Before entering the nested subroutine `userout.f`, the `usermat.f` code checks whether the solution converges or requires a bisection. In case of convergence, `userout.f`

Die approbierte gedruckte Originalversion dieser Dissertation ist an der TU Wien Bibliothek verfügbar.
The approved original version of this doctoral thesis is available in print at TU Wien Bibliothek.
TU Bibliothek WIEN Your knowledge hub

manages the collective transfer of all user state variables to the next higher level of the FEA.

CHAPTER 6

Results

The following chapter is divided into three sections. It starts with the experimental observations, moves on to the analytical calculations, and finally presents the results of the computer simulations.

6.1 Experimental

The experiments conducted by Wiehoff [127] and this study combine existing and new experimental setups. While the repetition of known tests helped assess the position within a wide range of publications, new test setups allowed the opportunity to explore novelties. Furthermore, experimentation is always relevant even in a simulation-oriented environment because the knowledge gained is essential for a deeper understanding of the subject.

Mechanical Testing

The following section presents the results of four hot tensile test series. The standard series uses a specimen with a nominal diameter of 8 mm and a cooling rate of $1\,\mathrm{K\,s^{-1}}$. The novelty of the other tests, as explained in section 4.1 Mechanical Testing, is the nominal diameter, cooling time, and strain rate. Further processing of the stress-strain curves (fig. B.1) provides a set of meaningful plots (figs. 6.1a to 6.1c). A fourth diagram, the necking assessment, rests on vernier caliper measurements (fig. 6.1d).

The evaluation of all tests reveals that the yield stress (R_{p02}) is between 9.8 MPa and 41 MPa within the observed test range. The lowest value belongs to the specimen with a nominal diameter of 16 mm, strained at 1050 °C; the highest value belongs to the specimen with a nominal diameter of 8 mm, cooled within 800 s and strained at 850 °C. The maximum yield stress of each curve varies from 27 MPa to 41 MPa. All but one series reach their maximum at 850 °C, the one strained at $1\times10^{-4}\,\mathrm{s^{-1}}$ already at 800 °C. Beyond the above temperatures, the yield stress gradually decreases to about 9.8 MPa to 16 MPa at 1050 °C, the highest temperature studied. The parallel course of the two 800 s series is noteworthy, with the thicker samples always yielding before the thinner ones (fig. 6.1a). As with the yield stress, the ultimate tensile strength decreases with temperature, from about 65 MPa to 88 MPa at 800 °C to about 26 MPa to 34 MPa at 1050 °C. The data further shows that the applied strain rate affects the achievable UTS, with slower strained samples showing reduced strength (fig. 6.1b). Unlike the previous two figures, the resistance to deformation cannot be read directly from the stress-strain curves (fig. B.1). The evaluation of this value, which represents the area under the stress-strain curve before UTS is reached, indicates a reduced strain effort at low strain rates, i.e., $1 \times 10^{-4}\,\mathrm{s}^{-1}$, between 800 °C and 950 °C (fig. 6.1c). Besides analyzing the stress-strain curves, the postmortem measured fracture diameter provides valuable insights. The slowest strained series and the series with the thick specimens have an S-shaped ductility curve; the other two are double S-shaped. Interestingly, thin specimens strained at $3 \times 10^{-4}\,\mathrm{s}^{-1}$ have increased reduction of area values at 900 °C. The same two sets of tests further indicate that the obtained results are independent of the cooling strategy (800 s or $1\,\mathrm{K\,s}^{-1}$). The comparison of the nominal diameter 8 mm and 16 mm siblings shows that the thicker specimens are less ductile in the temperature range 850 °C to 950 °C. Furthermore, linearly cooled specimens ($1\,\mathrm{K\,s}^{-1}$) strained at $1 \times 10^{-4}\,\mathrm{s}^{-1}$ and $3 \times 10^{-4}\,\mathrm{s}^{-1}$ show reduced ductility at lower strain rates, but the difference decreases with increasing temperature (fig. 6.1d).

Precipitation Analysis

The above results provide a good first overview of the studied steel. However, microalloyed steels are precisely composed materials with excellent performance despite—or even because of—the minimal use of alloying elements, so it is worth taking a closer look at the precipitates (section 4.2 Precipitation Analysis). At first glance, the number of precipitates decreases with increasing holding time (fig. 6.2). A thorough evaluation shows that the particle size distribution is almost identical for the first holding times (1 min and 5 min) and that both populations are slightly right-skewed. Above 5 min, the mean radius increases proportionally with time. It is also noticeable that the interquartile range of the last series (30 min holding time) is slightly wider than that of the other three populations. The results further indicate that the measurements and the MatCalc thermokinetic simulations [139–141,154–156] agree for a holding time of 15 min, while the radii of the other series are either overestimated or underestimated (fig. 6.3).

6.2 Calculations

Raj-Ashby and Steady-State Nucleation Model

Before turning to the computer simulation results, it is vital to compare different model approaches. The following section reviews relevant models for cavity nucleation using austenite (table 5.1) with a grain size of 1 mm. The results also demonstrate why discarding some models and searching for other approaches was necessary.

As mentioned earlier, the Raj-Ashby model (eq. (3.30)) is a landmark in cavity formation research, but unlike the Becker-Döring model (eq. (3.36)), it studies only a

Die approbierte gedruckte Originalversion dieser Dissertation ist an der TU Wien Bibliothek verfügbar.
The approved original version of this doctoral thesis is available in print at TU Wien Bibliothek.
TU Bibliothek WIEN Your knowledge hub

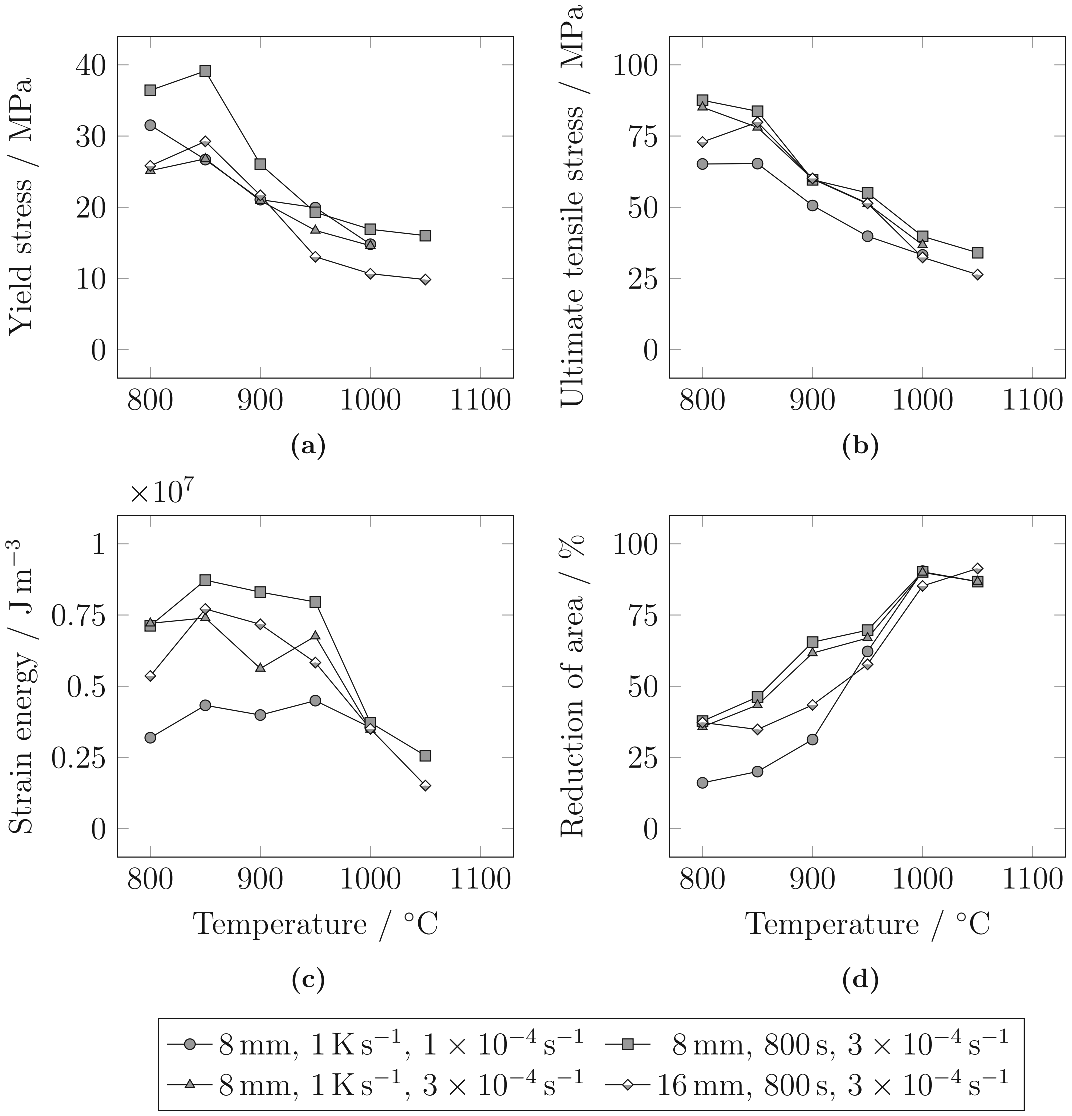

(a) (b)

(c) (d)

Figure 6.1. Evaluation of hot tensile tests. (a) Yield strength, (b) ultimate tensile stress (UTS), (c) strain energy up to UTS, (d) reduction of area.

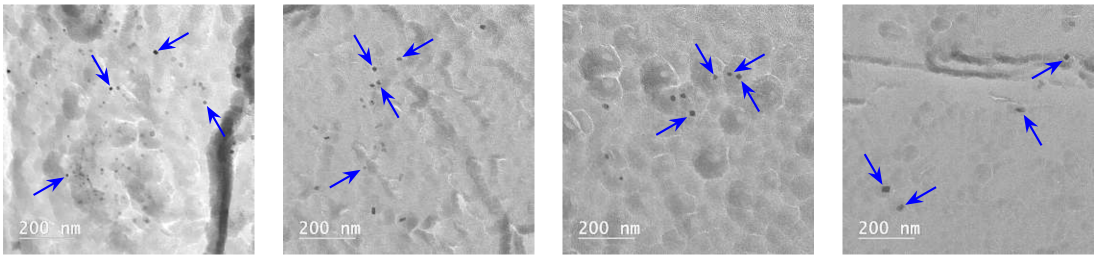

(a) (b) (c) (d)

Figure 6.2. Nb(C,N)-precipitates (arrows) visualized via carbon replica foils of a microalloyed steel after an isothermal holding time of (a) 1 min, (b) 5 min, (c) 15 min, and (d) 30 min at 950 °C.

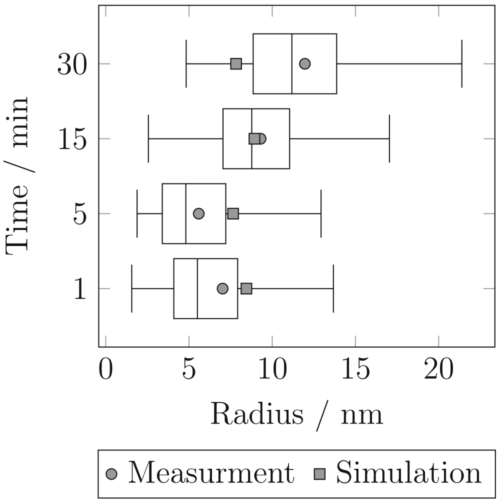

Figure 6.3. Radius of Nb(C,N) precipitates after isothermal holding (1 min, 5 min, 15 min, and 30 min) at 950 °C and straining to failure at $3 \times 10^{-4}\,\mathrm{s}^{-1}$ (1284 s, 1025 s, 1519 s, and 1070 s). The box plots are derived from the measurements. The simulated mean values originate from MatCalc thermokinetic simulations.

two-dimensional case. Therefore, this study implements a slightly adapted Raj-Ashby model that uses the nucleation sites per volume ($c_{\mathrm{max}} = \lambda^{-3}$) instead of per area ($c_{\mathrm{max}} = \lambda^{-2}$), where λ is the spacing between potential nucleation sites.

The following evaluation uses stresses between 4 GPa and 10 GPa within a homologous temperature range of 0.6 to 1 and a void tip angle ψ of 70° (fig. 6.4a). As expected, the nucleation rate increases from low to high temperatures and stresses. Therefore, the lowest nucleation rate ($7 \times 10^{-22}\,\mathrm{s}^{-1}\,\mathrm{m}^{-3}$) within the observed test range occurs at the lowest applied stress (4 GPa) and temperature ($T/T_{\mathrm{m}} = 0.6$). Even a homologous temperature equal to one triggers only meager nucleation rates at this stress level ($3 \times 10^{2}\,\mathrm{s}^{-1}\,\mathrm{m}^{-3}$). However, increasing the applied stress to 6 GPa changes the picture. The nucleation rate is now well above unity ($5 \times 10^{7}\,\mathrm{s}^{-1}\,\mathrm{m}^{-3}$ to $6 \times 10^{19}\,\mathrm{s}^{-1}\,\mathrm{m}^{-3}$) in the test temperature spectrum. Although further increases in applied stress result in even higher nucleation rates, the achievable gain gradually decreases. Finally, applying a stress of 10 GPa results in nucleation rates between $2 \times 10^{22}\,\mathrm{s}^{-1}\,\mathrm{m}^{-3}$ and $4 \times 10^{28}\,\mathrm{s}^{-1}\,\mathrm{m}^{-3}$ over the observed temperature range. In addition to the stress variation, the void tip angle provides valuable insight. Void tip angle variations between 40° and 70° at a stress of 6 GPa show that small void tip angles cause high nucleation rates even at moderate stresses (fig. 6.4b). The combination of a void tip angle $\psi = 40°$ and a stress of 6 GPa results in nucleation rates between $1 \times 10^{27}\,\mathrm{s}^{-1}\,\mathrm{m}^{-3}$ and $2 \times 10^{31}\,\mathrm{s}^{-1}\,\mathrm{m}^{-3}$. These rates are even higher than those observed for a stress of 10 GPa at a void tip angle of 70°. Calculations show that the Raj-Ashby model (eq. (3.30)) and the steady-state nucleation model (eq. (3.41)) yield similar nucleation rates. Therefore, it is sufficient for the reader to consider only the latter.

The preceding observations reveal the need for unattainably high stresses, as addressed in chapter 7 Discussion, but what if the applied stress amplifies within the microstructure and nucleation does not occur instantaneously? Consider an applied $\sigma_{\infty} = 100\,\mathrm{MPa}$ stress and derive the critical stress concentration required

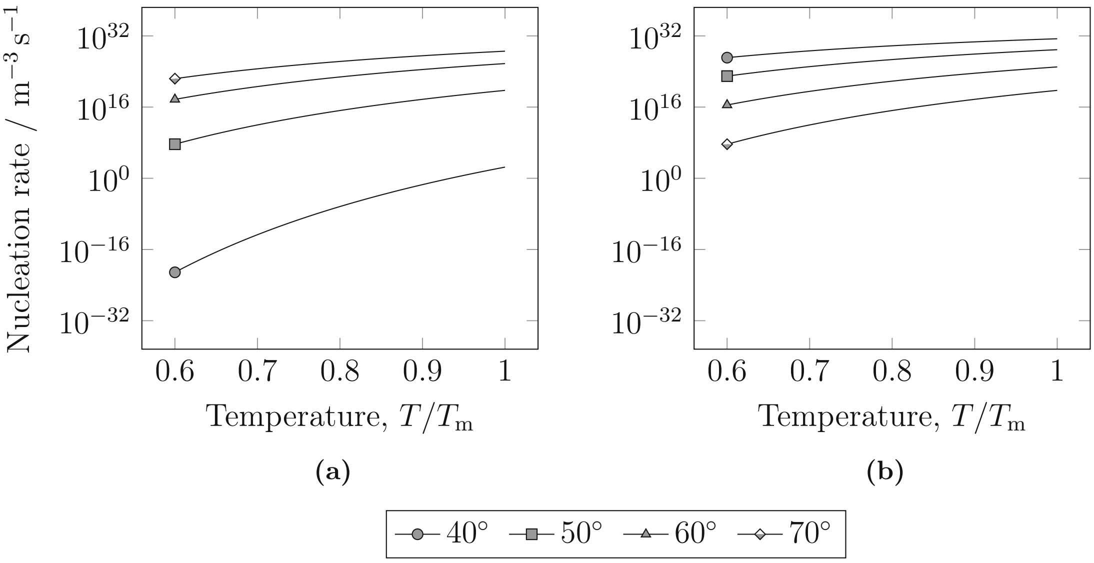

Figure 6.4. Nucleation rate in austenite according to the adapted Raj-Ashby model as a function of (a) stress $\sigma(\psi = 70°)$ and (b) void tip angle $\psi(\sigma = 6\,\mathrm{GPa})$ under the assumption that $0.5\,c_{\mathrm{max}}$ subcritical nucleation sites per unit grain boundary are available for further nucleation.

to nucleate a cavity by vacancy condensation alone from eq. (3.30). Nucleation by vacancy condensation alone requires stress amplifications between 60 and 160 times, depending on the prevailing temperature and strain rate (fig. 6.5). An analysis of the underlying equation (eq. (3.30)) reveals that the stress concentration is inversely proportional to the applied stress, with temperature and nucleation time having little influence. In other words, lower stresses, as observed in fig. B.1, require even higher stress concentrations to allow cavity nucleation by vacancy condensation alone. Thus, for applied stresses of the given magnitude, nucleation by vacancy condensation is impossible unless the stresses are locally amplified by two orders of magnitude.

The above considerations illustrate the high stress concentration required for vacancy condensation under steady-state conditions. However, they do not provide information on the time required for a cluster to adapt to a changing stress environment and eventually be ready to nucleate another cavity. The required time is derived from the transient solution of the Fokker-Plank equation (eqs. (3.40), (3.42), and (3.43)) [1]. Calculation of the lower and upper incubation time limits for an applied stress magnitude of 100 MPa according to the above equations shows that the incubation time for a previously unstressed sample varies between 2×10^{-6} s and 7×10^{2} s in a homologous temperature range of 0.6 to 1 (fig. 6.6). Further calculations show that spontaneous nucleation requires much higher stresses. Stress amplitudes of 1000 MPa already trigger nucleation within 1×10^{-9} s and 3×10^{-4} s in the mentioned temperature range.

The previous figures show nucleation rates based on applied stresses, required stress concentrations, and incubation times. The transition time from nonsteady to steady-state nucleation is also important. The performed evaluation shows that a more or less temperature-independent transition from a sparse nonsteady to a fully established steady-state nucleation regime occurs between four to eight times

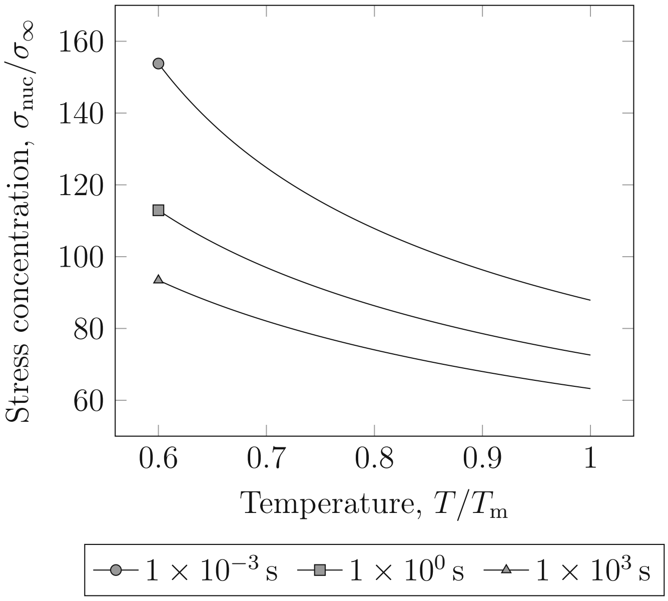

Figure 6.5. Stress concentration $\sigma_{\mathrm{nuc}}/\sigma_\infty$ of an externally applied stress $\sigma_\infty = 100\,\mathrm{MPa}$ necessary to nucleate a cavity after 1×10^{-3} s to 1×10^{3} s by vacancy condensation. Based on calculations according to Riedel [1].

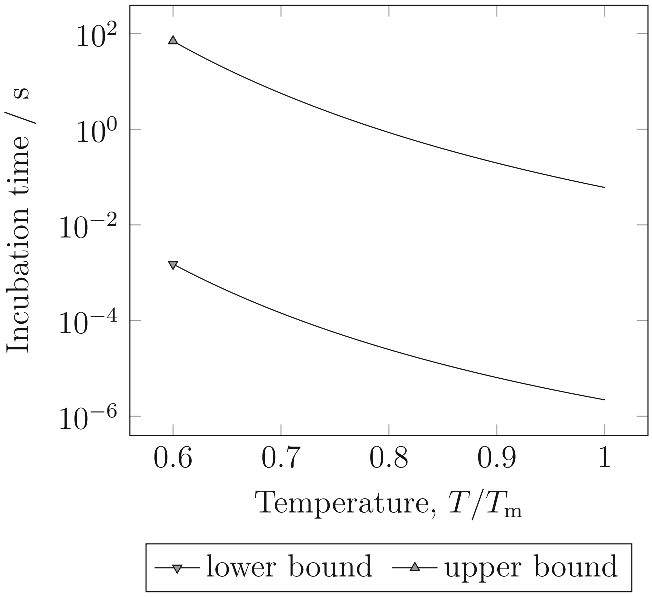

Figure 6.6. The lower and upper bound of the incubation time with an externally applied stress of 100 MPa. Calculations according to Riedel [1].

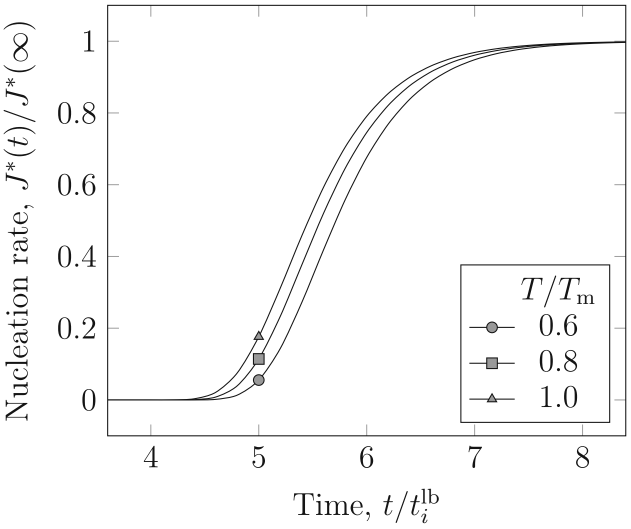

Figure 6.7. Transition time from nonsteady to steady-state nucleation rate for the homologous temperatures 0.6, 0.8, and 1.0. Based on calculations according to Riedel [1].

the lower incubation time-bound (fig. 6.7). Riedel [1] also provides equations to estimate the time required to build or relax local and global stresses. The evaluation shows that for austenite loaded at 100 MPa, local stresses are relieved seven orders of magnitude faster than they can be built up. Global stresses are relieved eleven orders of magnitude faster.

Becker-Döring Nucleation Model

Besides the Raj-Ashby model, the Becker-Döring model, implemented by Gleixner et al. [90], is a reasonable choice. Applying the Zeldovich factor and the two different formulations (eqs. (3.36) and (3.37)) makes it appear more comprehensive. The difference between the two Gleixner et al. implementations is not noticeable, at least in this study, so fig. 6.8 shows only the single diffusion path version. Compared to fig. 6.4a, the data analysis for an applied stress of 6 GPa shows that the Becker-Döring model (fig. 6.8) is more conservative than the Raj-Ashby model, requiring smaller void tip angles (fig. 3.23) to achieve similar nucleation rates. According to the evaluation, stable cavity nucleation over the observed temperature range requires void tip angles ψ less than 50°.

Tang-Plumtree Excess Vacancy Model

According to the Tang-Plumtree model, the locally prevailing effective stress σ_eff is a function of the applied σ_∞ and the chemical stress σ_chem. The chemical stress depends on the vacancy concentration ratio $c_\mathrm{ex}/c_\mathrm{gb}$, which depends on the local strain rate $\dot{\varepsilon}_\mathrm{loc}$ and the dislocation density ϱ. Of course, both also depend on a variety of material parameters (eqs. (3.46) to (3.50)). An evaluation of the model shows that low dislocation density values, low temperatures, and high strain rates are advantageous for achieving high vacancy concentration ratios. Towards high temperatures, the maximum achievable vacancy concentration ratio decreases

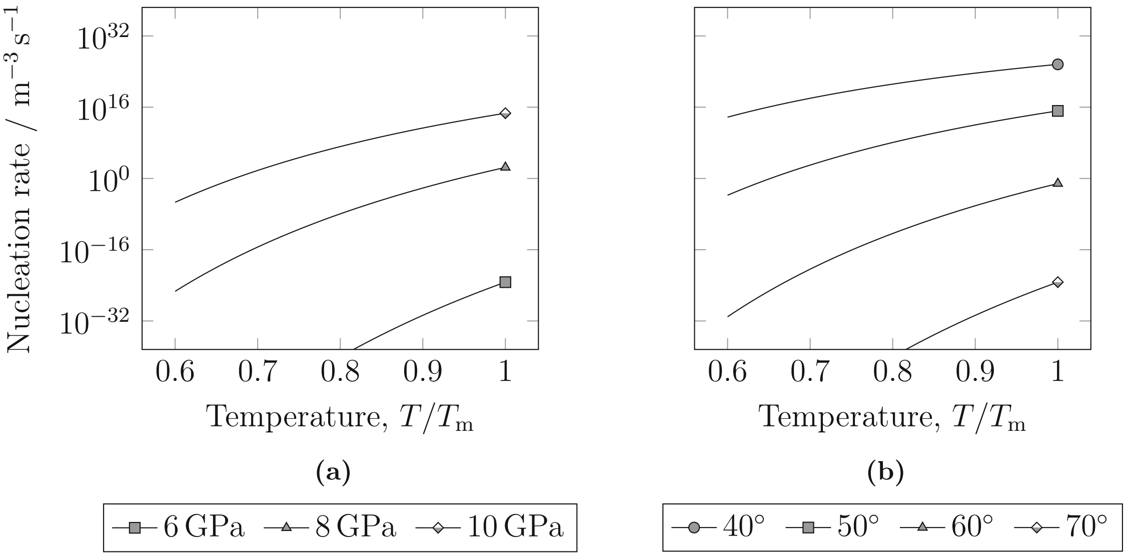

(a)

(b)

Figure 6.8. Nucleation rate in austenite according to the Becker-Döring model for (a) a stress σ ($\psi = 70°$) and (b) a void tip angle ψ ($\sigma = 6\,\mathrm{GPa}$). Based on calculations according to Gleixner et al. [90].

significantly (figs. 6.9a and 6.9b). As described later in chapter 7 Discussion, the correlation is straightforward, but the sudden cutoff in fig. 6.9d compared to fig. 6.9c is not intuitive. At low dislocation densities, a strain rate of $1 \times 10^2\,\mathrm{s}^{-1}$ maintains at least a small stress ratio $\sigma_{\mathrm{eff}}/\sigma_\infty$ up to the melting temperature (fig. 6.9c), which is impossible at high dislocation densities, where the stress ratio drops sharply already at intermediate temperatures. Above 0.8 homologous temperature, even the highest applied strain rate cannot increase the stress ratio beyond unity (fig. 6.9d).

6.3 Computer Simulation

Cooling Rate Sensitivity

Since the cooling rate variation results in different times to reach the test temperature, the start of the strain cycle defines the zero time (fig. 6.10a); for cooling rates below $1\,\mathrm{K\,s^{-1}}$, the phase fraction, number density, and mean radius begin to grow within the cooling cycle. The higher the rate, the later the growth starts. Although the evolution is different, the final values are almost identical, except for a reduced number density and increased mean radius at the lowest cooling rate (figs. 6.10b to 6.10d).

Finite Element Analysis

All computer simulations in this study utilize the Ansys element type *PLANE182*, a two-dimensional four-node structural solid in a plane-strain configuration. The plane-strain approach is legitimate because the microstructure in the critical zone, which is prone to transverse cracking, consists mainly of columnar grains [128].

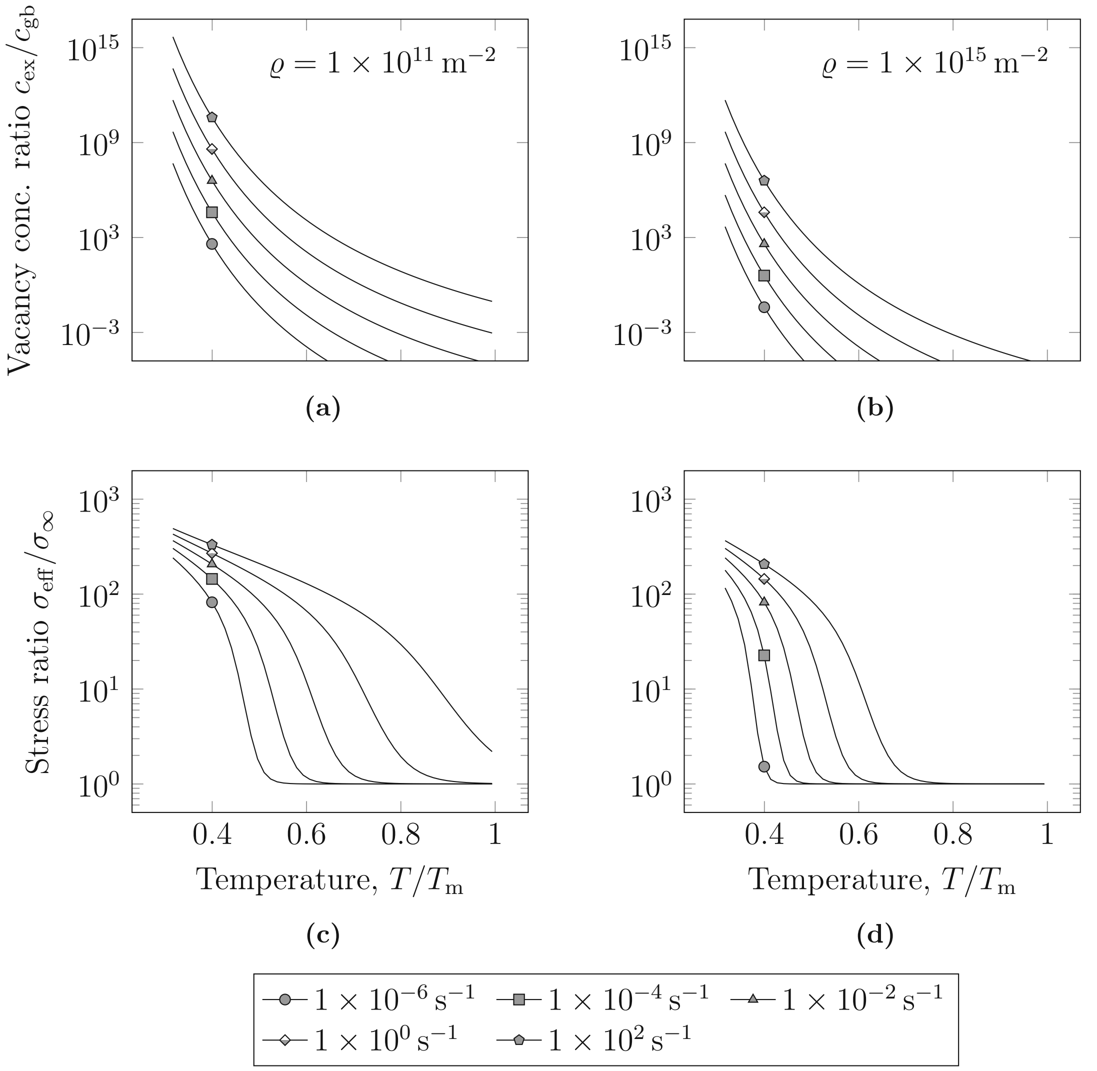

Figure 6.9. (a), (b) Strain rate dependence of the vacancy concentration ratio c_{ex}/c_{gb} and (c), (d) stress ratio $\sigma_{eff}/\sigma_\infty$ in austenite for homologous temperatures, T/T_m, between 0.3 and 1. The applied dislocation density ϱ is (a), (c) $1 \times 10^{11}\,\mathrm{m}^{-2}$ or (b), (d) $1 \times 10^{15}\,\mathrm{m}^{-2}$. The applied stress σ_∞ is always 100 MPa. Based on calculations according to Tang and Plumtree [16].

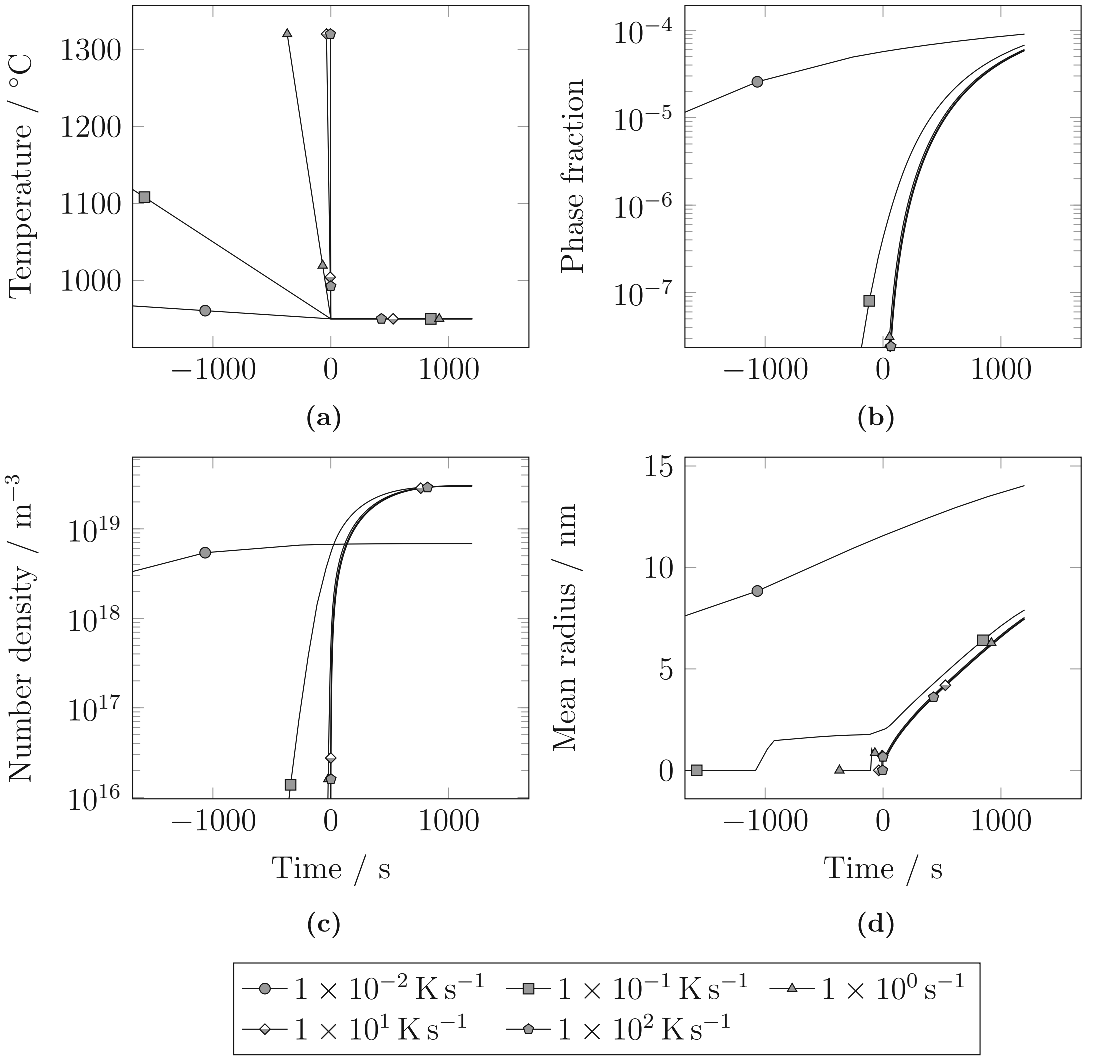

Figure 6.10. Influence of the cooling rate on the evolution of Nb(C,N)-precipitates at dislocation sites. (a) Temperature profile of the applied cooling regime, (b) phase fraction, (c) number density, and (d) mean radius of the precipitates.

Single-Element Test

The Ansys material model development in this study is based on MatCalc computer simulations. All model verification tests are performed on a single element (fig. 6.12). The deformation modes are tension ① ③, compression ④, and constant strain holding ②. The maximum accumulated strain is slightly less than 0.8 (fig. 6.11).

Due to the geometry independence of MatCalc, the validation of the material model with Ansys requires a temporary code adjustment, i.e., replacing the equivalent plastic strain from Ansys with MatCalc values (fig. 6.11). The evaluation of pure fcc iron at 950 °C shows that the dislocation density and yield stress contribution calculated with Ansys agree with those obtained from the MatCalc reference. Ansys cannot achieve the same values as the corresponding MatCalc simulation without suppressing the influence of geometry (fig. 6.12). The discussion on this topic follows in section 7.3 Finite Element Analysis.

Die approbierte gedruckte Originalversion dieser Dissertation ist an der TU Wien Bibliothek verfügbar.
The approved original version of this doctoral thesis is available in print at TU Wien Bibliothek.
TU Bibliothek Your knowledge hub WIEN

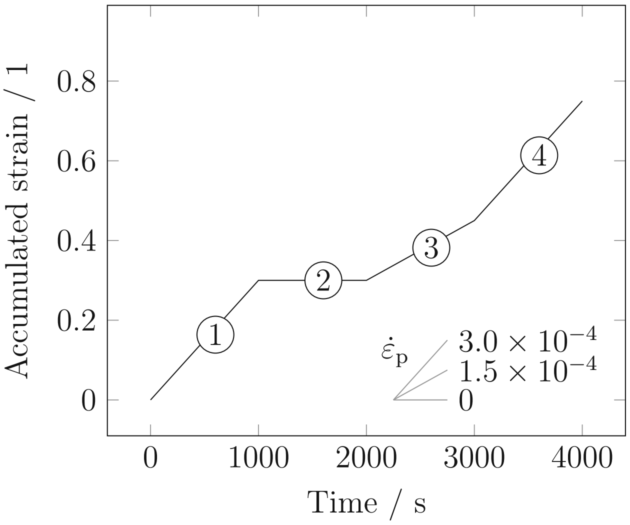

Figure 6.11. Accumulated strain.

Computation with Representative Area Model

After successfully implementing the material model in the single-element setup, it can now be applied to any geometry; in this study, the representative area model of a coarse-grain annealed microalloyed steel with a grain size of 1 mm. Based on an idealized assumption, the grains are regular hexagonal prisms (figs. 5.1a and 5.1b).

All computer simulations focused on the critical tensile loading conditions during the straightening process in curved strand casters. The simulation virtually loads the microstructure with up to 5 % strain in the vertical direction at nine strain rates ($1 \times 10^{-6}\,\mathrm{s}^{-1}$ to $1 \times 10^{2}\,\mathrm{s}^{-1}$), five temperatures (800 °C to 1200 °C), and three static Coulomb friction coefficients ($\mu = 0$, 0.3, and 1). The simulations also include two vacancy concentration approaches (Tang-Plumtree [16] and Ungár et al. [126]). The material parameters used are summarized in table 5.1.

The following section presents the simulation results of dislocation density and hydrostatic stress as a function of strain rate and temperature at 5 % strain, the maximum strain applied in the simulations (figs. 6.13 to 6.15).

A comparison of the dislocation density shows similar results for all applied friction coefficients ($\mu = 0$, 0.3, and 1). The maximum dislocation density ρ_max for each friction coefficient is highest at the lowest temperature (800 °C) and the highest strain rate ($1 \times 10^{2}\,\mathrm{s}^{-1}$). The dislocation density saturates for strain rates above $1\,\mathrm{s}^{-1}$. The global maximum ($9.6 \times 10^{14}\,\mathrm{m}^{-2}$) occurs at frictionless contact (figs. 6.13a, 6.14a, and 6.15a).

The ratio between maximum and minimum dislocation density $\rho_\mathrm{max}/\rho_\mathrm{min}$ is similar to the maximum dislocation density. The ratio is lowest at low strain rates and vice versa. The ratio is between 3.5 to 40 at $1 \times 10^{-6}\,\mathrm{s}^{-1}$ and 960 to 1100 at $1 \times 10^{2}\,\mathrm{s}^{-1}$ for frictionless contacts and between 1.6 to 20 at $1 \times 10^{-6}\,\mathrm{s}^{-1}$ and 860 to 1100 at 1×10^{2} for the friction coefficient $\mu = 1$ (figs. 6.13b, 6.14b, and 6.15b).

Also, the shape of the maximum hydrostatic stress $\sigma_\mathrm{h}^\mathrm{max}$ is similar to the dislocation density. An evaluation of the stress shows that the maximum values occur at the lowest temperature under frictionless conditions. Reducing the strain rate or

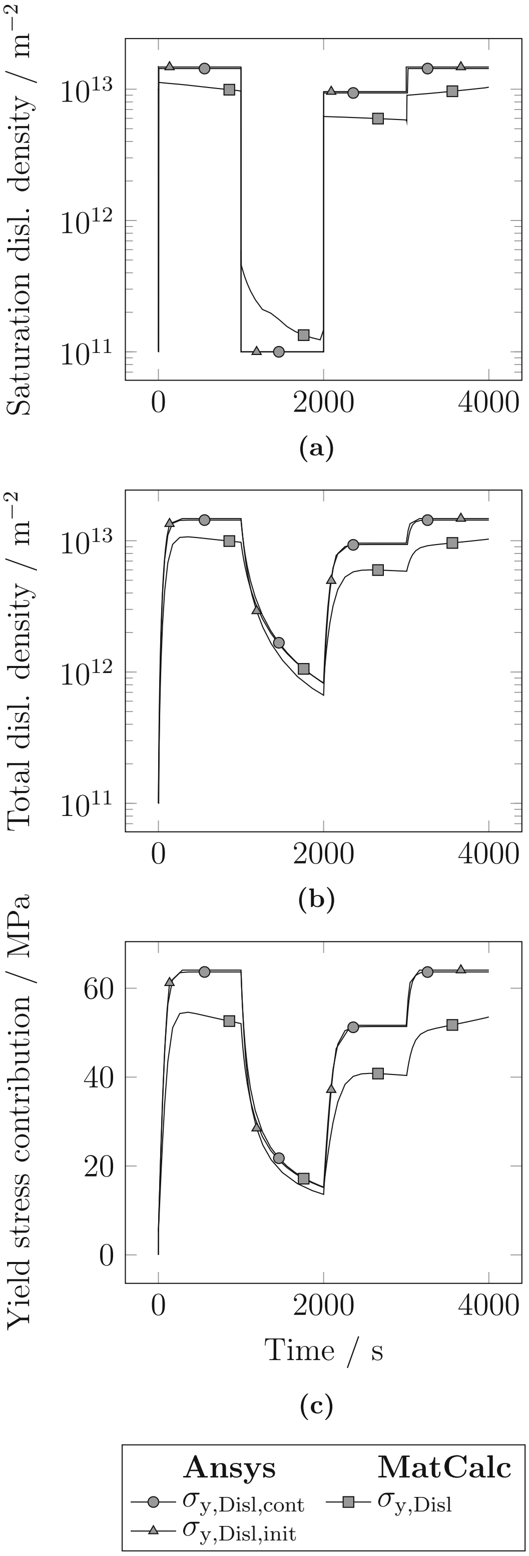

Figure 6.12. Comparison of two Ansys single-element tests with a MatCalc reference calculation utilizing a constant strain rate. In the first case, *const*, Ansys was forced to utilize the same (plastic equivalent) strain rate as MatCalc. In the second case, *init*, only the initial value was the same. (a) Saturation dislocation density, (b) total dislocation density, and (c) yield stress contribution of dislocations.

Die approbierte gedruckte Originalversion dieser Dissertation ist an der TU Wien Bibliothek verfügbar.
The approved original version of this doctoral thesis is available in print at TU Wien Bibliothek.
TU Bibliothek Your knowledge hub
TU WIEN

increasing the temperature or the friction coefficient reduces the achievable stress. The global maximum hydrostatic stress (100 MPa) occurs at frictionless contact at 800 °C and $1 \times 10^{2}\,\mathrm{s}^{-1}$ (figs. 6.13c, 6.14c, and 6.15c).

The ratio between the maximum hydrostatic stress and the value of the grain center is approximately three across all temperatures and strain rates for frictionless contact. For frictional contacts, the shape is similar to the maximum hydrostatic stress. For $\mu = 0.3$, the ratio is between 1.4 to 2.4 at $1 \times 10^{-6}\,\mathrm{s}^{-1}$ and 3.2 to 3.3 at $1 \times 10^{2}\,\mathrm{s}^{-1}$. For $\mu = 1$, the ratio is between 1.2 to 1.9 at $1 \times 10^{-6}\,\mathrm{s}^{-1}$ and 3.2 to 3.3 at $1 \times 10^{2}\,\mathrm{s}^{-1}$.

The effect of the friction coefficient on the ratio between the hydrostatic stress at the center of the specimen and the maximum stress reached is evident. While the stress ratio for the frictionless contact remains nearly constant, the value for the friction contacts decreases toward unity at high temperatures and low strain rates (figs. 6.13d, 6.14d, and 6.15d).

The implemented nucleation model[*] is not directly friction-dependent. Therefore, the remaining section focuses on frictionless contact, where the influence of varying surface energy was studied with $\gamma_{\mathrm{s}} = 0.9\,\mathrm{J\,m^{-2}}$ to $1.02\,\mathrm{J\,m^{-2}}$, while the grain boundary energy ($\gamma_{\mathrm{gb}} = 0.8\,\mathrm{J\,m^{-2}}$) remained unchanged (fig. 6.16).

The Tang-Plumtree vacancy concentration model shows abundant nucleation for both surface energies ($\gamma_{\mathrm{s}} = 0.9\,\mathrm{J\,m^{-2}}$ and $1.02\,\mathrm{J\,m^{-2}}$) at low temperatures and high strain rates. In both cases, the highest number of cavities (1.1×10^{25} and 1.2×10^{25}) nucleate at 900 °C and a strain rate of $1 \times 10^{2}\,\mathrm{s}^{-1}$. The number of nucleated cavities gradually decreases toward high temperatures and low strain rates. Higher surface energy shifts the nucleation to higher strain rates and steepens the transition from abundant to no nucleation (figs. 6.16a and 6.16b).

However, suppose the Ungár et al. model for cold rolling[†] (eq. (3.52)) replaces the Tang-Plumtree model for the generation of excess vacancy concentration (eq. (3.51)). In that case, the cumulative number of cavities shows a distinct profile within the test spectrum, characterized by (1) a maximum at intermediate strain rates, (2) a sharp decline towards low strain rates, and (3) a flat decline towards high strain rates. The number of nucleated cavities strongly depends on the surface energy. The maximum number of cavities (1.0×10^{15} and 4.2×10^{6}) nucleate at 900 °C and a strain rate of $1 \times 10^{-1}\,\mathrm{s}^{-1}$. Towards lower strain rates, the number of nucleated cavities quickly drops towards zero. Towards higher strain rates ($1 \times 10^{2}\,\mathrm{s}^{-1}$), the number decreases between one and three magnitudes of order (figs. 6.16c and 6.16d).

---

[*] Consisting of publications [7, 90] and either [16] or [126].

[†] A function of the dislocation density.

Die approbierte gedruckte Originalversion dieser Dissertation ist an der TU Wien Bibliothek verfügbar.
The approved original version of this doctoral thesis is available in print at TU Wien Bibliothek.
TU Bibliothek, WIEN Your knowledge hub

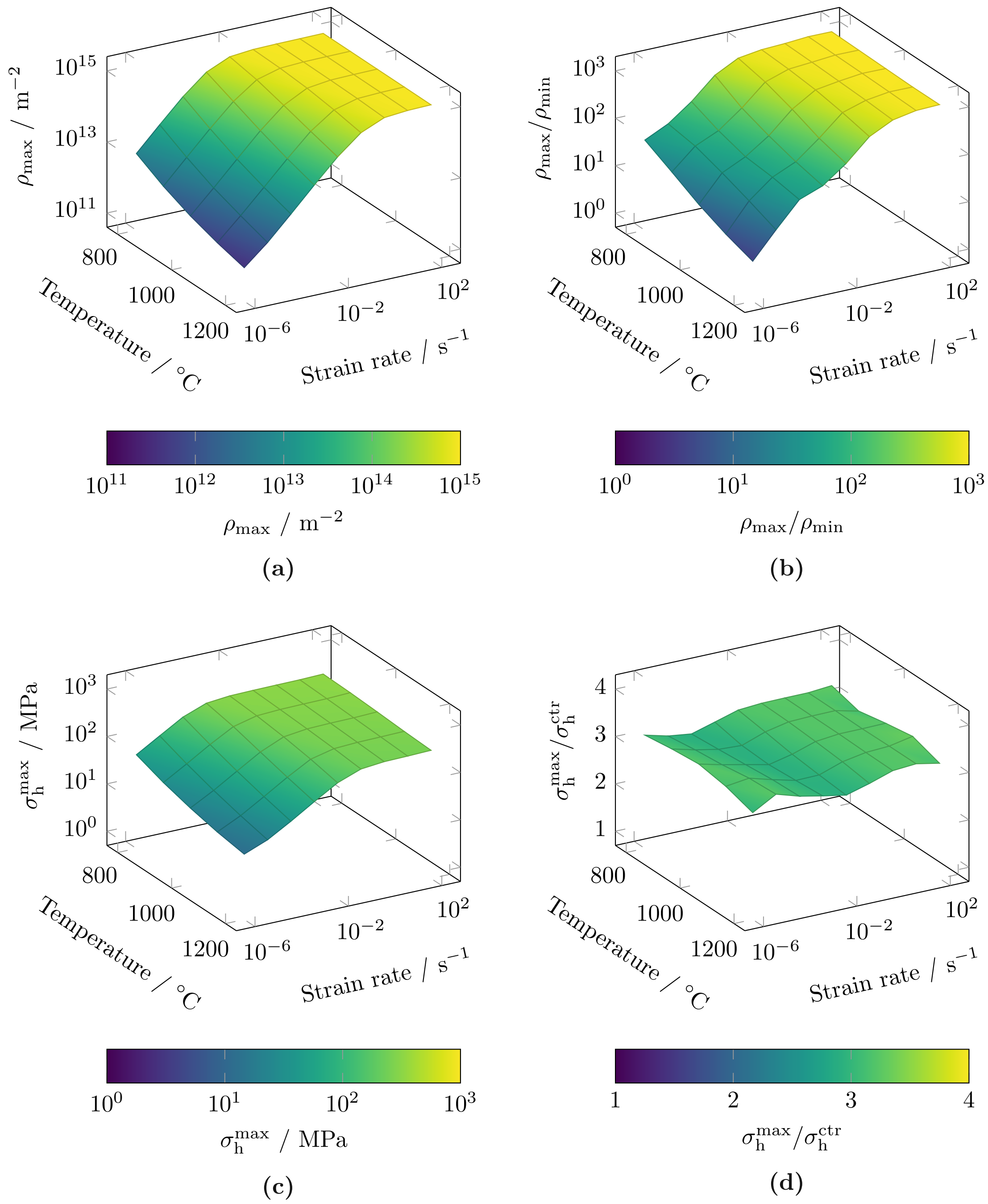

Figure 6.13. Finite element analysis evaluation at 5 % external strain in the vertical direction and friction coefficient $\mu = 0$. (a) Maximum dislocation density $\rho_{\max}$, (b) ratio of maximum and minimum dislocation density $\rho_{\max}/\rho_{\min}$, (c) maximum hydrostatic stress $\sigma_{\mathrm{h}}^{\max}$, (d) ratio of the hydrostatic stress maximum with the value of the grain center $\sigma_{\max}/\sigma_{\mathrm{h}}^{\mathrm{ctr}}$. See also figs. B.2 to B.5.

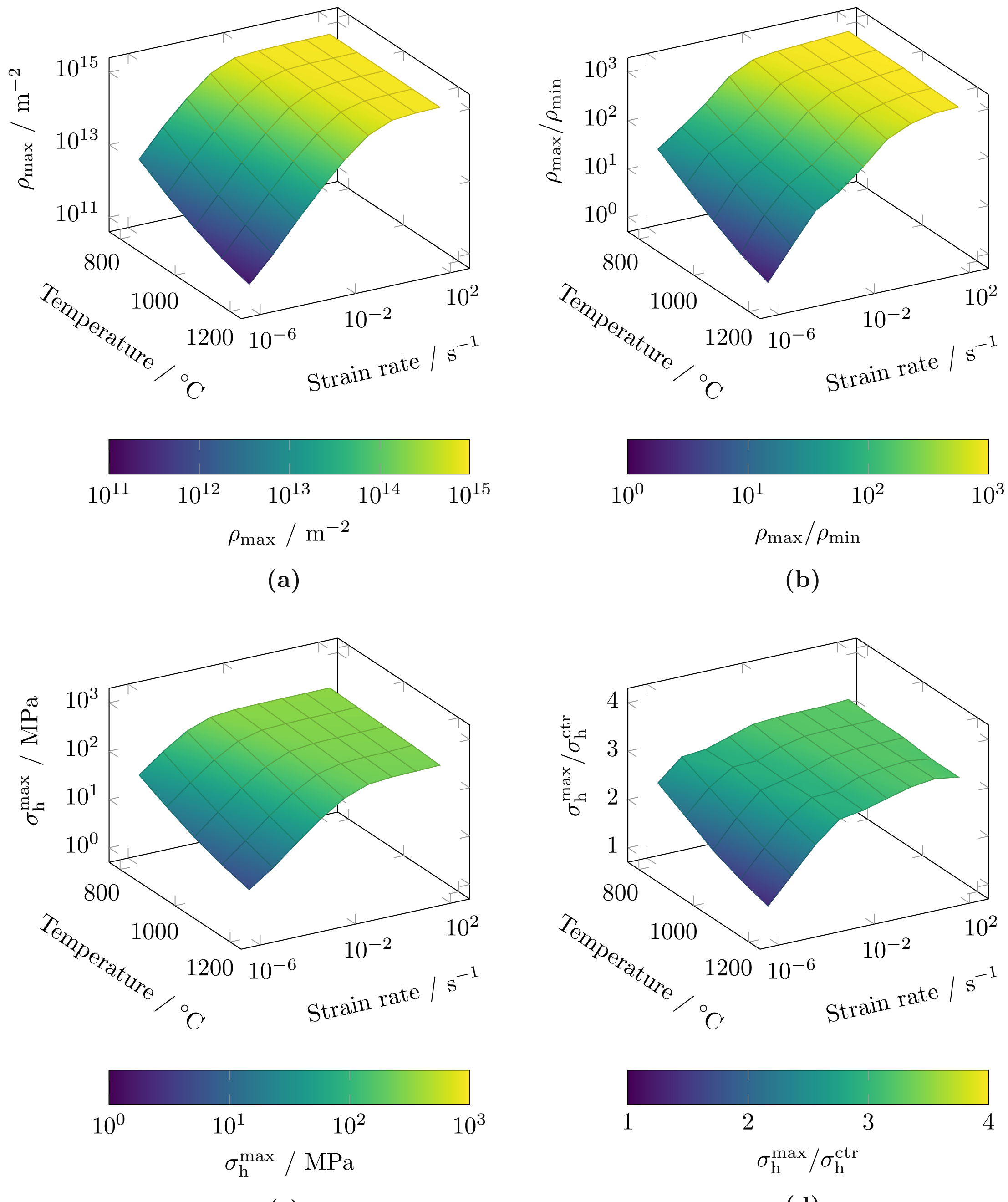

(a) **(b)** **(c)** **(d)**

Figure 6.14. Finite element analysis evaluation at 5 % external strain in the vertical direction and friction coefficient $\mu = 0.3$. (a) Maximum dislocation density ρ_max, (b) ratio of maximum and minimum dislocation density $\rho_\mathrm{max}/\rho_\mathrm{min}$, (c) maximum hydrostatic stress $\sigma_\mathrm{h}^\mathrm{max}$, (d) ratio of the hydrostatic stress maximum with the value of the grain center $\sigma_\mathrm{max}/\sigma_\mathrm{h}^\mathrm{ctr}$. See also figs. B.2 to B.5.

Die approbierte gedruckte Originalversion dieser Dissertation ist an der TU Wien Bibliothek verfügbar.
The approved original version of this doctoral thesis is available in print at TU Wien Bibliothek.
TU Bibliothek WIEN Your knowledge hub

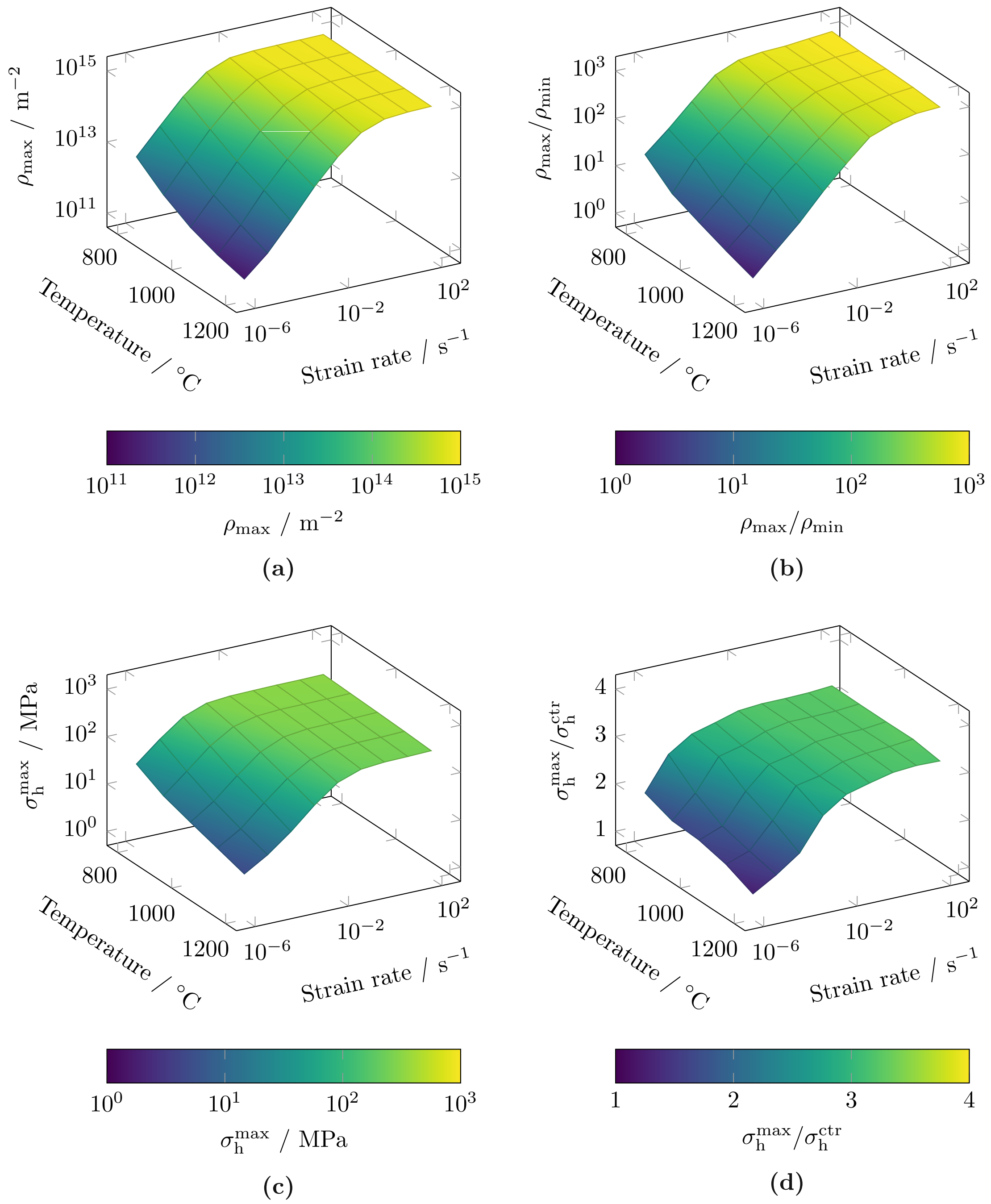

Figure 6.15. Finite element analysis evaluation at 5 % external strain in the vertical direction and friction coefficient $\mu = 1$. (a) Maximum dislocation density $\rho_{\max}$, (b) ratio of maximum and minimum dislocation density $\rho_{\max}/\rho_{\min}$, (c) maximum hydrostatic stress $\sigma_{\mathrm{h}}^{\max}$, (d) ratio of the hydrostatic stress maximum with the value of the grain center $\sigma_{\max}/\sigma_{\mathrm{h}}^{\mathrm{ctr}}$. See also figs. B.2 to B.5.

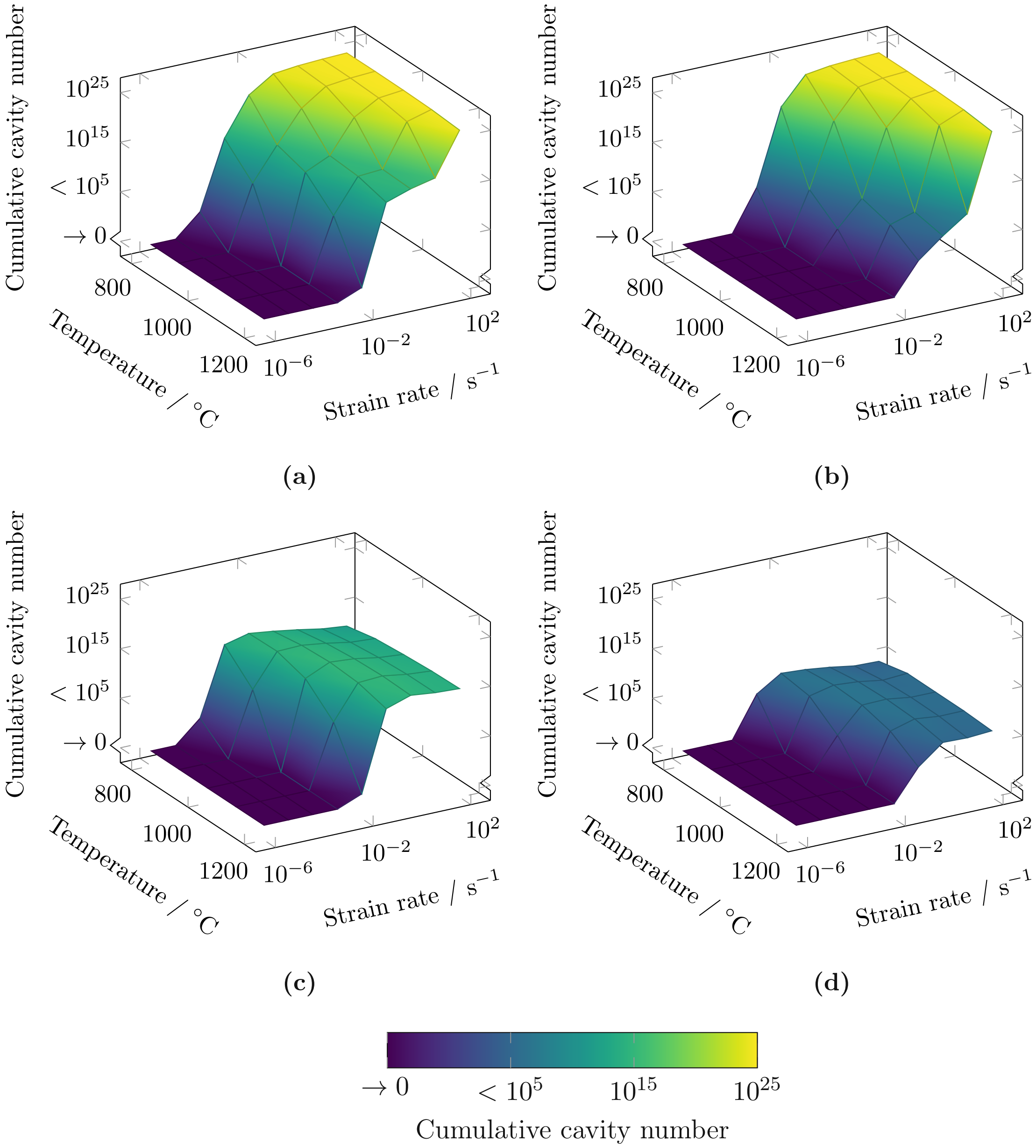

Figure 6.16. Cumulative number of cavities after applying 5 % external strain in the vertical direction, friction coefficient $\mu = 0$, grain boundary energy $\gamma_{\text{gb}} = 0.8\,\text{J}\,\text{m}^{-2}$, and a geometry factor reduced by two orders of magnitude. Vacancy concentration according to (a, b) Tang-Plumtree [16], and (c, d) Ungár [126] for cold rolling. Surface energy (a, c) $\gamma_{\text{s}} = 0.9\,\text{J}\,\text{m}^{-2}$, and (b, d) $\gamma_{\text{s}} = 1.02\,\text{J}\,\text{m}^{-2}$. See also figs. B.6 and B.7.

CHAPTER 7

Discussion

7.1 Experimental Results

Over the years, hot tensile testing has become the primary method for evaluating the susceptibility of steel to transverse cracking [21, 40]. Hot ductility curves (fig. 6.1d) are valuable for evaluating and comparing the temperature-dependent ductility behavior of different steel grades and cooling strategies. Some publications suggest an increased susceptibility to transverse cracking below a 40 % reduction-of-area value [19, 21, 25, 157]. Although Mintz [157] also mentions that the limit is highly dependent on the test conditions, the origin of the value is not feasible. Therefore, it is most likely empirical.

According to the 40 % limit and the hot ductility curves of the ⌀8 mm specimen, which we strained at $3 \times 10^{-4}\,\mathrm{s}^{-1}$, the strand should not suffer from transverse cracking even at a straightening temperature of 800 °C. The picture is different when we look at the results of the ⌀16 mm. The results (fig. 6.1d) suggest straightening above 900 °C. Testing with larger specimen geometries has a critical advantage: a larger nominal diameter. This simple fact is advantageous in several ways. First, the cross-sectional area is proportional to the square of the specimen diameter. Doubling the diameter results in four times the area and approximately four times as many grains, which is important because the grain size of this particular alloy is between 500 µm and 1000 µm after being subjected to our annealing cycle. Therefore, we suggest that a larger sample diameter will help to obtain more realistic results. Second, the DSI Gleeble 1500D testing machine has an 80 kN (Class 1) load cell. Accordingly, the measurement uncertainty is ±0.8 kN. The maximum recorded load for the ⌀8 mm specimens is between 2 kN and 5 kN over the temperature range of 800 °C to 1050 °C. Such low values suffer from significant measurement uncertainties; here, 40 % to 16 %. It is common practice not to fall below 10 % of the nominal value. Therefore, a load cell with a lower nominal force must be used to achieve higher accuracy. It is also recommended that the sample diameter be increased.s Tests with ⌀16 mm specimens resulted in maximum loads of 5 kN to 15 kN. This recommendation is most important when the force signals are of interest.

Our view on the 40 % limit is congruent with that of Jansto [158], who also criticizes it. In addition, Jansto reports crack-free castings of niobium-containing steels with area reduction values as low as 10 %. According to Jansto, strain energy is the better ductility criterion, especially for microalloyed grades*. Despite the promising announcement, the publication lacks information on correctly interpreting the obtained strain energy data.

Despite its limitations, reduction of area remains the most widely used metric for evaluating hot ductility in steel, primarily due to its simplicity. The application is attractive because one needs only a gauge and a fracture diameter to calculate the corresponding reduction of area value. The measurement can be made with a simple vernier caliper or extracted from X-ray computed tomography (XCT) data. Personal experience shows that the vernier caliper measurements are highly operator-dependent. Not all achieve results that are comparable to high-fidelity XCT data. Therefore, the quality of the measurements is highly dependent on the method and sometimes even on the operator. However, the future use of the hot tensile test needs to be reconsidered, as the three-point bending test has been shown to provide more realistic results [159]. According to Krobath et al. [159], this is manifested by surface cracking at low strains, reduced deformation-induced ferrite formation, and prevention of dynamic recrystallization.

This study focuses on a steel grade that is particularly susceptible to transverse cracking (table 4.1). In order to gain a comprehensive understanding of this particular alloy, we have subjected it to various cooling regimes and tested its response to different strain rates. Most of the experimental test results and conclusions are presented in Wiehoff's thesis [127]. In the present study, we further proposed that the standard test cooling regime ($1\,\mathrm{K\,s^{-1}}$) is not realistic for two reasons: (1) the geometry of a continuous caster cannot be changed, and (2) the casting speed varies only within narrow limits. Consequently, cooling to an arbitrary test temperature must be completed within an invariable time window of 800 s.

We expected the new cooling regime to produce different results, but it did not. The new cooling regime did not significantly affect the hot ductility curve (compare 8 mm, $1\,\mathrm{K\,s^{-1}}$, $3 \times 10^{-4}\,\mathrm{s^{-1}}$ with 8 mm, 800 s, $3 \times 10^{-4}\,\mathrm{s^{-1}}$ in fig. 6.1d). So, we needed to get a deeper insight into the material. A *great state-of-the-art tool* is a computer simulation that can perform thermokinetic analysis. To ensure the quality of our simulations, we compared our simulation results with data obtained from image analysis of carbon replica (C-replica) foils. The comparison of the two data (fig. 6.3) shows that (1) the simulated mean radius value is always within the standard deviation range of the image analysis data, (2) the standard deviation of the image analysis is higher than that predicted by MatCalc using a single-class model, and (3) the predicted precipitate radius agrees with the experimental data. Consequently, the simulation can calculate the strengthening contribution of the precipitates.

Niobium carbonitrides (Nb(C,N)) are known to reduce the hot ductility of steel. The loss of ductility is attributed to precipitation hardening of the matrix, resulting in stress concentrations along the austenite grain boundary [18, 20, 33, 160–164]. Regarding the strengthening effect, reference [165] states that for each 0.01 wt% of niobium, the strength increases by 35 MPa to 40 MPa. The investigated steel grade contains 180 ppm of niobium (table 4.1). Therefore, the niobium content alone

---

[*] Evaluation of strain energy in this work, see fig. 6.1c

should increase the strength between 63 MPa and 72 MPa. These values are probably at room temperature, as no temperature is given in the above reference. Accordingly, the increase in strength would result from a fine ferrite-pearlite grain structure developing in the presence of many small niobium precipitates. MatCalc can help identify the actual influence of the various strength contributors. We evaluated the strengthening contribution using a coarse-grained annealed steel that we cooled from the solid solution state at 1320 °C to the desired test temperature of 800 °C in 800 s. The sample is then strained at $3 \times 10^{-4}\,\mathrm{s}^{-1}$ follows. The simulation shows that the precipitates contribute only about 15 MPa to the total yield stress.

7.2 Calculations

Raj-Ashby and Steady-State Nucleation Model

As Riedel [1] states, the nucleation stress strongly depends on the exponential part. This statement also applies to the analysis of austenite at homologous temperatures between 0.6 and 1 (fig. 6.4).

Calculation of the stress concentration based on the steady-state nucleation rate equation (eq. (3.41)) indicates that vacancy condensation requires applied stresses between 2.7 GPa and 6.5 GPa (fig. 6.5) for the assumed boundary conditions. The stress required for pure vacancy condensation, i.e., not assisted by any other mechanism, is about two orders of magnitude higher than our recorded stress values (fig. B.1). This is also consistent with Riedel's [1] analysis, which indicates that void nucleation by pure vacancy condensation is impossible in creep tests at typical applied stresses (10 MPa to 100 MPa).

The steady-state nucleation rate equation (eq. (3.41)) was further used to investigate the incubation and diffusive relaxation times. Void incubation is possible at stresses above 100 MPa. However, as shown in section 6.2, the diffusive relaxation times are several orders of magnitude smaller. For this reason, vacancy condensation is unlikely to occur by the proposed mechanism in the steady-state nucleation model. Thus, Riedel's [1] findings for ferrite are likewise valid for austenite.

Becker-Döring Nucleation Model and Unified Thermodynamic Cavity Nucleation

The side-by-side comparison of the single and multi-diffusion path results indicates that grain boundary diffusion is dominant. Thus, lattice diffusion is of secondary importance (fig. 6.8). It is also clear that applying a more complex equation does not necessarily provide additional information (eqs. (3.36) and (3.37)).

Despite the above facts, small void tip angles significantly promote nucleation (fig. 6.8). A prime candidate for such a nucleation-friendly environment is the triple junction [1, 166]. Of course, the correct estimation of the surface energy γ_s is crucial because the change in free energy raises it to the third power (eq. (3.25)). Additionally, an increased nucleation rate is feasible within a specific range of radii if we respect the generalized shape factor of Svoboda and Sklenička [7]. The difference in the volumetric shape factor of Raj and Ashby [4] comes from the rejection of an

Die approbierte gedruckte Originalversion dieser Dissertation ist an der TU Wien Bibliothek verfügbar.
The approved original version of this doctoral thesis is available in print at TU Wien Bibliothek.
TU Bibliothek WIEN Your knowledge hub

infinite inclusion size. The difference is about two orders of magnitude in the best case.

Finally, it should be noted that a nucleation rate of $J = 1 \times 10^{10}\,\mathrm{s}^{-1}\,\mathrm{m}^{-2}$ corresponds to $J = 36\,\mathrm{h}^{-1}\,\mathrm{mm}^{-2}$. Consequently, only void tip angles ψ less than 50° give promising results in the present evaluation.

Tang-Plumtree Excess Vacancy Model

The excess void model of Tang and Plumtree [16] complements the classical nucleation theory models of Raj-Ashby and Gleixner et al. [4, 90]. It explains how the applied stress is locally amplified by microstructural states that provide the additional driving force for void nucleation (eq. (3.46)).

Adequate stress concentration contributions from excess vacancies at elevated temperatures and above require low dislocation densities and high strain rates. (fig. 6.9). This finding is not surprising when we look at eqs. (3.47) to (3.49), from which we learn that the excess vacancy concentration gains are proportional to the strain rate and the inverse dislocation density, $c_{\mathrm{ex}} \propto \dot{\varepsilon}_{\mathrm{loc}}/\left(4\varrho\right)$. Consequently, strain hardening makes it increasingly difficult to gain additional driving force in the strengthened regions of the material.

Besides the mean diffusion distance L and the local strain rate $\dot{\varepsilon}_{\mathrm{loc}}$, a proper estimation of the vacancy concentration is crucial for the excess vacancy model. Tang and Plumtree [16] implemented a linear, plastic strain-dependent relationship for the evolution of the vacancy concentration (eq. (3.51)). The plastic deformation approach is simple, but it is not time-dependent like the mean diffusion distance. This deficiency is due to the extended Kocks-Mecking dislocation evolution (eq. (3.16)) and its combination with the vacancy concentration equations of Ungár et al. [126] (eqs. (3.52) and (3.53)). However, the latter equation has two other minor drawbacks. First, the vacancy concentration is a function of the deformation mode, and second, it does not represent a localized vacancy concentration, such as that near the grain boundary, which can reach values up to 1×10^{-3} [126]. Despite these drawbacks, the advantages of the dislocation-based approach still prevail, as seen at the end of section 7.3 Computation with Representative Area Model.

7.3 Computer Simulations

Cooling Rate Sensitivity

Evaluation of the cooling rate variation showed that only rapid cooling rates ($1 \times 10^{2}\,\mathrm{K\,s}^{-1}$) significantly influence nucleation kinetics. Therefore, it can be concluded that typical conventional strand-casting cooling rates ($< 1\,\mathrm{K\,s}^{-1}$) do not influence nucleation kinetics. However, the selection of an appropriate cooling rate is still crucial. Computational analyses show that a reduced cooling rate is beneficial in terms of residual stresses [167]. However, the cooling rate is not an arbitrary variable. Too much cooling can lead to thermal stresses; too little cooling results in extensive reheating, which expands the strand surface. In the worst case, the latter will initiate hot tear cracks at the solidification front [168].

Finite Element Analysis

Single-Element Test

The simulation approach of a MatCalc precipitation kinetics simulation differs from that of an Ansys Mechanical structural analysis. MatCalc is not designed to perform simulations of discrete structures; it is a material calculation tool. Because MatCalc does not use structural information, it can calculate the precipitation kinetics simulations on a single representative volume element (RVE) using the Svoboda-Fischer-Fratzl-Kozeschnik (SFFK) model, a mean-field approach for complex systems [155, 169]. This approach creates a single homogeneous matrix that contains all the properties of the entire model. Therefore, temperature and pressure are homogeneous throughout the RVE [169]. The same is true for the strain rate tensor.

In contrast, Ansys Mechanical is a finite element software for structural analysis. The central components of such simulations are the finite elements, which are available in different shapes. Apart from the shape, the elements can be of linear or nonlinear character. The main features of the elements are nodes and integration points, of which a quadrilateral linear plane element has four. Consider a statically determinate single element with an applied boundary condition that causes a deformation, such as a displacement of nodes (fig. 5.3). During the deformation, the integration points do not displace uniformly because their displacement depends on the boundary conditions and material laws; accordingly, the strain rate is distributed unevenly. Therefore, the *constant* strain rate and the *initial* strain rate course must be different (fig. 6.12).

Computation with Representative Area Model

In section 3.2 Plasticity, we outlined that today's understanding of metal plasticity is based on dislocations, so it is unsurprising that dislocations became the backbone of our computational model (section 5.4 Program Specific Features). As we recall from section 3.2 Dislocation Density Evolution Models, we have implemented dislocation evolution according to the extended Kocks-Mecking model (eq. (3.16)). Therefore, all dislocation density plots (figs. 6.13a, 6.14a, and 6.15a) bear the model's signature mentioned above. A favorable environment for dislocation generation exists mainly at high strain rates and low temperatures. This trend is also visible in the hydrostatic stress plots (figs. 6.13c, 6.13d, 6.14c, 6.14d, 6.15c, and 6.15d), which is not surprising since we can only achieve high hydrostatic stresses in regions of increased yield stress. A significant portion of the yield stress is due to strain hardening. In our computer simulation, we calculate the strain hardening contribution according to the Taylor equation (eq. (3.15)), which is a direct descendant of the square root of the dislocation density. Finally, we look at the stress enhancement (figs. 6.13d, 6.14d, and 6.15d), which helps us identify temperatures and strain rates with low and high stress-distribution uniformity. The plots show that the stress concentration does not change significantly within the evaluated range for frictionless contacts but does change when the grain boundary is no longer perfectly smooth. Since the material model of this study was the first attempt to program a user material, we tried to keep the contact definition simple and, therefore, modeled it as a flat interface with Coulomb friction. Sliding of the contact pair is, therefore, only allowed

Die approbierte gedruckte Originalversion dieser Dissertation ist an der TU Wien Bibliothek verfügbar.
The approved original version of this doctoral thesis is available in print at TU Wien Bibliothek.
TU Bibliothek WIEN Your knowledge hub

when the shear stress exceeds a certain threshold, which is a function of the friction coefficient, the contact pressure, and the cohesion sliding resistance [170]. Therefore, the expanding region of a stress ratio close to unity results from the friction coefficient, as it becomes increasingly difficult for the shear stress to overcome the sliding barrier.

At this point, it is worth remembering that a grain boundary is a surface, not a body of finite thickness, so we need to model the grain boundary as an interface. The only feasible solution that fit the scope of this project was the Coulomb friction described above. However, this approach ignores the general description of the grain boundary, which has a nonplanar shape and can be described by microscopic shear viscosity using the Stokes-Einstein equation [171]. Such behavior needs to be implemented in a future extension of the model through a user-programmable feature (UPF). Candidates for this UPF are either a friction law[†] or a contact interaction[‡] [170].

Finally, we return to the nucleation of cavities and compare the Tang-Plumtree model [16] and and the adapted version[§] using information from Ungár et al. [126]. As already noted in section 7.2 Tang-Plumtree Excess Vacancy Model, the Tang-Plumtree excess vacancy approach (figs. 6.16a and 6.16b) implies that the hydrostatic stress itself must be the dominant driving force since the conditions for an additional chemical driving force are unfavorable in the regions of highest cumulative nucleation achieved, i.e., at low temperatures and high dislocation densities (or low average mean diffusion distances) (eqs. (3.47) to (3.50)). The Tang-Plumtree model relies on the dislocation density, meaning maintaining a vacancy concentration requires a certain amount of continuous plastic deformation. Therefore, the nucleation of cavities relies on at least two prerequisites: (1) Overcoming the nucleation barrier and (2) maintaining a certain amount of plastic deformation to maintain the vacancy concentration level. Therefore, abundant cavity nucleation occurs only at slightly elevated temperatures and intermediate strain rates, where the cavities have sufficient time to nucleate. Accordingly, intermediate strain rates are more detrimental than extremely low or high rates. While the former makes it difficult to overcome the nucleation barrier, the latter does not provide enough time for abundant cavity nucleation (figs. 6.16c and 6.16d). Comparing the left and right figures reveals another critical parameter, the surface energy. For example, the surface energy of SAE 304 stainless steel at 1060 °C is $2.19\,\mathrm{J\,m^{-2}}$ [172], while the surface energy of aluminum oxide (Al_2O_3) at a comparable temperature of 1000 °C is only $0.9\,\mathrm{J\,m^{-2}}$ [173].

Surface energy has a strong influence on the ability to nucleate. An increase in surface energy of just over 10 % can reduce the number of nucleated voids by several orders of magnitude (figs. 6.16c and 6.16d). However, it does not necessarily take a different species to have a drastic effect. Bulatov et al. [174] have shown in their analysis of fcc metals that the grain boundary energy strongly depends on the orientation of the grains. Therefore, the correct estimation of surface and grain boundary energies is critical.

[†] `userfric.f`

[‡] `userinter.f`

[§] With respect to temperature and strain rate.

CHAPTER 8

Summary and Conclusions

Experimental studies have shown that hot tensile specimens with larger gauge diameters fail more brittle. Changing the cooling rate did not significantly affect the fracture characteristics. Moreover, our computer simulations indicate that cooling rate variations within a production-relevant range do not significantly alter the precipitation state.

Fracture strains from hot tensile tests that closely resemble the straightening process of continuous casting either require further adaptation of the test itself or are not feasible. In the former case, Wiehoff's experiments [127] show that switching from cylindrical to flat specimens may be part of the solution. However, three-point bending tests have obtained more promising results [159]. At this time, it remains unclear whether a DSI Gleeble 1500D can be modified for bending tests.

Casting the Kreyca-Kozeschnik state parameter-based material model [83] into a user-programmable feature of an Ansys finite element analysis allowed observation of the spatial distribution and time-dependent evolution of microstructural features such as dislocation density. Although a simple Coulomb friction model is applied to the grain boundary, the model can only represent creep behavior. Mimicking grain boundary sliding requires the development of a separate user subroutine.

The implemented nucleation model of Gleixner et al. [90] with adjustments according to Svoboda and Sklenička, in combination with the excess vacancy model of Tang and Plumtree [16], showed a monotonically increasing nucleation rate at low temperatures and high strain rates. Implementing the information from Ungár et al. [126] allowed the formulation of a state parameter-based excess vacancy model. Computer simulations with this model show that most cavities accumulate at intermediate temperatures and strain rates in the experimental range, with surface and grain boundary energies significantly influencing this behavior.

Consequently, stress concentration cannot be the sole mechanism leading to cavitation because it is three to four orders of magnitude below the required level; sufficient driving force levels require at least one additional order of magnitude. Nevertheless, cavitation can occur at moderate stress concentration levels but only in conjunction with excess vacancies. The role of grain boundary sliding needs to be further investigated.

References

[1] H. Riedel, Fracture at High Temperatures, Materials research and engineering, Springer Berlin Heidelberg, Berlin, Heidelberg, 1987. `doi:10.1007/978-3-642-82961-1`.

[2] H. Riedel, Cavity nucleation at particles on sliding grain boundaries. A shear crack model for grain boundary sliding in creeping polycrystals, Acta Metallurgica 32 (3) (1984) 313–321. `doi:10.1016/0001-6160(84)90104-4`.

[3] J. Greenwood, D. Miller, J. Suiter, Intergranular cavitation in stressed metals, Acta Metallurgica 2 (2) (1954) 250–258. `doi:10.1016/0001-6160(54)90166-2`.

[4] R. Raj, M. Ashby, Intergranular fracture at elevated temperature, Acta Metallurgica 23 (6) (1975) 653–666. `doi:10.1016/0001-6160(75)90047-4`.

[5] R. Raj, Nucleation of cavities at second phase particles in grain boundaries, Acta Metallurgica 26 (6) (1978) 995–1006. `doi:10.1016/0001-6160(78)90050-0`.

[6] J. Svoboda, I. Turek, V. Sklenička, Unified thermodynamic treatment of cavity nucleation and growth in high temperature creep, Acta Metallurgica et Materialia 38 (4) (1990) 573–580. `doi:10.1016/0956-7151(90)90211-X`.

[7] J. Svoboda, V. Sklenička, Thermal cavity nucleation at intergranular inclusions in high temperature creep, Acta Metallurgica et Materialia 38 (6) (1990) 1141–1149. `doi:10.1016/0956-7151(90)90187-L`.

[8] M. Ahmadi, B. Sonderegger, S. Yadav, M. Poletti, Modelling and simulation of diffusion driven pore formation in martensitic steels during creep, Materials Science and Engineering A 712 (December 2017) (2018) 466–477. `doi:10.1016/j.msea.2017.12.010`.

[9] M. Volmer, A. Weber, Keimbildung in übersättigten Gebilden, Zeitschrift für Physikalische Chemie 119U (1). `doi:10.1515/zpch-1926-11927`.

[10] L. Farkas, Keimbildungsgeschwindigkeit in übersättigten Dämpfen, Zeitschrift für Physikalische Chemie 125U (1). `doi:10.1515/zpch-1927-12513`.

[11] J. Gibbs, The Collected Works of J. Willard Gibbs. Volume I. Thermodynamics, Longmans, Green & Co., New York, London, Toronto, 1928.

[12] R. Kaischew, I. Stranski, Zur kinetischen Ableitung der Keimbildungsgeschwindigkeit, Z. Phys. Chem. B 26 (1934) 317–326.

[13] R. Becker, W. Döring, Kinetische Behandlung der Keimbildung in übersättigten Dämpfen, Annalen der Physik 416 (8) (1935) 719–752. `doi:10.1002/andp.19354160806`.

[14] J. Frenkel, A general theory of heterophase fluctuations and pretransition phenomena, The Journal of Chemical Physics 7 (7) (1939) 538–547. `doi:10.1063/1.1750484`.

[15] Y. B. Zeldovich, On the Theory of New Phase Formation: Cavitation, Acta Physicochimica U.R.S.S. 12 (1) (1943) 1–22.

[16] N. Tang, A. Plumtree, Cavity nucleation in creep, Scripta Metallurgica 18 (10) (1984) 1045–1049. `doi:10.1016/0036-9748(84)90176-5`.

[17] M. Militzer, W. P. Sun, J. J. Jonas, Modelling the effect of deformation-induced vacancies on segregation and precipitation, Acta Metallurgica et Materialia 42 (1) (1994) 133–141. `doi:10.1016/0956-7151(94)90056-6`.

[18] J. K. Brimacombe, K. Sorimachi, Crack formation in the continuous casting of steel, Metallurgical Transactions B 8 (2) (1977) 489–505. `doi:10.1007/BF02696937`.

[19] B. Mintz, S. Yue, J. J. Jonas, Hot ductility of steels and its relationship to the problem of transverse cracking during continuous casting, International Materials Reviews 36 (1) (1991) 187–220. `doi:10.1179/imr.1991.36.1.187`.

[20] B. Thomas, J. Brimacombe, I. Samarasekera, The Formation of Panel Cracks in Steel Ingots: A State-of-the-Art Review, I. Hot Ductility of Steel, Transactions of the Iron and Steel Society 7 (1986) 7–20. Available from: `https://ccc.illinois.edu/PDF%20Files/Publications/86_Trans_ISS_Formation_Panel_Cracks_Steel_Ductility_ocr.pdf` [accessed 2019-08-23].

[21] B. Mintz, D. N. Crowther, Hot ductility of steels and its relationship to the problem of transverse cracking in continuous casting, International Materials Reviews 55 (3) (2010) 168–196. `doi:10.1179/095066009X12572530170624`.

[22] C. Zhang, M. Bellet, M. Bobadilla, H. Shen, B. Liu, A coupled electrical-thermal-mechanical modeling of gleeble tensile tests for ultra-high-strength (UHS) steel at a high temperature, Metallurgical and Materials Transactions A: Physical Metallurgy and Materials Science 41 (9) (2010) 2304–2317. `doi:10.1007/s11661-010-0310-7`.

[23] P. Presoly, R. Pierer, C. Bernhard, Identification of defect prone peritectic steel grades by analyzing high-temperature phase transformations, Metallurgical and Materials Transactions A: Physical Metallurgy and Materials Science 44 (12) (2013) 5377–5388. `doi:10.1007/s11661-013-1671-5`.

[24] B. G. Thomas, Review on Modeling and Simulation of Continuous Casting, steel research international 89 (1) (2018) 1700312. `doi:10.1002/srin.201700312`.

[25] B. Mintz, The Influence of Composition on the Hot Ductility of Steels and to the Problem of Transverse Cracking., ISIJ International 39 (9) (1999) 833–855. `doi:10.2355/isijinternational.39.833`.

[26] T. N. Baker, Microalloyed steels, Ironmaking & Steelmaking 43 (4) (2016) 264–307. `doi:10.1179/1743281215Y.0000000063`.

[27] C. Ouchi, K. Matsumoto, Hot ductility in Nb-bearing high-strength low-alloy steels, Trans. Iron Steel Inst. Jpn 22 (181) (1982) 181–189.

[28] F. G. Wilson, T. Gladman, Aluminium nitride in steel, International Materials Reviews 33 (1) (1988) 221–286. `doi:10.1179/imr.1988.33.1.221`.

[29] E. O. Hall, The Deformation and Ageing of Mild Steel: III Discussion of Results, Proceedings of the Physical Society. Section B 64 (9) (1951) 747–753. `doi:10.1088/0370-1301/64/9/303`.

[30] N. J. Petch, The Cleavage Strength of Polycrystals, Journal of The Iron and Steel Institute 174 (1) (1953) 25–28.

[31] N. Hansen, Hall-Petch relation and boundary strengthening, Scripta Materialia 51 (8) (2004) 801–806. `doi:10.1016/j.scriptamat.2004.06.002`.

[32] U. F. Kocks, H. Mecking, Physics and phenomenology of strain hardening: The FCC case, Progress in Materials Science 48 (3) (2003) 171–273. `doi:10.1016/S0079-6425(02)00003-8`.

[33] Y. Maehara, Y. Ohmori, The precipitation of AlN and NbC and the hot ductility of low carbon steels, Materials Science and Engineering 62 (1) (1984) 109–119. `doi:10.1016/0025-5416(84)90272-6`.

[34] J. S. Park, Y. S. Ha, S. J. Lee, Y. K. Lee, Dissolution and precipitation kinetics of Nb(C,N) in austenite of a low-carbon Nb-microalloyed steel, Metallurgical and Materials Transactions A: Physical Metallurgy and Materials Science 40 (3) (2009) 560–568. `doi:10.1007/s11661-008-9758-0`.

[35] B. Dutta, C. M. Sellars, Effect of composition and process variables on Nb(C, N) precipitation in niobium microalloyed austenite, Materials Science and Technology 3 (3) (1987) 197–206. `doi:10.1179/mst.1987.3.3.197`.

[36] E. V. Pereloma, B. R. Crawford, P. D. Hodgson, Strain-induced precipitation behaviour in hot rolled strip steel, Materials Science and Engineering A 299 (1-2) (2001) 27–37. `doi:10.1016/S0921-5093(00)01423-4`.

[37] S. C. Hong, S. H. Lim, H. S. Hong, K. J. Lee, D. H. Shin, K. S. Lee, Effects of Nb on strain induced ferrite transformation in C-Mn steel, Materials Science and Engineering A 355 (1-2) (2003) 241–248. `doi:10.1016/S0921-5093(03)00071-6`.

[38] E. Kozeschnik, Modeling Solid-State Precipitation, Momentum Press, 2012. `doi:10.5643/9781606500644`.

[39] H. G. Suzuki, S. Nishimura, S. Yamaguchi, Characteristics of Hot Ductility in Steels Subjected to the Melting and Solidification, Transactions of the Iron and Steel Institute of Japan 22 (1) (1982) 48–56. `doi:10.2355/isijinternational1966.22.48`.

[40] K. M. Banks, A. S. Tuling, B. Mintz, Improved Simulation of Continuous Casting to Predict Transverse Corner Cracking in Microalloyed Steels, International Journal of Metallurgical Engineering 2 (2) (2013) 188–197. `doi:10.5923/j.ijmee.20130202.10`.

[41] D. Djuric, Heißzugprüfmaschine BETA 250-5, conference date: 05-05-2011 (Mai 2011). Available from: `https://pure.tugraz.at/ws/portalfiles/portal/1650067/Poster%2520BETA_Dragan%2520Djuric%2520v2.pdf` [accessed 2019-04-16].

[42] D. Djuric, C. Höller, M. Oberroither, B. Sonderegger, C. Sommitsch, In-situ-Aufschmelz-Methode zur Bestimmung der Hochtemperatureigenschaften von Stählen, Materials Testing 54 (2) (2012) 75–79. `doi:10.3139/120.110298`.

[43] D. Djuric, O. Caliskanoglu, D. Leidinger, S. Ilie, C. Sommitsch, Untersuchung des zweiten Duktilitätsminimums mikrolegierter Stähle mit einer neu entwickelten Heißzugprüfung, BHM Berg- und Hüttenmännische Monatshefte 157 (8-9) (2012) 296–300. `doi:10.1007/s00501-012-0026-7`.

[44] D. D. S. Inc., The Gleeble Induction Heating System (IHS) provides an alternative heating method to increase testing flexibility (2018). Available from: `http://dsi.gleeble.com/Induction` [accessed 2019-08-23].

[45] Normenausschuss Materialprüfung (NMP) im DIN, DIN EN ISO 6892-2: Metallische Werkstoffe - Zugversuch - Teil 2: Prüfverfahren bei erhöhter Temperatur (2011).

[46] U. Glatzel, High Temperature Tensile Testing. Available from: `http://www.metalle.uni-bayreuth.de/de/download/teaching_downloads/high_temperature_tensile_testing.pdf` [accessed 2019-01-22].

[47] M. Abspoel, B. M. Neelis, P. van Liempt, Constitutive behaviour under hot stamping conditions, Journal of Materials Processing Technology 228 (2016) 34–42. `doi:10.1016/j.jmatprotec.2015.05.007`.

[48] B. Mintz, R. Abu-Shosha, M. Shaker, Influence of deformation induced ferrite, grain boundary sliding, and dynamic recrystallisation on hot ductility of $0 \cdot 1 - 0 \cdot 75\,\%$ C steels, Materials Science and Technology 9 (10) (1993) 907–914. `doi:10.1179/mst.1993.9.10.907`.

[49] B. Mintz, J. J. Jonas, Influence of strain rate on production of deformation induced ferrite and hot ductility of steels, Materials Science and Technology 10 (August) (1994) 721–727. `doi:10.1179/mst.1994.10.8.721`.

[50] Y. Maehara, K. Yasumoto, H. Tomono, T. Nagamichi, Y. Ohmori, Surface cracking mechanism of continuously cast low carbon low alloy steel slabs, Materials Science and Technology 6 (9) (1990) 793–806. `doi:10.1179/026708390790193664`.

[51] S. H. Song, Z. X. Yuan, J. Jia, D. D. Shen, a. M. Guo, The role of tin in the hot-ductility deterioration of a low-carbon steel, Metallurgical and Materials Transactions A 34 (8) (2003) 1611–1616. `doi:10.1007/s11661-003-0306-7`.

[52] W. T. Lankford, Some considerations of strength and ductility in the continuous-casting process (1972). `doi:10.1007/BF02643017`.

[53] SMS CONCAST AG, Continuous Casting - The world's leading technology for long products (2014). Available from: `http://www.sms-concast.ch/fileadmin/user_upload/concast/pdf/ContinuousCasting_en_GzD.pdf` [accessed 2018-11-07].

[54] Primetals Technologies Ltd., Continuous slab caster from Primetals Technologies goes on stream at CSP in Brazil (2016). Available from: `http://www.primetals.co.jp/press/pdf/20160816.pdf` [accessed 2018-11-07].

[55] Primetals Technologies Ltd., Primetals Technologies to upgrade continuous slab caster for China Steel Corporation in Kaohsiung, Taiwan (2017). Available from: `http://www.primetals.co.jp/press/pdf/20170810.pdf` [accessed 2018-11-07].

[56] M. Hanao, M. Kawamoto, A. Yamanaka, Growth of Solidified Shell Just below the Meniscus in Continuous Casting Mold, ISIJ International 49 (3) (2009) 365–374. `doi:10.2355/isijinternational.49.365`.

[57] F. Pascon, A. M. Habraken, Finite element study of the effect of some local defects on the risk of transverse cracking in continuous casting of steel slabs, Computer Methods in Applied Mechanics and Engineering 196 (21-24) (2007) 2285–2299. `doi:10.1016/j.cma.2006.07.017`.

[58] E. Orowan, Zur Kristallplastizität. III, Zeitschrift für Physik 89 (9-10) (1934) 634–659. `doi:10.1007/BF01341480`.

[59] M. Polanyi, Über eine Art Gitterstörung, die einen Kristall plastisch machen könnte, Zeitschrift für Physik 89 (9) (1934) 660–664. `doi:10.1007/BF01341481`.

[60] G. I. Taylor, The Mechanism of Plastic Deformation of Crystals. Part I. Theoretical, Proceedings of the Royal Society A: Mathematical, Physical and Engineering Sciences 145 (855) (1934) 362–387. `doi:10.1098/rspa.1934.0106`.

[61] A. Argon, Strengthening Mechanisms in Crystal Plasticity, Oxford University Press, 2007. `doi:10.1093/acprof:oso/9780198516002.001.0001`.

[62] U. Messerschmidt, M. Bartsch, Generation of dislocations during plastic deformation, Materials Chemistry and Physics 81 (2) (2003) 518–523. doi:10.1016/S0254-0584(03)00064-6.

[63] H. J. Frost, M. F. Ashby, Deformation-Mechanism Maps - The Plasticity and Creep of Metals and Ceramics, 1st Edition, Pergamon Press, Oxford [u.a.], 1982. Available from: http://engineering.dartmouth.edu/defmech/ [accessed 2019-08-08].

[64] P. E. J. Rivera-Díaz-del Castillo, M. Huang, Dislocation annihilation in plastic deformation: I. Multiscale irreversible thermodynamics, Acta Materialia 60 (6) (2012) 2606–2614. doi:10.1016/j.actamat.2012.01.027.

[65] J. Weertman, Width of a moving edge dislocation calculated with the Nabarro force law, Philosophical Magazine 18 (155) (1968) 959–964. doi:10.1080/14786436808227518.

[66] U. Essmann, H. Mughrabi, Annihilation of dislocations during tensile and cyclic deformation and limits of dislocation densities, Philosophical Magazine A 40 (6) (1979) 731–756. doi:10.1080/01418617908234871.

[67] W. Püschl, Models for dislocation cross-slip in close-packed crystal structures: a critical review, Progress in Materials Science 47 (4) (2002) 415–461. doi:10.1016/S0079-6425(01)00003-2.

[68] A. Argon, W. Moffatt, Climb of extended edge dislocations, Acta Metallurgica 29 (2) (1981) 293–299. doi:10.1016/0001-6160(81)90156-5.

[69] T. Watanabe, Grain boundary design and control for high temperature materials, Materials Science and Engineering A 166 (1-2) (1993) 11–28. doi:10.1016/0921-5093(93)90306-Y.

[70] S. R. Chen, U. Kocks, High-temperature plasticity in copper polycrystals, in: A. D. Freed, K. P. Walker (Eds.), High Temperature Constitutive Modeling: Theory and Applications; Proceedings of the Symposium, 112th ASME Winter Annual Meeting, Atlanta, GA, Dec. 1-6, 1991 American Society of Mechanical Engineers, Vol. 26, American Society of Mechanical Engineers (ASME), New York, 1991, pp. 1–12. Available from: https://www.osti.gov/servlets/purl/5238950.

[71] E. Orowan, Problems of plastic gliding, Proceedings of the Physical Society 52 (1) (1940) 8–22. doi:10.1088/0959-5309/52/1/303.

[72] D. Kuhlmann, On the Theory of Plastic Deformation, Proc. Phys. Soc. A 64 (1951) 140–155.

[73] M. E. Kassner, Fundamentals of Creep in Metals and Alloys, 3rd Edition, Elsevier, Walthama, USA; Oxford, UK, 2015. doi:10.1016/C2012-0-06071-1.

[74] M. Kassner, M.-T. Pérez-Prado, Five-power-law creep in single phase metals and alloys, Progress in Materials Science 45 (1) (2000) 1–102. doi:10.1016/S0079-6425(99)00006-7.

[75] E. Nes, Modelling of work hardening and stress saturation in FCC metals, Progress in Materials Science 41 (3) (1997) 129–193. doi:10.1016/S0079-6425(97)00032-7.

[76] T. Sakai, A. Belyakov, R. Kaibyshev, H. Miura, J. J. Jonas, Dynamic and post-dynamic recrystallization under hot, cold and severe plastic deformation conditions, Progress in Materials Science 60 (1) (2014) 130–207. doi:10.1016/j.pmatsci.2013.09.002.

[77] R. Doherty, D. Hughes, F. Humphreys, J. Jonas, D. Juul Jensen, M. Kassner, W. King, T. McNelley, H. McQueen, A. Rollett, Current issues in recrystallization: A review, Materials Today 1 (2) (1998) 219–274. doi:10.1016/S0921-5093(97)00424-3.

[78] J. Hines, K. Vecchio, Recrystallization kinetics within adiabatic shear bands, Acta Materialia 45 (2) (1997) 635–649. doi:10.1016/S1359-6454(96)00193-0.

[79] M.-T. Perez-Prado, M. Kassner, Diffusional Creep, in: Fundamentals of Creep in Metals and Alloys, 3rd Edition, Elsevier, 2015, Ch. 3, pp. 103–108. doi:10.1016/B978-0-08-099427-7.00003-7.

[80] P. Ludwik, Elemente der Technologischen Mechanik, Springer Berlin Heidelberg, Berlin, Heidelberg, 1909. doi:10.1007/978-3-662-40293-1.

[81] J. H. Hollomon, Tensile Deformation, Transactions of the American Institute of Mining and Metallurgical Engineers 162 (1945) 268–290.

[82] A. Kundu, D. P. Field, Geometrically Necessary Dislocation Density Evolution in Interstitial Free Steel at Small Plastic Strains, Metallurgical and Materials Transactions A: Physical Metallurgy and Materials Science 49 (8) (2018) 3274–3282. doi:10.1007/s11661-018-4693-1.

[83] J. Kreyca, E. Kozeschnik, State parameter-based constitutive modelling of stress strain curves in Al-Mg solid solutions, International Journal of Plasticity 103 (2018) 67–80. doi:10.1016/j.ijplas.2018.01.001.

[84] P. S. Follansbee, U. F. Kocks, A constitutive description of the deformation of copper based on the use of the mechanical treshold stress as an internal state variable, Acta Metall 36 (1) (1988) 81–93. doi:10.1016/0001-6160(88)90030-2.

[85] D. Goto, J. Bingert, W. Reed, R. Garrett Jr, Anisotropy-corrected MTS constitutive strength modeling in HY-100 steel, Scripta Materialia 42 (12) (2000) 1125–1131. doi:10.1016/S1359-6462(00)00347-X.

[86] B. Banerjee, The Mechanical Threshold Stress model for various tempers of AISI 4340 steel, International Journal of Solids and Structures 44 (3-4) (2007) 834–859. doi:10.1016/j.ijsolstr.2006.05.022.

[87] K. M. Davoudi, J. J. Vlassak, Dislocation evolution during plastic deformation: Equations vs. discrete dislocation dynamics study, Journal of Applied Physics 123 (8) (2018) 085302. `doi:10.1063/1.5013213`.

[88] U. F. Kocks, Laws for Work-Hardening and Low-Temperature Creep, Journal of Engineering Materials and Technology 98 (1) (1976) 76. `doi:10.1115/1.3443340`.

[89] P. Sherstnev, P. Lang, E. Kozeschnik, Treatment of Simultaneous Deformation and Solid- State Precipitation in Thermo-Kinetic Calculations, in: J. Eberhardsteiner (Ed.), ECCOMAS 2012 - European Congress on Computational Methods in Applied Sciences and Engineering, e-Book Full Papers, Vienna, 2012, pp. 5331–5338.

[90] R. J. Gleixner, B. M. Clemens, W. D. Nix, Void Nucleation in Passivated Interconnect Lines: Effects of Site Geometries, Interfaces, and Interface Flaws, Journal of Materials Research 12 (08) (1997) 2081–2090. `doi:10.1557/JMR.1997.0279`.

[91] P. M. Anderson, P. G. Shewmon, Stress redistribution and cavity nucleation near a diffusively growing grain boundary cavity, Mechanics of Materials 32 (3) (2000) 175–191. `doi:10.1016/S0167-6636(99)00048-4`.

[92] M. Kassner, T. Hayes, Creep cavitation in metals, International Journal of Plasticity 19 (10) (2003) 1715–1748. `doi:10.1016/S0749-6419(02)00111-0`.

[93] C. Zener, Elasticity and Anelasticity of Metals, The University of Chicago Press, 1948.

[94] C. Zener, The micro-mechanism of fracture, in: Fracturing of Metals, American Society for Metals, Cleveland, OH, 1948, pp. 3–31.

[95] A. Stroh, A theory of the fracture of metals, Advances in Physics 6 (24) (1957) 418–465. `doi:10.1080/00018735700101406`.

[96] E. Smith, J. T. Barnby, Crack Nucleation in Crystalline Solids, Metal Science Journal 1 (1) (1967) 56–64. `doi:10.1179/msc.1967.1.1.56`.

[97] J. Weiss, E. M. Schulson, Grain-boundary sliding and crack nucleation in ice, Philosophical Magazine A 80 (2) (2000) 279–300. `doi:10.1080/01418610008212053`.

[98] M. Kikuchi, K. Shiozawa, J. R. Weertman, Void nucleation in astroloy: theory and experiments, Acta Metallurgica 29 (10) (1981) 1747–1758. `doi:10.1016/0001-6160(81)90008-0`.

[99] J. Weertman, Zener-Stroh crack, Zener-Hollomon parameter, and other topics, Journal of Applied Physics 60 (6) (1986) 1877–1887. `doi:10.1063/1.337236`.

[100] A. H. Cottrell, Theory of brittle facture in steel and similar metals, Trans. Metallurgical Soc. AIME 212 (1958) 192–203.

[101] J. N. Greenwood, Intercrystalline Cracking of Metals, Journal of the Iron and Steel Institute 171 (4) (1952) 380.

[102] E. S. Machlin, Creep-Rupture by Vacancy Condensation, JOM 8 (2) (1956) 106–111. `doi:10.1007/BF03377651`.

[103] D. Hull, D. E. Rimmer, The growth of grain-boundary voids under stress, Philosophical Magazine 4 (42) (1959) 673–687. `doi:10.1080/14786435908243264`.

[104] J. Harris, An analysis of creep ductility of magnox Al80 and its implications, Journal of Nuclear Materials 15 (3) (1965) 201–207. `doi:10.1016/0022-3115(65)90181-9`.

[105] J. E. Harris, Nucleation of Creep Cavities in Magnesium, Trans. Met. Soc. AIME 233. Available from: `https://www.osti.gov/biblio/4577560`.

[106] I. W. Chen, Mechanisms of cavity growth in creep, Scripta Metallurgica 17 (1) (1983) 17–22. `doi:10.1016/0036-9748(83)90063-7`.

[107] T. G. Langdon, Grain boundary sliding revisited: Developments in sliding over four decades, Journal of Materials Science 41 (3) (2006) 597–609. `doi:10.1007/s10853-006-6476-0`.

[108] A. Ball, M. M. Hutchison, Superplasticity in the Aluminium-Zinc Eutectoid, Metal Science Journal 3 (1) (1969) 1–7. `doi:10.1179/msc.1969.3.1.1`.

[109] A. Ball, Superplasticity in the aluminium-zinc eutectoid—an early model revisited, Materials Science and Engineering: A 234-236 (97) (1997) 365–369. `doi:10.1016/S0921-5093(97)00157-3`.

[110] M. E. Kassner, Fundamentals of creep in metals and alloys, 2nd Edition, Elsevier, Amsterdam [u.a.], 2009.

[111] J. Wadsworth, O. A. Ruano, O. D. Sherby, Denuded zones, diffusional creep, and grain boundary sliding, Metallurgical and Materials Transactions A: Physical Metallurgy and Materials Science 33 (2) (2002) 219–229. `doi:10.1007/s11661-002-0084-7`.

[112] E. Clouet, Modeling of Nucleation Processes (dec 2009). `doi:10.31399/asm.hb.v22a.a0005410`.

[113] Max-Planck-Institut für Kolloid- und Grenzflächenforschung, Particle Formation : Theory of Nucleation and Systems, hR, 2021-03-13: This entry needs a note, otherwise bibtex issues a warning. Available from: `http://www.mpikg.mpg.de/886735/Nucleationlecture.pdf` [accessed 2019-08-19].

[114] D. Kashchiev, Nucleation, Elsevier, 2000. `doi:10.1016/B978-0-7506-4682-6.X5000-8`.

[115] J. W. Christian, The Classical Theory of Nucleation, in: J. W. Christian (Ed.), The Theory of Transformations in Metals and Alloys, 3rd Edition, Pergamon, Oxford, 2002, Ch. 10, pp. 422–479. `doi:10.1016/B978-008044019-4/50014-3`.

[116] R. M. Nyquist, V. Talanquer, D. W. Oxtoby, Density functional theory of nucleation: A semiempirical approach, The Journal of Chemical Physics 103 (3) (1995) 1175–1179. `doi:10.1063/1.469827`.

[117] P. J. Clemm, J. C. Fisher, The influence of grain boundaries on the nucleation of secondary phases, Acta Metallurgica 3 (1) (1955) 70–73. `doi:10.1016/0001-6160(55)90014-6`.

[118] M. Ohring, Failure and Reliability of Electronic Materials and Devices, in: Engineering Materials Science, Elsevier, 1995, pp. 747–788. `doi:10.1016/B978-012524995-9/50039-8`.

[119] J. Hormadaly, M. Prudenziati, 3 - materials science concepts for printed films, in: J. Hormadaly, M. Prudenziati (Eds.), Printed Films, Woodhead Publishing Series in Electronic and Optical Materials, Woodhead Publishing, 2012, pp. 63–89. `doi:10.1533/9780857096210.1.63`.

[120] R. Radis, E. Kozeschnik, Numerical simulation of NbC precipitation in microalloyed steel, Modelling and Simulation in Materials Science and Engineering 20 (5). `doi:10.1088/0965-0393/20/5/055010`.

[121] S. Allen, T. Eagar, Phase Transformations: Nucleation Theory, mIT OpenCourseWare (2006). Available from: `https://ocw.mit.edu/courses/materials-science-and-engineering/3-205-thermodynamics-and-kinetics-of-materials-fall-2006/lecture-notes/lecture07_slides.pdf`.

[122] J. Svoboda, Numerical study of cavity nucleation kinetics, Acta Metallurgica et Materialia 39 (5) (1991) 963–970. `doi:10.1016/0956-7151(91)90296-D`.

[123] J. Svoboda, Cooperation of diffusive processes at cavity nucleation in high temperature creep, Acta Metallurgica et Materialia 41 (12) (1993) 3495–3503. `doi:10.1016/0956-7151(93)90229-L`.

[124] N. Mott, CXVII. A theory of work-hardening of metal crystals, The London, Edinburgh, and Dublin Philosophical Magazine and Journal of Science 43 (346) (1952) 1151–1178. `doi:10.1080/14786441108521024`.

[125] A. H. Cottrell, Point Defects and the Mechanical Properties of Metals and Alloys at Low Temperatures, in: Vacancies and Other Point Defects in Metals and Alloys, Vol. Monograph, The Institute of Metals, London, 1958, Ch. 1, pp. 1–39.

[126] T. Ungár, E. Schafler, P. Hanák, S. Bernstorff, M. Zehetbauer, Vacancy production during plastic deformation in copper determined by in situ X-ray diffraction, Materials Science and Engineering A 462 (1-2) (2007) 398–401. `doi:10.1016/j.msea.2006.03.156`.

[127] P. Wiehoff, Thermo-mechanische Untersuchung eines Nb-mikrolegierten Stahls im 2. Duktilitätsminimum, TU Wien, Vienna, 2018. Available from: `http://katalog.ub.tuwien.ac.at/AC15192037` [accessed 2019-08-25].

[128] C. M. Chimani, K. Mörwald, Micromechanical Investigation of the Hot Ductility Behavior of Steel., ISIJ International 39 (11) (1999) 1194–1197. `doi:10.2355/isijinternational.39.1194`.

[129] B. Mintz, A. Cowley, R. Abushosha, Importance of columnar grains in dictating hot ductility of steels, Materials Science and Technology 16 (1) (2000) 1–5. `doi:10.1179/026708300773002591`.

[130] M. Vidal, Service Newsletter - April - Abbildung periodischer Randbedingungen in ANSYS (2004). Available from: `http://ww3.cad.de/foren/ubb/uploads/Soren32/ansys_lagerung_Newsletter_04_2004.pdf` [accessed 2019-08-23].

[131] E. Kozeschnik, Mean-Field Microstructure Kinetics Modeling, in: F. G. Caballero (Ed.), Encyclopedia of Materials: Metals and Alloys, Elsevier, Oxford, 2022, pp. 521–526. `doi:10.1016/B978-0-12-819726-4.00055-7`.

[132] ANSYS Inc., Lecture 2 - Installing, compiling and linking UPFs (2011). Available from: `http://www.cadfamily.com/download-pdf/ANSYS_MAPDL/L02-Installing_compiling_and_linking_UPFs.pdf` [accessed 2019-04-16].

[133] J. R. de Laeter, J. K. Böhlke, P. De Bièvre, H. Hidaka, H. S. Peiser, K. J. R. Rosman, P. D. P. Taylor, Atomic weights of the elements. Review 2000 (IUPAC Technical Report), Pure and Applied Chemistry 75 (6) (2003) 683–800. `doi:10.1351/pac200375060683`.

[134] CIAAW, Atomic weights of the elements 2017. Available from: `http://www.ciaaw.org` [accessed 2019-06-12].

[135] I. Seki, K. Nagata, Lattice Constant of Iron and Austenite Including Its Supersaturation Phase of Carbon, ISIJ International 45 (12) (2005) 1789–1794. `doi:10.2355/isijinternational.45.1789`.

[136] M. P. Surh, J. B. Sturgeon, W. G. Wolfer, Void nucleation, growth, and coalescence in irradiated metals, Journal of Nuclear Materials 378 (1) (2008) 86–97. `doi:10.1016/j.jnucmat.2008.05.009`.

[137] S. M. Kim, W. J. L. Buyers, Vacancy formation energy in iron by positron annihilation, Journal of Physics F: Metal Physics 8 (5) (1978) L103–L108. `doi:10.1088/0305-4608/8/5/001`.

[138] L. E. Kinsler, A. R. Frey, A. B. Coppens, J. V. Sanders, Fundamentals of Acoustics, 4th Edition, Wiley, 2000.

[139] E. Kozeschnik, MatCalc – The Materials Calculator. Version 6.03 (1997–2020). Available from: `https://www.matcalc.at/index.php/download/developer` [accessed 2020-02-02].

[140] E. Povoden-Karadeniz, MatCalc mobility diffusion database for steel. Version 2.012 (2018). Available from: `https://www.matcalc.at/index.php/databases/open-databases` [accessed 2020-02-02].

[141] E. Povoden-Karadeniz, MatCalc thermodynamic steel database. Version 2.060 (2016). Available from: `https://www.matcalc.at/index.php/databases/open-databases` [accessed 2020-02-02].

[142] G. Stechauner, E. Kozeschnik, Self-diffusion in grain boundaries and dislocation pipes in Al, Fe, and Ni and application to AlN precipitation in steel, Journal of Materials Engineering and Performance 23 (5) (2014) 1576–1579. `doi:10.1007/s11665-014-0921-z`.

[143] J. Gubicza, Defect Structure and Properties of Nanomaterials: Second and Extended Edition, Woodhead Publishing, Duxford, UK, 2017. Available from: `https://www.sciencedirect.com/book/9780081019177/defect-structure-and-properties-of-nanomaterials`.

[144] J. Gubicza, Lattice Defects and Their Influence on the Mechanical Properties of Bulk Materials Processed by Severe Plastic Deformation, MATERIALS TRANSACTIONS 60 (7) (2019) 1230–1242. `doi:10.2320/matertrans.MF201909`.

[145] J. C. Butcher, Numerical Methods for Ordinary Differential Equations, 2nd Edition, John Wiley & Sons, Ltd, Chichester, UK, 2008. `doi:10.1002/9780470753767`.

[146] A. Iserles, A First Course in the Numerical Analysis of Differential Equations, Cambridge University Press, Cambridge, 2008. `doi:10.1017/CBO9780511995569`.

[147] Wikipedia contributors, Runge-Kutta methods (2018). Available from: `https://en.wikipedia.org/w/index.php?title=Runge-Kutta_methods&oldid=866837125` [accessed 2018-11-07].

[148] J. Gurland, Observations on the fracture of cementite particles in a spheroidized 1.05 % C steel deformed at room temperature, Acta Metallurgica 20 (5) (1972) 735–741. `doi:10.1016/0001-6160(72)90102-2`.

[149] S. H. Goods, L. M. Brown, Overview No. 1. The nucleation of cavities by plastic deformation, Acta Metallurgica 27 (1) (1979) 1–15. `doi:10.1016/0001-6160(79)90051-8`.

[150] A. S. Argon, J. Im, R. Safoglu, Cavity formation from inclusions in ductile fracture, Metallurgical Transactions A 6 (4) (1975) 825–837. `doi:10.1007/BF02672306`.

[151] A. Needleman, J. R. Rice, Limits to Ductility Set by Plastic Flow Localization, in: Mechanics of Sheet Metal Forming, Springer US, Boston, MA, USA, 1978, pp. 237–267. `doi:10.1007/978-1-4613-2880-3_10`.

[152] C. C. Chu, A. Needleman, Void nucleation effects in biaxially stretched sheets, Journal of Engineering Materials and Technology, Transactions of the ASME 102 (3) (1980) 249–256. `doi:10.1115/1.3224807`.

[153] V. Tvergaard, Ductile fracture by cavity nucleation between larger voids, Journal of the Mechanics and Physics of Solids 30 (4) (1982) 265–286. `doi:10.1016/0022-5096(82)90033-3`.

[154] E. Kozeschnik, J. Svoboda, F. Fischer, Modified evolution equations for the precipitation kinetics of complex phases in multi-component systems, Calphad 28 (4) (2004) 379–382. `doi:10.1016/j.calphad.2004.11.003`.

[155] J. Svoboda, F. D. Fischer, P. Fratzl, E. Kozeschnik, Modelling of kinetics in multi-component multi-phase systems with spherical precipitates - I: Theory, Materials Science and Engineering A 385 (1-2) (2004) 166–174. `doi:10.1016/j.msea.2004.06.018`.

[156] E. Kozeschnik, J. Svoboda, P. Fratzl, F. D. Fischer, Modelling of kinetics in multi-component multi-phase systems with spherical precipitates - II: Numerical solution and application, MATERIALS SCIENCE AND ENGINEERING A-STRUCTURAL MATERIALS PROPERTIES MICROSTRUCTURE AND PROCESSING 385 (1-2) (2004) 157–165. `doi:10.1016/j.msea.2004.06.016`.

[157] B. Mintz, Importance of Ar 3 temperature in controlling ductility and width of hot ductility trough in steels, and its relationship to transverse cracking, Materials Science and Technology 12 (2) (1996) 132–138. `doi:10.1179/mst.1996.12.2.132`.

[158] S. Jansto, The Integration of Process and Product Metallurgy in Niobium Bearing Steels, Metals 8 (9) (2018) 671. `doi:10.3390/met8090671`.

[159] R. Krobath, C. Bernhard, S. Ilie, J. Six, S. Hahn, A new method for the experimental simulation of surface crack formation in continuous casting, Metallurgia Italiana 109 (4) (2017) 5–13. Available from: `http://www.aimnet.it/la_metallurgia_italiana/2017/aprile/Krobath.pdf` [accessed 2019-08-19].

[160] Y. Maehara, K. Yasumoto, H. Tomono, Y. Ohmori, Morphology of Carbonitrides and Hot Ductility of Low Carbon Low Alloy Steels, Trans.Iron Steel Inst.Jpn 27 (3) (1987) 222–228. `doi:10.2355/isijinternational1966.27.222`.

[161] P. Sricharoenchai, C. Nagasaki, J. Kihara, Hot Ductility of High Purity Steels Containing Niobium., ISIJ International 32 (10) (1992) 1102–1109. `doi:10.2355/isijinternational.32.1102`.

[162] K. Suzuki, S. Miyagawa, Y. Saito, K. Shiotani, Effect of Microalloyed Nitride Forming Elements on Precipitation of Carbonitride and High Temperature Ductility of Continuously Cast Low Carbon Nb Containing Steel Slab., ISIJ International 35 (1) (1995) 34–41. `doi:10.2355/isijinternational.35.34`.

[163] K. Banks, A. Koursaris, F. Verdoorn, A. Tuling, Precipitation and hot ductility of low C-V and low C-V-Nb microalloyed steels during thin slab casting, Materials Science and Technology 17 (12) (2001) 1596–1604. `doi:10.1179/026708301101509665`.

TU Bibliothek WIEN Your knowledge hub
Die approbierte gedruckte Originalversion dieser Dissertation ist an der TU Wien Bibliothek verfügbar.
The approved original version of this doctoral thesis is available in print at TU Wien Bibliothek.

[164] D. N. Crowther, The Effects of Microalloying Elements on Cracking During Continuous Casting, Vanitec Symposium Proceedings - The Use of Vanadium in Steel (2001) 99–131.

[165] J. R. Davis, High-Strength Low-Alloy Steels, in: J. R. Davis, Davis & Associates (Eds.), Alloying: Understanding the Basics, ASM International, Materials Park, Ohio, 2001, pp. 193–209. `doi:10.31399/asm.tb.aub.t61170193`.

[166] C. Hippsley, J. Knott, B. Edwards, A study of stress relief cracking in Cr 1 Mo steel—II. The effects of multi-component segregation, Acta Metallurgica 30 (3) (1982) 641–654. `doi:10.1016/0001-6160(82)90113-4`.

[167] R. Vaghefi, A. Nayebi, M. R. Hematiyan, Investigating the effects of cooling rate and casting speed on continuous casting process using a 3D thermo-mechanical meshless approach, Acta Mechanica 229 (11) (2018) 4375–4392. `doi:10.1007/s00707-018-2240-1`.

[168] J. Sengupta, B. G. Thomas, M. A. Wells, The use of water cooling during the continuous casting of steel and aluminum alloys, Metallurgical and Materials Transactions A 36 (1) (2005) 187–204. `doi:10.1007/s11661-005-0151-y`.

[169] E. Kozeschnik, General considerations (2011). Available from: `https://www.matcalc.at/wiki/doku.php?id=howtosimulate:precipitation:general#the_representative_volume_element_rve` [accessed 2019-08-23].

[170] ANSYS Inc., Mechanical APDL (2016).

[171] M. Ashby, Boundary defects, and atomistic aspects of boundary sliding and diffusional creep, Surface Science 31 (1972) 498–542. `doi:10.1016/0039-6028(72)90273-7`.

[172] L. Murr, G. Wong, R. Horylev, Measurement of interfacial free energies and associated temperature coefficients in 304 stainless steel, Acta Metallurgica 21 (5) (1973) 595–604. `doi:10.1016/0001-6160(73)90068-0`.

[173] D. M. Mattox, Substrate (“Real”) Surfaces and Surface Modification, in: Handbook of Physical Vapor Deposition (PVD) Processing, Elsevier, 2010, pp. 25–72. `doi:10.1016/B978-0-8155-2037-5.00002-2`.

[174] V. V. Bulatov, B. W. Reed, M. Kumar, Grain boundary energy function for fcc metals, Acta Materialia 65 (2014) 161–175. `doi:10.1016/j.actamat.2013.10.057`.

APPENDIX A

Strain Rate in the Extreme Fiber

The following calculations are based on fig. 3.12. As mentioned above, the calculations are only valid for a perfectly shaped caster with no local misalignments. For each segment of the bent strand, the inner radius r is calculated from the difference between the outer radius R and the strand height h ($r = R - h$). The segment area is the integral of the radius over the height and the angle (eq. (A.1)).

$$A = \int_0^{\varphi} \int_r^R r \, \mathrm{d}r \, \mathrm{d}\varphi = \varphi \left(R^2 - r^2\right)/2 \tag{A.1}$$

After unbending, we have a straight strand. The previously different arc lengths (l and L) now have the same length ($l' = L'$). The area is calculated using the formula for rectangles (eq. (A.2)).

$$A' = L'h = l'h \tag{A.2}$$

Equating eqs. (A.1) and (A.2) based on the conservation of area assumption ($A = A'$)* gives eq. (A.3).

$$\frac{(R^2 - r^2)}{2}\varphi = L'h = l'h \quad | \, \varphi = \frac{\overset{\frown}{L}}{R} = \frac{\overset{\frown}{l}}{r} \tag{A.3}$$

From this point on, we distinguish between outer and inner radius and show in eqs. (A.4) to (A.7) how to calculate the true strain using only the given parameters.

---

*Conservation of area—not volume—as we assume constant width during straightening.

Outer Radius **Inner Radius**

$$L'h = \frac{\left(R^2 - r^2\right)}{2}\frac{\overset{\frown}{L}}{R} \qquad l'h = \frac{\left(R^2 - r^2\right)}{2}\frac{\overset{\frown}{l}}{r} \tag{A.4}$$

$$\frac{L'}{\overset{\frown}{L}} = \frac{R^2 - r^2}{2Rh} \qquad \frac{l'}{\overset{\frown}{l}} = \frac{R^2 - r^2}{2rh} \qquad \mid \ln \tag{A.5}$$

$$\varepsilon_{\mathrm{o}} = \ln\left(\frac{L'}{\overset{\frown}{L}}\right) = \ln\left(\frac{R^2 - r^2}{2Rh}\right) \qquad \varepsilon_{\mathrm{i}} = \ln\left(\frac{l'}{\overset{\frown}{l}}\right) = \ln\left(\frac{R^2 - r^2}{2rh}\right) \qquad \mid r = R - h \tag{A.6}$$

$$\varepsilon_{\mathrm{o}} = \ln\left(1 - \frac{h}{2R}\right) \qquad \varepsilon_{\mathrm{i}} = \ln\left(\frac{2R - h}{2\left(R - h\right)}\right) \tag{A.7}$$

Finally, the average strain rate in the two extreme fibers can be calculated by dividing the respective true strain by the straightening time. Where $\bar{l}$ is the arc length, $\bar{v}$ is the casting velocity, and $\bar{t}$ is the straightening time in the center fiber. The combination of strain (eq. (A.8)) and straightening time (eq. (A.9)) gives the average strain rate in the straightening zone (eq. (A.9)).

$$\bar{t} = \frac{\bar{l}}{\bar{v}} \tag{A.8}$$

$$\dot{\varepsilon}_n = \frac{\varepsilon_n}{\bar{t}} = \frac{\bar{v}}{\bar{l}}\varepsilon_n \qquad \mid n = \mathrm{o}, \mathrm{i} \tag{A.9}$$

APPENDIX B

Additional results

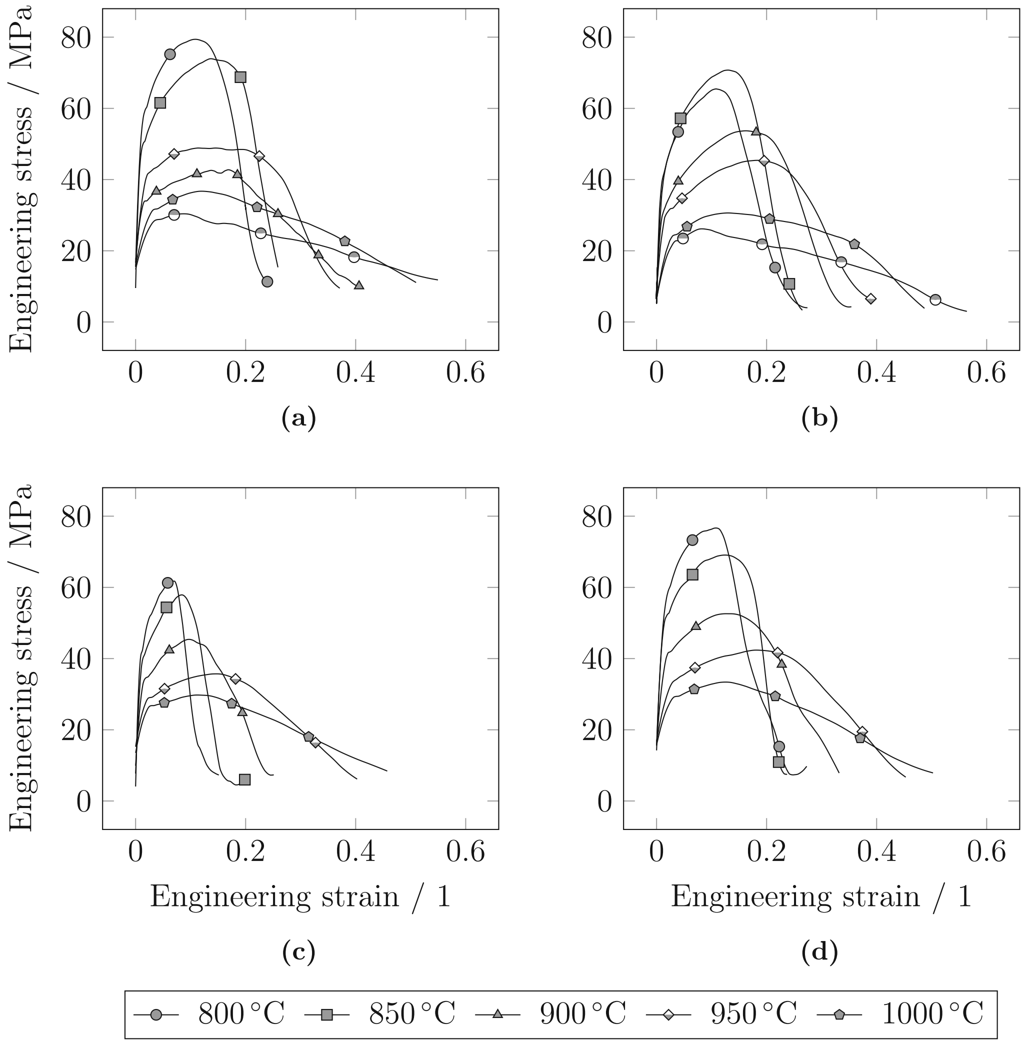

(a) (b) (c) (d)

Figure B.1. Engineering stress-strain curves of tested samples. (a) $d_0 = \varnothing 8\,\mathrm{mm}$, 800 s, $3 \times 10^{-4}\,\mathrm{s}^{-1}$, (b) $d_0 = \varnothing 16\,\mathrm{mm}$, 800 s, $3 \times 10^{-4}\,\mathrm{s}^{-1}$, (c) $d_0 = \varnothing 8\,\mathrm{mm}$, $1\,\mathrm{K\,s}^{-1}$, $1 \times 10^{-4}\,\mathrm{s}^{-1}$, (d) $d_0 = \varnothing 8\,\mathrm{mm}$, $1\,\mathrm{K\,s}^{-1}$, $3 \times 10^{-4}\,\mathrm{s}^{-1}$

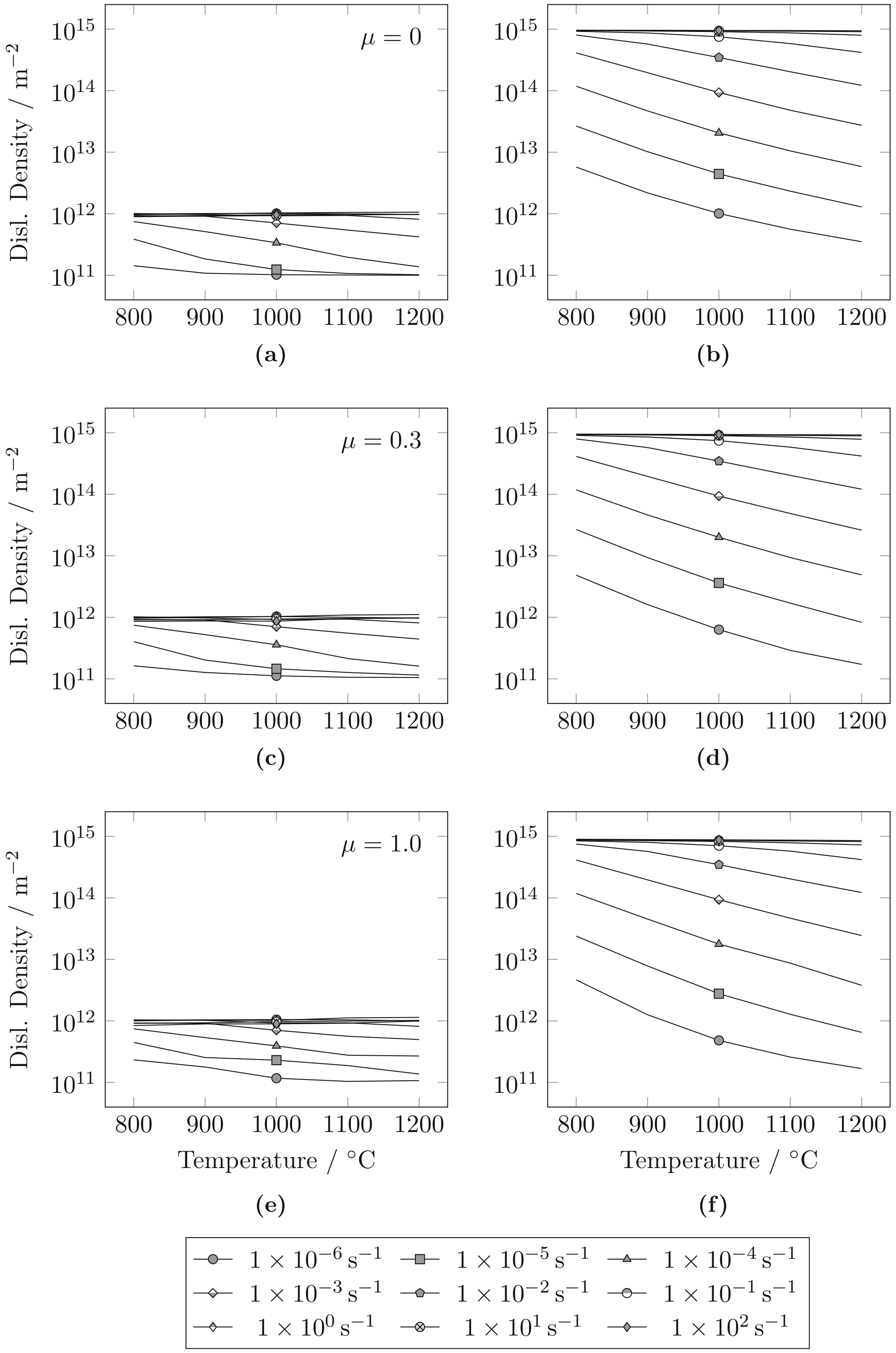

(a) **(b)**

(c) **(d)**

(e) **(f)**

Figure B.2. Temperature dependence of (a), (c), and (e) the minimum and (b), (d), and (f) the maximum dislocation density for different strain rates evaluated at 5 % external strain in the vertical direction and friction coefficient $\mu = 0$.

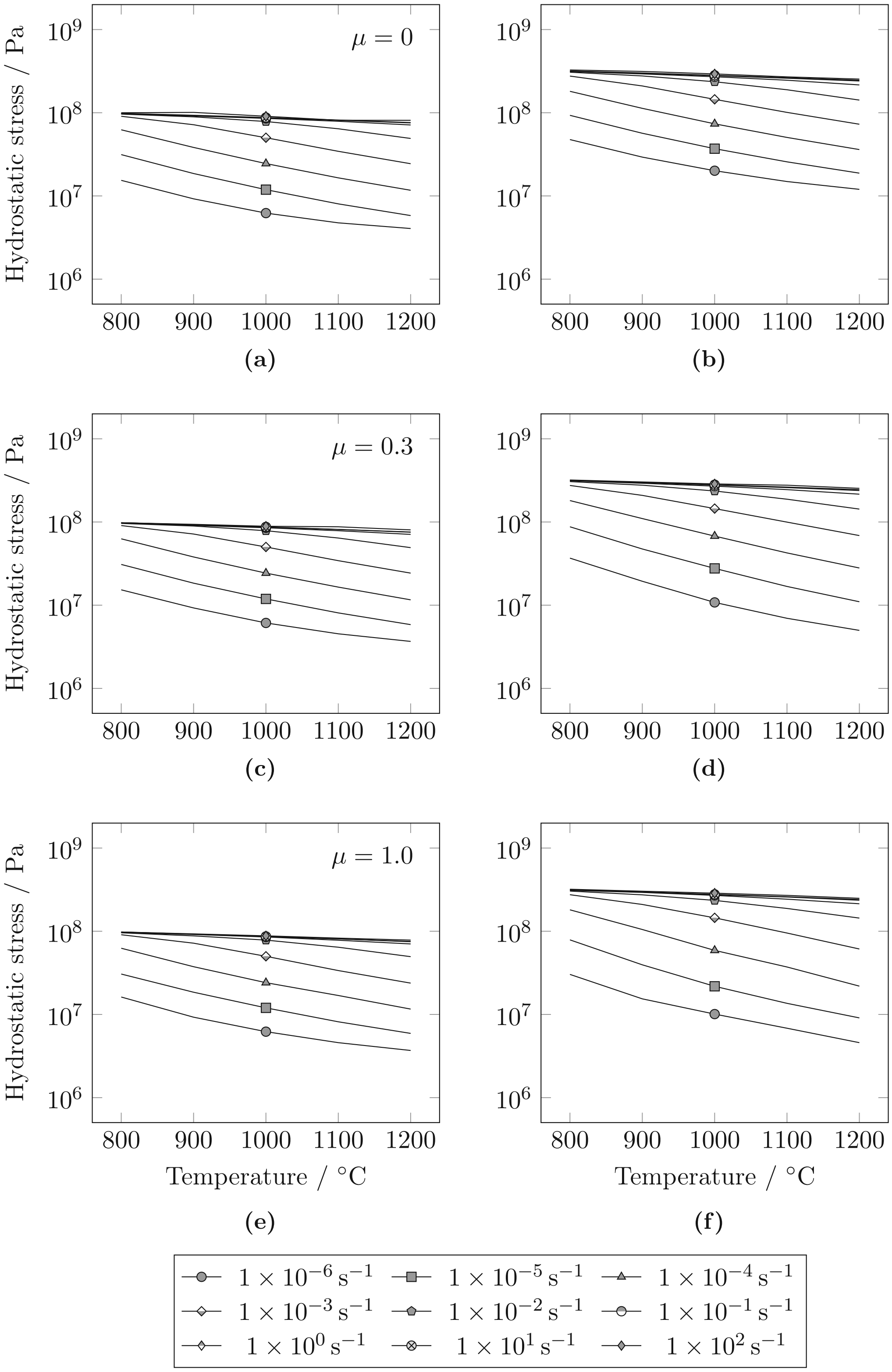

Figure B.3. Temperature dependence of (a), (c), and (e) the hydrostatic stress at the grain center and (b), (d), and (f) the maximum recorded value for different strain rates evaluated at 5 % external strain in the vertical direction and friction coefficient $\mu = 0$.

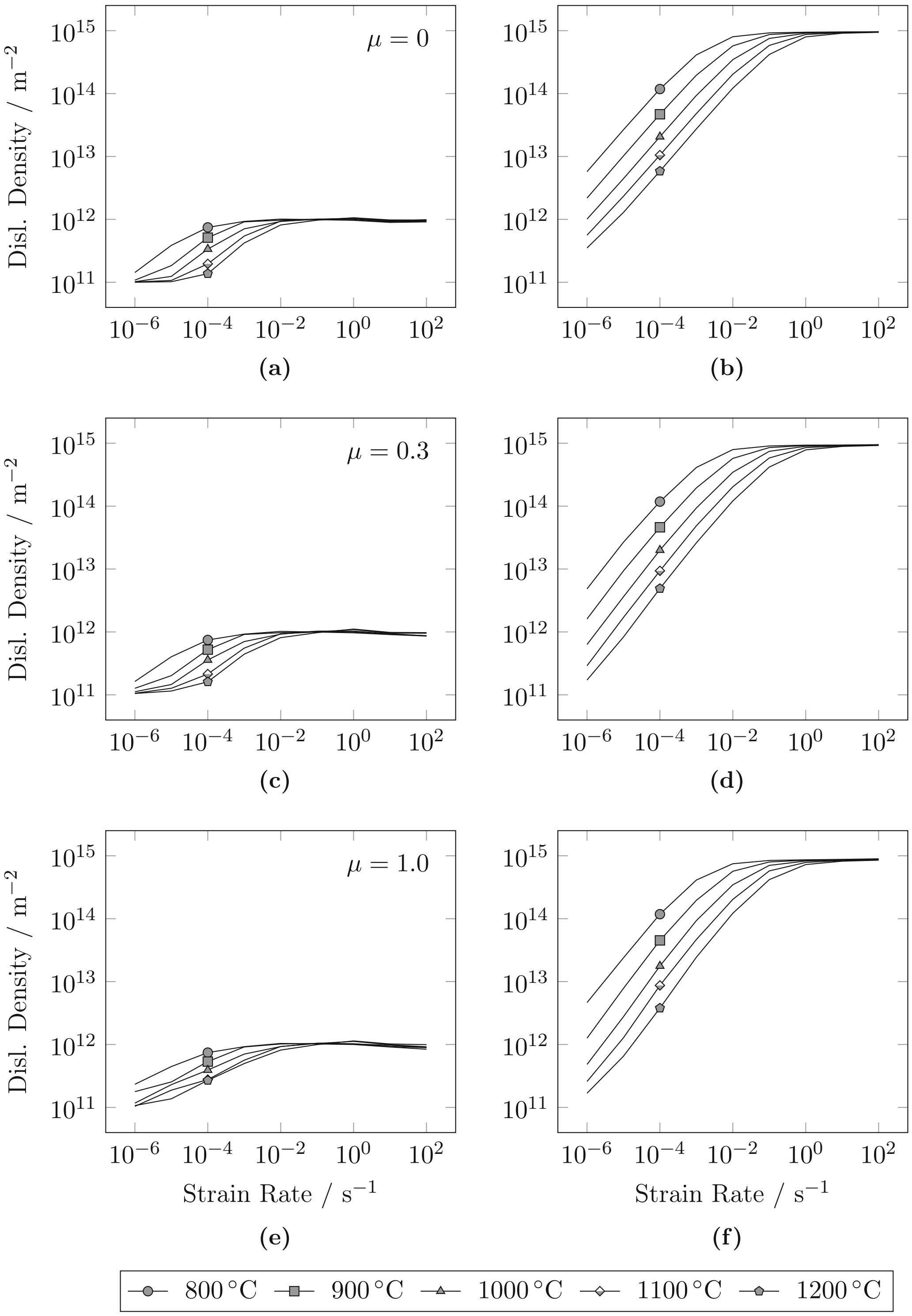

(a) (b)

(c) (d)

(e) (f)

Figure B.4. Strain rate dependence of (a), (c), and (e) the minimum and (b), (d), and (f) the maximum dislocation density for different temperatures evaluated at 5 % external strain in the vertical direction and friction coefficient $\mu = 0$.

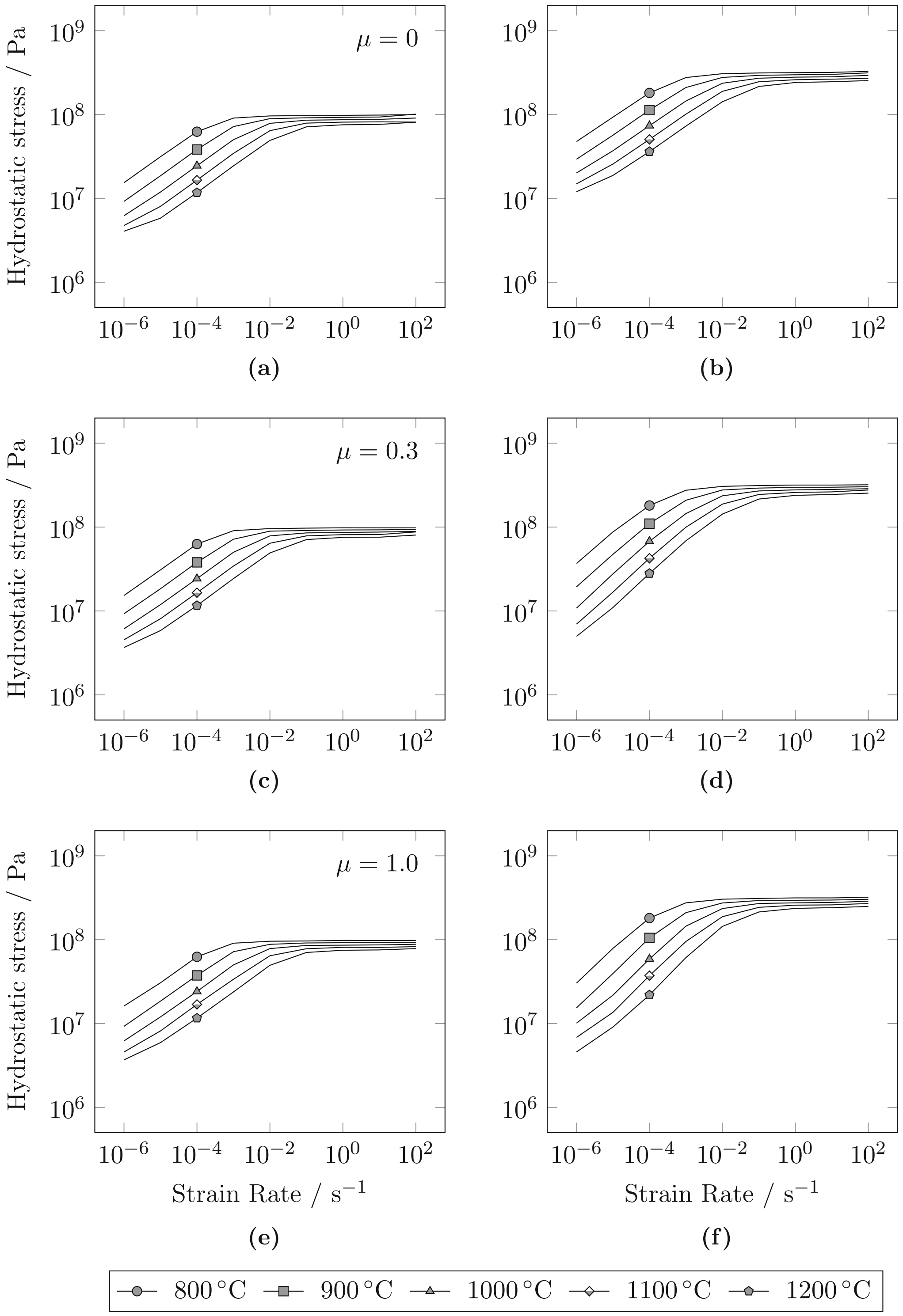

Figure B.5. Strain rate dependence of (a), (c), and (e) the hydrostatic stress at the grain center and (b), (d), and (f) the maximum recorded value for different temperatures evaluated at 5 % external strain in the vertical direction and friction coefficient $\mu = 0$.

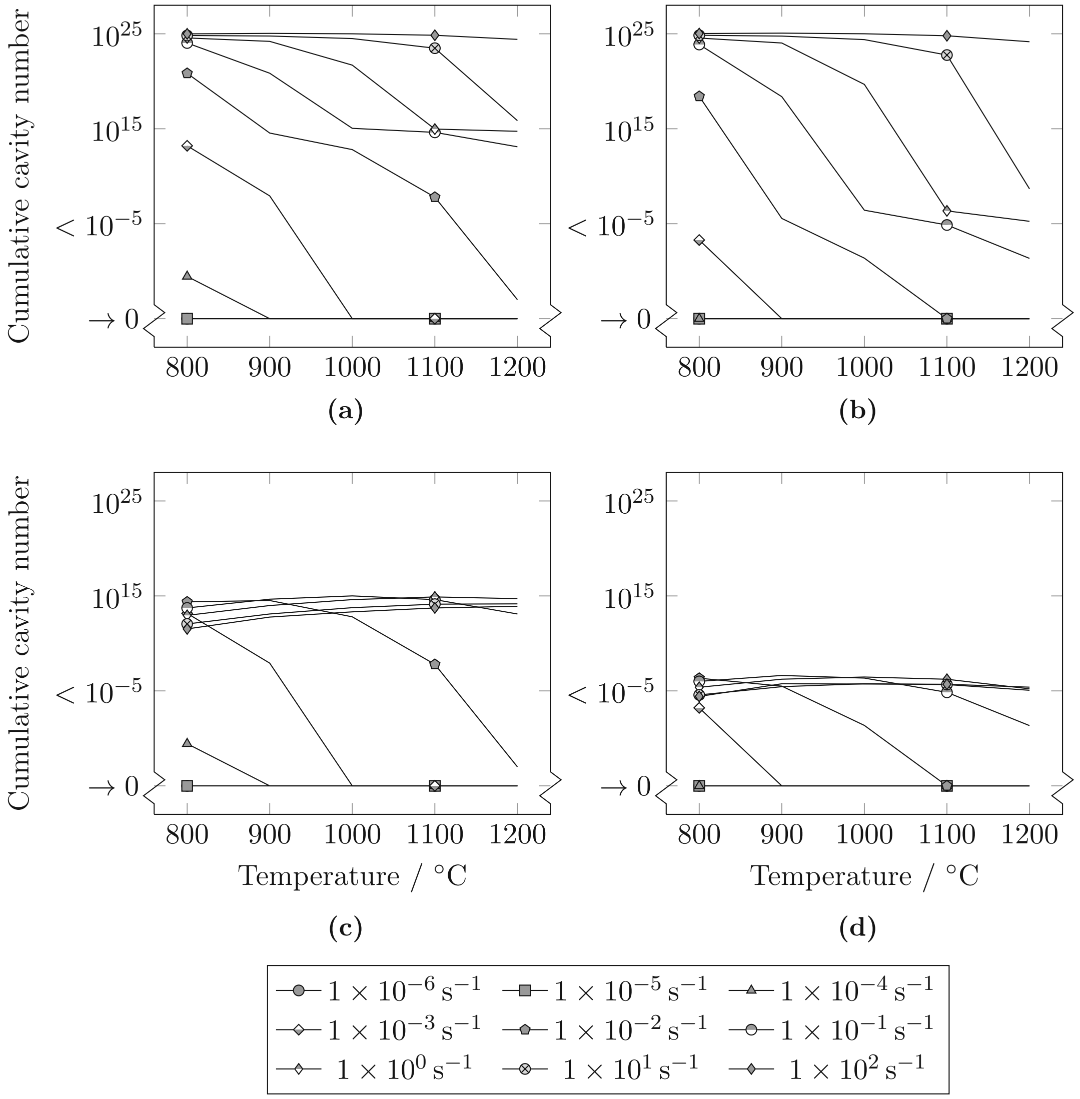

Figure B.6. Temperature dependence of the cumulative nucleated cavity number according to the model setup based on (a) and (b) Tang-Plumtree [16] and (c) and (d) Ungár et al. [126] for different strain rates evaluated at 5 % external strain in the vertical direction and friction coefficient $\mu = 0$.

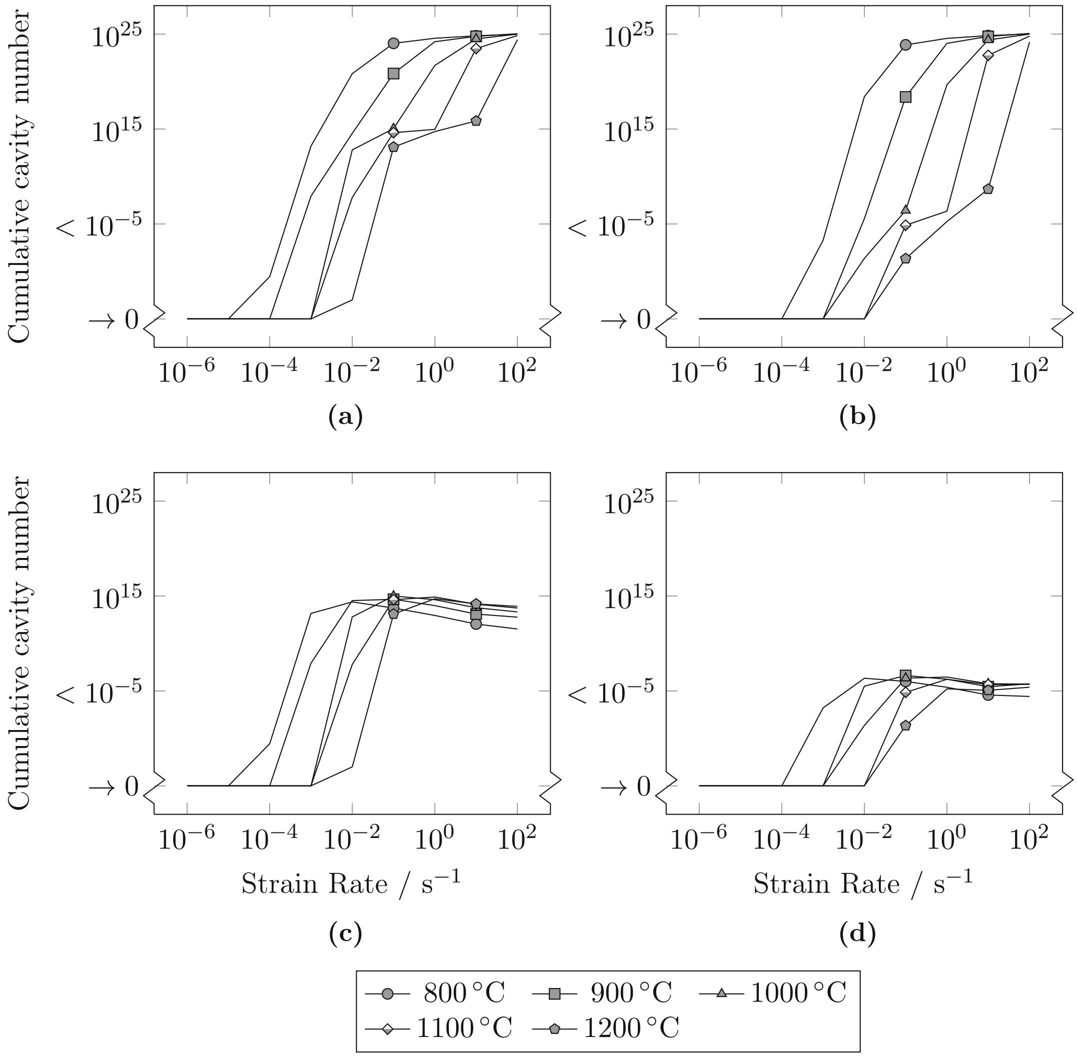

Figure B.7. Strain rate dependence of the cumulative nucleated cavity number according to the model setup based on (a) and (b) Tang-Plumtree [16] and (c) and (d) Ungár et al. [126] for different temperatures evaluated at 5 % external strain in the vertical direction and friction coefficient $\mu = 0$.

Curriculum vitae

Harald Radlwimmer was born in Mödling, Austria, in 1984. He went to Gymnasium Bachgasse Mödling and later attended the technical college HTBLuVA Mödling, department of Mechatronics. In the final year at HTBLuVA Mödling, he and two classmates developed a test bench for dental motors in cooperation with a renowned Austrian dental equipment manufacturer. The utility model AT6118U2 entitled "Bremsvorrichtung für Kleinmotoren zur Erfassung der Antriebsmomente" was derived from the thesis. He graduated in 2003 with the final examination, *Matura*, which he passed with distinction. Afterward, he joined the Austrian Armed Forces for a year as a military musician and augmented his skills on the clarinet. In 2004, he started studying mechanical engineering at TU Wien and became interested in engineering design, lightweight design, and material-related subjects.

Besides the university courses, Harald Radlwimmer worked part-time in an engineering company for several years and trained pupils in snowboarding at school sports weeks. In 2010, he studied for one year abroad in the Erasmus program at the University of Stavanger, Norway, where he learned about fatigue, corrosion, and offshore field development. But he also learned about other cultures, made friends, and fell in love. Additionally, he joined the local brass band SMK1919 in his Erasmus year and competed with them in the annual national championship.

After returning home, Harald Radlwimmer became fascinated by materials science and the capabilities of computer simulations. He graduated in 2014 from TU Wien with a Master of Science degree and received the Peter Emil Varga Foundation Award 2015 for his Master's thesis titled "Microstructural evolution during homogenization of AA-7075 alloy". Later that year, he started as a doctoral candidate with Ernst Kozeschnik at the Institute of Materials Science and Technology, TU Wien. Besides his research, Harald Radlwimmer was a teaching assistant for scanning electron microscopy in the annual laboratory course. He presented his research at two international conferences: THERMEC'2016, Graz, Austria, and FEMS EUROMAT 2017, Thessaloniki, Greece.

In 2020, Harald Radlwimmer joined the leading Austrian manufacturer of pedestrian and occupant safety systems and battery separators as a simulation engineer.

Harald Radlwimmer and his partner Anke have a lovely daughter named Frida.